Acta Technica *63* No. 3/2018, 353–368

Vibration analysis of nonhomogeneous tapered rectangular plate under thermal effect

Narinder Kaur[1 3], Anupam Khanna[2]

Abstract. Effect of non-homogeneity on the vibration of visco-elastic tapered rectangular plate has been investigated on the basis of classical plate theory. The non-homogeneous mechanical properties of the plate are assumed to be exponential along with linear thickness variation in x-direction. It is assumed that temperature varies bi-directionally such that linearly in x-direction but parabolically in y-direction. The governing differential equation for such a plate model has been obtained by using Hamilton's principle. The differential transform method has been employed to obtain the frequency equation for clamped boundary condition. Effects of different plate's parameters viz. non-homogeneity constant, taper constant, thermal gradient and aspect ratio on first two modes of vibration have been studied and tabulated in Tables 1–8. Comparison with existing results has been made.

Key words. Vibration, linear thickness, visco-elastic, non-homogeneity, frequency, plate's parameters.

1. Introduction

There has been amazing discoveries in the field of thermally induced vibration drawing the attention of scientists and design engineers to study the tremendous effect of non-uniform thickness variation on vibrational behavior of plates of different shapes and sizes in engineering and modern technology. Study of vibration is not just confined to science but also our day to day life. From its constructive aspects in aircrafts engineering, space technology etc., to the destructive aspects e. g. earthquake, satellite; nothing is untouched by effects of vibration.

The prevalent interest in the effects of high temperature on vibration of non-homogeneous rectangular plates of variable thickness is due to their applications in

[1]Department of Mathematics, Statistics and Physics, Punjab Agricultural University, Ludhiana, Punjab, India; e-mail: narinder89.kaur@gmail.com

[2]Department of Mathematics, D. A. V. College, Sadhaura, Yamunanagar, Haryana, India; e-mail: rajieanupam@gmail.com

[3]Corresponding author.

various engineering branches such as nuclear power plants, aeronautical engineering, chemical plants and so forth, where metals and their alloys exhibit visco-elastic behavior. The reason for this is that during heating-up periods, structures are exposed to high-intensity heat fluxes and material properties undergo significant changes; in particular; thermal effect can not be negligible. A lot of research work has been done in the area of vibration of plate with varying thickness and under thermal condition since last half century. An update literature survey is as follows:

Leissa [1] and Leissa [2] discussed vibration of plates with different boundary conditions. Jain and Soni [3] analyzed effect of parabolic varying thickness on vibration of rectangular plate. Dhotarad and Ganesan [4] worked on vibration of rectangular plate under varying temperature field. Laura et al. [5] discussed effect of two dimensional thickness variation on vibration of rectangular plates. Khanna and Kaur [6–8] discussed vibrational behavior of non homogeneous tapered rectangular plate with bidirectional thermal effect. Singh and Saxena [9] discussed vibration of plate of bi-directional thickness variation. Vibrations of plate with elastic support were discussed by Li [10]. Lal et al. [13] analyzed vibration of non-homogeneous plate with boundary characteristic orthogonal polynomial. Gupta et al. [12] investigated effect of taper constant along with thermal gradient on vibration of plate. Gupta et al. [14] discussed vibrations of non-homogeneous rectangular plate of variable thickness in both directions with thermal gradient.

Here, a theoretical prediction on vibration of non-homogeneous visco-elastic plate is presented for the use of mechanical engineers or design engineers who are always been interested to know about the first few modes of vibration before finalizing the structures of machines/designs. It is considered that temperature varies bi-directional *i.e.* linearly in x-direction and parabolically in y-direction while thickness of plate is assumed to vary linearly in x-direction. The non-homogeneity of the plate's material is characterized by an exponential variation of Poisson's ratio of the plate's material. First two modes of frequency, deflection and logarithmic decrement are reported in tabular form for various combinations of plate's parameters. A comparison with existing results in available literature is also provided in the tabular form.

2. Assumptions required

Since the scope of the study of vibration of plates is too vast to be considered as a whole, authors put few limitations to make easy and convenient calculation for analyzing the vibrational behavior of plates in the influence of varying plate's parameters.

2.1. Linear thickness variation of the plate

Since plates of variable thickness are vigorously used in various mechanical structures and designs, it becomes the need of the hour to examine that how varying thickness affects the vibration of structure or design. Hence, linear thickness variation in

x-direction is taken as [6]

$$g = g_0 \left(1 + \beta \frac{x}{a}\right) . \tag{1}$$

Here, g denotes the thickness of the plate, g_0 is its thickness at $x = 0$, β stands for the taper constant in the x-direction and a represents the length of the plate.

2.2. Temperature variation in the plate

Since most of machines or mechanical structures work under the influence of high temperature variations, it becomes necessary to investigate the effect of variation in temperature on vibrational behavior of the structure or system. Here, bi-directional temperature variations, i. e. linearly in x-direction and parabolically in y-direction are considered as follows:

$$\tau = \tau_0 \left(1 - \frac{x}{a}\right) \left(1 - \frac{y^2}{b^2}\right) ,$$

where τ is the temperature excess above the reference temperature at any point on the plate, τ_0 denotes the temperature excess above the reference temperature at $x = y = 0$ and b is the width of the rectangular plate.

The temperature dependence of the modulus of elasticity E for most of the engineering materials can be expressed as [5]:

$$E = E_0(1 - \gamma\tau) ,$$

where E_0 is the modulus of elasticity at the reference temperature and γ denotes the slope of modulus of elasticity with the temperature.

Using the value of τ in E, it becomes

$$E = E_0 \left\{1 - \alpha \left(1 - \frac{x}{a}\right) \left(1 - \frac{y^2}{b^2}\right)\right\} , \tag{2}$$

where α is the thermal gradient.

2.3. Non-homogeneity in the plate's material

Non-homogeneous plates have wide applications in engineering designs and structures and also, non-homogeneity directly affects the physical properties of the material. Since the material is assumed non-homogeneous, authors characterized non-homogeneity in Poisson's ratio of material as exponential variation in x-direction according to [7]

$$\nu = \nu_0 \mathrm{e}^{\alpha_1 x/a} , \tag{3}$$

where ν is the Poisson ratio, ν_0 its value at $x = 0$ and α_1 represents the non-homogeneity constant.

Since maximum value of Poisson ratio is less than or equal to $1/2$, the numeric value of α_1 may not be greater than 0.16 (approximately). Therefore, the results

are calculated for $0.0 \leq \alpha_1 \leq 0.15$.

2.4. Boundary conditions for the plate

In present study, rectangular plate is assumed to be clamped on the boundary. Hence, boundary conditions are [12]

$$W = W_{,x} = 0 \text{ at } x = 0, a, \quad W = W_{,y} = 0 \text{ at } y = 0, b\,. \tag{4}$$

It is considered that visco-elastic properties of rectangular plate are of the Kelvin type. Material of the plate is considered isotropic and made up of visco-elastic material, Duralium.

3. Formulation of equation of motion

Differential equation of motion of an isotropic visco-elastic rectangular plate is

$$\frac{\partial^3 M}{\partial x^3} + 2\frac{\partial^4 M}{\partial x^2 \partial y^2} + \frac{\partial^3 M}{\partial y^3} = \rho g \frac{\partial^2 w}{\partial t^2}\,, \tag{5}$$

where

$$\begin{aligned} \frac{\partial M}{\partial x} &= -\tilde{D} D_1 \left[\frac{\partial^2 w}{\partial x^2} + \nu \frac{\partial^2 w}{\partial y^2}\right], \\ \frac{\partial M}{\partial y} &= -\tilde{D} D_1 \left[\frac{\partial^2 w}{\partial y^2} + \nu \frac{\partial^2 w}{\partial x^2}\right], \\ \frac{\partial^2 M}{\partial x \partial y} &= -\tilde{D} D_1 (1-\nu) \frac{\partial^2 w}{\partial x \partial y}\,. \end{aligned} \tag{6}$$

Here, M denotes the moments, $w(x, y, t)$ is the amplitude of deflection of the plate and ρ is the density of plate's material.

Using Eq. (6) in Eq. (5) one gets [7]

$$\tilde{D}[\nabla^2 (D_1 \nabla^2 w) - (1-\nu) \diamondsuit^4 (D_1, w)] + \rho g \frac{\partial^2 w}{\partial t^2} = 0\,, \tag{7}$$

where

$$\diamondsuit^4 (D_1, w) = \frac{\partial^2 D_1}{\partial y^2}\frac{\partial^2 w}{\partial x^2} - 2\frac{\partial^2 D_1}{\partial x \partial y}\frac{\partial^2 w}{\partial x \partial y} + \frac{\partial^2 D_1}{\partial x^2}\frac{\partial^2 w}{\partial y^2}$$

is the die operator and

$$\nabla^2 \equiv \frac{\partial^2}{\partial x^2} + \frac{\partial^2}{\partial y^2}$$

is the Laplacian operator.

With the help of separation of variable technique, solution of eq. (7) can be assumed as [6]

$$w(x, y, t) = \xi(x, y)\psi(t)\,, \tag{8}$$

where $\xi(x,y)$ is the deflection function and $\psi(t)$ is a time function

After using eq. (8) in eq. (7), one gets

$$\left[D_1\left(\frac{\partial^4\xi}{\partial x^4}+2\frac{\partial^4\xi}{\partial x^2\partial y^2}+\frac{\partial^4\xi}{\partial y^4}\right)+2\frac{\partial D_1}{\partial x}\left(\frac{\partial^3\xi}{\partial x^3}+\frac{\partial^3\xi}{\partial x\partial y^2}\right)\right.$$
$$+2\frac{\partial D_1}{\partial y}\left(\frac{\partial^3\xi}{\partial y^3}+\frac{\partial^3\xi}{\partial y\partial x^2}\right)+\frac{\partial^2 D_1}{\partial x^2}\left(\frac{\partial^2\xi}{\partial x^2}+\nu\frac{\partial^2\xi}{\partial y^2}\right)$$
$$\left.+\frac{\partial^2 D_1}{\partial y^2}\left(\frac{\partial^2\xi}{\partial y^2}+\nu\frac{\partial^2\xi}{\partial x^2}\right)+2(1-\nu)\frac{\partial^2 D_1}{\partial x\partial y}\frac{\partial^2\xi}{\partial x\partial y}\right]/\rho g\xi=-\frac{\ddot{\psi}}{\tilde{D}\psi}\,. \tag{9}$$

Here, dot denotes differentiation with respect to t. The preceding equation is satisfied if both of its sides are equal to a constant. Denoting this constant by p^2, one gets differential equation of transverse motion for non-homogenous plate of variable thickness as

$$\left[D_1\left(\frac{\partial^4\xi}{\partial x^4}+2\frac{\partial^4\xi}{\partial x^2\partial y^2}+\frac{\partial^4\xi}{\partial y^4}\right)+2\frac{\partial D_1}{\partial x}\left(\frac{\partial^3\xi}{\partial x^3}+\frac{\partial^3\xi}{\partial x\partial y^2}\right)\right.$$
$$+2\frac{\partial D_1}{\partial y}\left(\frac{\partial^3\xi}{\partial y^3}+\frac{\partial^3\xi}{\partial y\partial x^2}\right)+\frac{\partial^2 D_1}{\partial x^2}\left(\frac{\partial^2\xi}{\partial x^2}+\nu\frac{\partial^2\xi}{\partial y^2}\right)$$
$$\left.+\frac{\partial^2 D_1}{\partial y^2}\left(\frac{\partial^2\xi}{\partial y^2}+\nu\frac{\partial^2\xi}{\partial x^2}\right)+2(1-\nu)\frac{\partial^2 D_1}{\partial x\partial y}\frac{\partial^2\xi}{\partial x\partial y}\right]-\rho p^2 g\xi=0. \tag{10}$$

and

$$\ddot{\psi}+p^2\tilde{D}\psi=0\,. \tag{11}$$

Eqns. (10) and (11) represent the differential equations of motion and time function for non-homogeneous rectangular plate, respectively. Symbol D_1 denotes the flexural rigidity of rectangular plate

$$D_1=\frac{Eg^3}{12(1-\nu^2)}\,. \tag{12}$$

As plate is assumed to be clamped at the boundary, the corresponding deflection function is considered as follows

$$\xi(x,y)=A(x,y)\times B(x,y)\,, \tag{13}$$

where

$$A(x,y)=\left[\left(\frac{x}{a}\right)\left(\frac{y}{b}\right)\left(1-\frac{x}{a}\right)\left(1-\frac{y}{b}\right)\right]^2\,,$$
$$B(x,y)=\left[W_1+W_2\left(\frac{x}{a}\right)\left(\frac{y}{b}\right)\left(1-\frac{x}{a}\right)\left(1-\frac{y}{b}\right)\right]\,.$$

Here, W_1 and W_2 are arbitrary constants.

4. Solution of frequency equation

To obtain a frequency equation for the vibration of the rectangular plate, authors used the Rayleigh–Ritz method. This method is based on the principle of conservation of energy, i.e. the maximum strain energy $P_{\max}$ must be equal to the maximum kinetic energy $K_{\max}$. So, it is necessary for the problem under consideration that

$$\delta(P_{\max} - K_{\max}) = 0\,, \tag{14}$$

where

$$K_{\max} = \frac{1}{2}\rho p^2 \int_0^a \int_0^b g\xi^2 \,\mathrm{d}y\,\mathrm{d}x \tag{15}$$

and

$$\begin{aligned} P_{\max} =& \frac{1}{2}\int_0^a \int_0^b D_1 \left\{ \left(\frac{\partial^2\xi}{\partial x^2}\right)^2 + \left(\frac{\partial^2\xi}{\partial y^2}\right)^2 + \right. \\ & \left. + 2\nu \frac{\partial^2\xi}{\partial x^2}\frac{\partial^2\xi}{\partial y^2} + 2(1-\nu)\left(\frac{\partial^2\xi}{\partial x \partial y}\right)^2 \right\} \mathrm{d}y\,\mathrm{d}x\,. \end{aligned} \tag{16}$$

To simplify and parameterize the present problem, non-dimensionalization is introduced as follows

$$X = \frac{x}{a}, \quad Y = \frac{y}{a}\,. \tag{17}$$

On using Eqns. (1)–(4) and eq. (12) in eqns. (15) and (16), modified maximum kinetic energy ($K^*_{\max}$) and maximum potential energy ($P^*_{\max}$) are obtained as follows:

$$K^*_{max} = \frac{1}{2}\rho p^2 a^2 g_0 \int_0^1 \int_0^{b/a} (1+\beta X)\xi^2 \,\mathrm{d}Y\,\mathrm{d}X \tag{18}$$

and

$$\begin{aligned} P^*_{\max} =& Q \int_0^1 \int_0^{b/a} \left\{ \frac{\left(1-\alpha(1-X)\left(1-\frac{a^2}{b^2}Y^2\right)\right)(1+\beta X)^3}{(1-{\nu_0}^2 e^{2\alpha_1 X})} \right\} \\ & \{(\frac{\partial^2\xi}{\partial X^2})^2 + (\frac{\partial^2\xi}{\partial Y^2})^2 + 2\nu_0 e^{\alpha_1 X}\frac{\partial^2\xi}{\partial X^2}\frac{\partial^2\xi}{\partial Y^2} \\ & + 2(1-\nu_0 e^{\alpha_1 X})(\frac{\partial^2\xi}{\partial X \partial Y})^2\}\,\mathrm{d}Y\,\mathrm{d}X\,, \end{aligned} \tag{19}$$

where

$$Q = \frac{E_0 g_0^3}{24a^2}\,.$$

After using values of $K^*_{\max}$ and $P^*_{\max}$ from (18) and (19) in (14), one obtains

$$\delta(P^*_{\max} - \lambda^2 K^*_{\max}) = 0\,. \tag{20}$$

Here $\lambda^2 = \frac{12\rho p^2 a^4}{E_0 {g_0}^2}$ is the frequency parameter. Equation (20) consists two unknown constants i.e. W_1 and W_2 arising due to the substitution of ξ. These two constants are to be determined as follows:

$$\frac{\delta(P^*_{\max} - \lambda^2 K^*_{\max})}{\delta W_n} = 0, \qquad n = 1, 2\,. \tag{21}$$

On simplifying eq. (21) one gets

$$B_{n_1} W_1 + B_{n_2} W_2 = 0, \qquad n = 1, 2\,, \tag{22}$$

where $B_{n1}, B_{n2} (n = 1, 2)$ involve plate's parameters and frequency parameter.

Choosing $W_1 = 1$, one can easily get W_2 from eq. (22), which is $(-B_{11}/B_{12})$ or $(-B_{21}/B_{22})$.

For non-trivial solution of (22), determinant of the coefficients of equation (22) must vanish. Therefore, the frequency equation comes as

$$\begin{vmatrix} B_{11} & B_{12} \\ B_{21} & B_{22} \end{vmatrix} = 0\,. \tag{23}$$

Since equation (23) is a quadratic equation in λ^2, one can obtain two values of λ^2. From these values of λ^2, two values of λ i.e. λ_1 and λ_2 may be obtained which represent first and second mode of the fundamental frequency, respectively.

On using W_1 and W_2 in eq. (13), one gets

$$\xi(X, Y) = \left[XY\left(\frac{a}{b}\right)(1 - X)\left(1 - \left(\frac{aY}{b}\right)\right)\right]^2 \left[1 + \left(\frac{-B_{11}}{B_{12}}\right) XY\left(\frac{a}{b}\right)(1 - X)\left(1 - \left(\frac{aY}{b}\right)\right)\right]. \tag{24}$$

Time period of the vibration of visco-elastic plate is given as

$$K = \frac{2 \times \pi}{p}\,. \tag{25}$$

5. Solution of differential equation for time function

For Kelvin's model, visco-elastic operator $\tilde{D}$ is defined as [6]

$$\tilde{D} \equiv \left\{1 + \left(\frac{\eta}{G}\right)\left(\frac{\mathrm{d}}{\mathrm{d}t}\right)\right\}. \tag{26}$$

Using eq. (26) in eq. (11), one gets

$$\ddot{\psi} + p^2 \left(\frac{\eta}{G}\right)\dot{\psi} + p^2 \psi = 0\,. \tag{27}$$

Solution of eq. (27) comes out as

$$\psi(t) = \mathrm{e}^{a_1 t}[B_1 \cos b_1 t + B_2 \sin b_1 t]\,, \tag{28}$$

where

$$a_1 = \frac{-p^2\eta}{2G} \tag{29}$$

and

$$b_1 = p\sqrt{1 - \left(\frac{p\eta}{2G}\right)^2}\,, \tag{30}$$

where B_1, B_2 are constants which can be determined easily from initial conditions of the plate.

The initial conditions of the plate are taken as

$$\psi = 1 \text{ and } \dot{\psi} = 0 \text{ at } t = 0\,. \tag{31}$$

On using eq. (31) in eq. (28), one obtains

$$B_1 = 1 \text{ and } B_2 = \frac{\frac{p^2\eta}{G}}{2b_1} = \frac{-a_1}{b_1}\,. \tag{32}$$

Using eq. (32) in eq. (28), one obtains

$$\psi(t) = \mathrm{e}^{a_1 t}\left[\cos b_1 t + \left(-\frac{a_1}{b_1}\right)\sin b_1 t\right]\,. \tag{33}$$

After using eq. (24) and eq. (33) in eq. (8), deflection w can be expressed as

$$\begin{aligned} w = {} & \left[XY\left(\frac{a}{b}\right)(1-X)\left(1-\left(\frac{aY}{b}\right)\right)\right]^2 \\ & \left[1+\left(\frac{-B_{11}}{B_{12}}\right)XY\left(\frac{a}{b}\right)(1-X)\left(1-\left(\frac{aY}{b}\right)\right)\right] \\ & \times\left[\mathrm{e}^{a_1 t}\left\{\cos b_1 t + \left(\frac{-a_1}{b_1}\right)\sin b_1 t\right\}\right]\,. \end{aligned} \tag{34}$$

The logarithmic decrement Λ of the vibration of visco-elastic plate is given by the standard formula

$$\Lambda = \log_{\mathrm{e}}(w_2/w_1)\,, \tag{35}$$

where w_1 is the deflection at any point on the plate at time period $K = K_1$ and w_2 is the deflection at same point at the time period $K = K_2$ succeeding K_1.

6. Results and discussion

All the numeric results of frequency, logarithmic decrement and deflection for first two modes of vibrations are calculated for an alloy of aluminium, Duralium. In calculation, the following parameters are used [15]: $E_0 = 7.08 \times 10^{10}\,\mathrm{N/m^2}$, $G = 2.632 \times 10^{10}\,\mathrm{N/m^2}$, $\eta = 14.612 \times 10^5\,\mathrm{Ns/m^2}$, $\rho = 2.80 \times 10^3\,\mathrm{kg/m^3}$, $\nu_0 = 0.345$ and $g_0 = 0.01\,\mathrm{m}$.

Frequency for first two modes of vibration at different values of non homogeneity constant, taper constant, aspect ratio and thermal gradient are calculated and tabulated in Tables 1–4.

Table 1. Frequency vs taper constant at $a/b = 1.5$

β	$\alpha = \alpha_1 = 0.0$		$\alpha = 0.2,\ \alpha_1 = 0.1$	
	Mode 1	Mode 2	Mode 1	Mode 2
0.0	64.77	255.98	63.07	249.35
0.2	71.40	282.12	69.65	275.31
0.4	78.27	309.17	76.46	302.13
0.6	85.34	336.90	83.46	329.62
0.8	92.54	365.16	90.59	357.63
1.0	99.86	393.83	97.82	386.03

In Table 1, frequency for both the modes of vibration is obtained at various values of taper constant for the following values of other plate parameters:
i) $\alpha = \alpha_1 = 0.0,\ a/b = 1.5$, ii) $\alpha = 0.2,\ \alpha_1 = 0.1, a/b = 1.5$.

It is clearly seen that frequency for both the modes of vibration increases as taper constant increases from 0.0 to 1.0 for both the cases. Here frequency decreases for both the modes of frequency as values of α and α_1 varying from zero to non-zero.

Table 2. Frequency vs thermal gradient at $a/b = 1.5$

α	$\beta = \alpha_1 = 0.0$		$\beta = 0.2,\ \alpha_1 = 0.1$	
	Mode 1	Mode 2	Mode 1	Mode 2
0.0	64.77	255.98	71.91	284.16
0.2	62.63	247.62	69.65	275.31
0.4	60.42	238.96	67.31	266.16
0.6	58.11	229.98	64.89	256.70
0.8	55.71	220.64	62.36	246.87

In Table 2, frequency for both the modes of vibration is investigated for increasing values of α at different values of β and α_1 for $a/b = 1.5$. Here, authors surprisingly note that frequency decreases for both the modes of vibration as α increases from 0.0 to 0.8. Also, frequency increases as values of β and α_1 change from zero to non-zero.

Effect of aspect ratio on frequency is given in Table 3 with different values of plate's parameters, i. e. $\beta = \alpha = \alpha_1 = 0.0$ and $\beta = \alpha = 0.2,\ \alpha_1 = 0.1$. It can be easily noticed that frequency for both the modes of vibration increases continuously with increasing values of aspect ratio for both the cases.

In Table 4, frequency for both the modes of vibration is reported for increasing values of non homogeneity constant for the following combinations:

a) $\alpha = \beta = 0.0$,

b) $\alpha = \beta = 0.2$,

c) $\alpha = \beta = 0.6$.

Here, authors analyzed that an acute increment is found in both the modes of frequency when α_1 increases. Also, frequency increases when combined values of α and β increase from 0.0 to 0.6.

Table 3. Frequency vs aspect ratio

a/b	$\alpha = \beta = \alpha_1 = 0.0$		$\alpha = \beta = 0.2,\ \alpha_1 = 0.1$	
	Mode 1	Mode 2	Mode 1	Mode 2
0.5	26.21	104.85	28.29	113.26
1.0	38.32	149.97	41.26	161.54
1.5	64.77	255.98	69.65	275.31
2.0	104.87	419.43	112.71	450.90
2.5	157.65	635.48	169.41	683.09

Table 4. Frequency vs non-homogeneity constant at $a/b = 1.5$

α_1	$\alpha = \beta = 0.0$		$\alpha = \beta = 0.2$		$\alpha = \beta = 0.6$	
	Mode 1	Mode 2	Mode 1	Mode 2	Mode 1	Mode 2
0.0	64.77	255.98	69.15	273.32	77.62	306.64
0.05	64.99	256.84	69.39	274.28	77.90	307.79
0.10	65.22	257.76	69.65	275.31	78.19	309.03
0.15	65.47	258.74	69.92	276.41	78.51	310.36

Damping in terms of logarithmic decrement is also calculated and tabulated in Table 5 at $\alpha = \beta = 0.2$ with varying values of aspect ratio for all X and Y. As aspect ratio increases from 0.5 to 1.5, the logarithmic decrement decreases for both the modes of vibration at $\alpha_1 = 0.0$ and $\alpha_1 = 0.15$. Negative values of logarithmic decrement show damping in the vibration of plates.

Table 5. Logarithmic decrement vs aspect ratio at $\alpha = \beta = 0.2$

a/b	$\alpha_1 = 0.0$		$\alpha_1 = 0.15$	
	Mode 1	Mode 2	Mode 1	Mode 2
0.5	–0.1543	–0.6184	–0.1562	–0.6265
1.0	–0.2252	–0.8839	–0.2278	–0.8945
1.5	–0.3803	–1.3369	–0.3846	–1.3294

Deflection for first two modes of vibration is calculated for various values of plate's parameters at different points on rectangular plate in Tables 6–8. The expression of w in equation (34) exhibits the following symmetric properties w.r.t. X, i. e.

$$w(X,(a/b)Y,t) = w(1-X,(a/b)Y,t) \qquad \text{for all } X,Y \text{ in the domain of plate},$$

$$w(0,Y,t) = w(1,Y,t) = w(X,0,t) = w(X,(b/a)Y,t) = 0\,.$$

From the above property, one can obtain

$$w(0.2,(a/b)Y,t) = w(0.8,(a/b)Y,t), \qquad w(0.4,(a/b)Y,t) = w(0.6,(a/b)Y,t)\,,$$

etc. Therefore, authors tabulated deflection only for $X = 0.2$ and $X = 0.4$ at some values of Y.

Deflection for both the modes of vibration with increasing values of non-homogeneity constant for fixed values of α and β, i. e. $\alpha = \beta = 0.0$ and aspect ratio ($= 1.5$) at different values of X, Y and ψ in Table 6. Authors summarized Table 6 as follows:

∗ At $\psi = 0K$, deflection for both the modes of vibration actually increases as non-homogeneity constant increases from 0.0 to 0.1 for each paired values of X and Y.

∗ At $\psi = 5K$, deflection decreases for both the modes of vibration with increasing non-homogeneity constant for each paired values of X and Y.

∗ At fixed value of $Y = 0.2$, first mode of deflection at $\psi = 0K$ and $\psi = 5K$ first increases up to a certain value and then decreases for each value of non-homogeneity constant. But second mode at $\psi = 0K$ and $\psi = 5K$ first decreases and then increases for each value of α_1.

∗ At $Y = 0.6$ both the modes of deflection at $\psi = 0K$ and $\psi = 5K$ first increase up to a certain value and then decrease for each value of non-homogeneity constant.

In Table 7, Deflection is tabulated for different values of plate's parameters as in Table 6 at $\alpha = \beta = 0.6$.

Here, authors noticed that variations of both the modes of deflection in Table 7 are as same as in Table 6 at corresponding values of plate's parameters. Main difference between Table 6 and Table 7 is as follows:

∗ At $\psi = 0K$, deflection for both the modes of vibration increases in Table 7 as compared to Table 6 with respect to corresponding values of plate's parameters.

∗ At $\psi = 5K$ and $X = 0.2$, first mode of deflection decreases in Table 7 as compared to Table 6 while second mode of deflection increases in Table 7 as compared to Table 6 for all values of Y.

∗ At $\psi = 5K$ and $X = 0.4$, deflection for both the modes of vibration increases in Table 7 as compared to Table 6 at corresponding values of plate's parameters.

In Table 8, authors analyzed the effect of aspect ratio on deflection for $\alpha = \beta = 0.2, \alpha_1 = 0.1$ at $\psi = 0K$ and $\psi = 5K$ at various values of X and Y. In order to explain Table 8, authors divided it in two parts on the behalf of aspect ratio and explained as follows:

Case I $0 \le a/b \le 1.0$: In this case deflection (both the modes) first increases and then decreases for all paired values of X and Y.

Case II $1.0 < a/b \le 1.5$: In this case, first mode of deflection varies as same as it varies in case I but second mode of deflection first decreases and then increases as X varies from 0.2 to 0.8.

Table 6. Deflection $\times 10^{-5}$ vs non-homogeneity constant for $\alpha = \beta = 0.0,\ a/b = 1.5$ at $\psi = 0K$ and $\psi = 5K*$

$X \rightarrow$	$\alpha_1 \downarrow$	0.0		0.2		0.4		0.6		0.8		1.0	
$Y \downarrow$		Mode 1	Mode 2	Mode 1	Mode 2	Mode 1	Mode 2	Mode 1	Mode 2	Mode 1	Mode 2	Mode 1	Mode 2
0.2	0	0	0	114.621	39.510	259.837	6.338	259.837	6.338	114.621	39.510	0	0
		0	*0*	*50.446*	*1.809*	*114.357*	*0.290*	*114.357*	*0.290*	*50.446*	*1.809*	*0*	*0*
	0.05	0	0	114.633	39.510	259.877	6.338	259.877	6.338	114.633	39.510	0	0
		0	*0*	*50.333*	*1.804*	*114.108*	*0.289*	*114.108*	*0.289*	*50.333*	*1.804*	*0*	*0*
	0.10	0	0	114.636	39.510	259.890	6.338	259.890	6.338	114.636	39.510	0	0
		0	*0*	*50.187*	*1.798*	*113.779*	*0.289*	*113.779*	*0.289*	*50.387*	*1.798*	*0*	*0*
	0.15	0	0	114.645	39.510	259.909	6.339	259.919	6.339	115.755	39.510	0	0
		0	*0*	*47.163*	*1.793*	*107.427*	*0.288*	*104.427*	*0.288*	*47.163*	*1.793*	*0*	*0*
0.6	0	0	0	20.872	14.959	47.114	27.160	47.114	27.160	20.872	14.959	0	0
		0	*0*	*9.186*	*0.685*	*27.734*	*1.244*	*20.734*	*1.244*	*9.186*	*0.685*	*0*	*0*
	0.05	0	0	20.873	14.959	47.117	27.196	47.117	27.160	20.873	14.959	0	0
		0	*0*	*9.165*	*0.683*	*20.689*	*1.240*	*20.689*	*1.240*	*9.165*	*0.683*	*0*	*0*
	0.10	0	0	20.873	14.959	47.118	27.160	47.118	27.160	20.873	14.959	0	0
		0	*0*	*9.138*	*0.681*	*20.628*	*1.236*	*20.628*	*1.236*	*9.138*	*0.681*	*0*	*0*
	0.15	0	0	20.873	14.959	47.118	27.160	47.118	27.160	20.873	14.959	0	0
		0	*0*	*9.138*	*0.679*	*20.628*	*1.233*	*20.628*	*1.233*	*9.138*	*0.679*	*0*	*0*

All the values written in italics show deflection for both the modes of vibration for $\psi = 5K$.

Table 7. Deflection $\times 10^{-5}$ vs non-homogeneity constant for $\alpha = \beta = 0.6,\ a/b = 1.5$ at $\psi = 0K$ and $\psi = 5K*$

$X \rightarrow$	$\alpha_1 \downarrow$	0.0		0.2		0.4		0.6		0.8		1.0	
$Y \downarrow$		Mode 1	Mode 2	Mode 1	Mode 2	Mode 1	Mode 2	Mode 1	Mode 2	Mode 1	Mode 2	Mode 1	Mode 2
0.2	0	0	0	119.269	39.639	275.526	6.774	275.526	6.774	119.269	39.639	0	0
		0	*0*	*44.616*	*2.889*	*103.068*	*0.494*	*103.068*	*0.494*	*44.616*	*2.889*	*0*	*0*
	0.05	0	0	119.332	39.641	275.738	6.647	275.738	6.647	119.332	39.650	0	0
		0	*0*	*44.485*	*2.962*	*102.789*	*0.507*	*102.789*	*0.507*	*44.485*	*2.962*	*0*	*0*
	0.10	0	0	119.408	39.643	275.992	6.785	275.992	6.785	119.408	39.642	0	0
		0	*0*	*44.347*	*3.045*	*102.500*	*0.521*	*102.500*	*0.521*	*44.347*	*3.045*	*0*	*0*
	0.15	0	0	119.496	39.645	276.289	6.793	276.289	6.793	119.496	39.645	0	0
		0	*0*	*43.933*	*3.139*	*101.578*	*0.538*	*101.578*	*0.538*	*43.933*	*3.139*	*0*	*0*
0.6	0	0	0	21.238	14.969	48.349	27.194	48.349	27.194	21.238	14.969	0	0
		0	*0*	*7.945*	*1.091*	*18.086*	*1.982*	*18.087*	*1.982*	*7.945*	*1.091*	*0*	*0*
	0.05	0	0	21.243	14.970	48.366	27.194	48.366	27.194	21.243	14.970	0	0
		0	*0*	*7.919*	*1.119*	*18.030*	*2.032*	*18.030*	*2.032*	*7.919*	*1.119*	*0*	*0*
	0.10	0	0	21.249	14.970	48.386	27.195	48.386	27.195	21.249	14.970	0	0
		0	*0*	*7.891*	*1.150*	*17.970*	*2.089*	*17.970*	*2.089*	*7.891*	*1.150*	*0*	*0*
	0.15	0	0	21.256	14.970	48.409	27.195	48.409	27.195	21.255	14.970	0	0
		0	*0*	*7.815*	*1.185*	*17.798*	*2.153*	*17.798*	*2.153*	*7.815*	*1.185*	*0*	*0*

All the values written in italics show deflection for both the modes of vibration for $\psi = 5K$.

Table 8. Deflection $\times 10^{-5}$ vs aspect ratio for $\alpha = \beta = 0.2,\ \alpha_1 = 0.1$ at $\psi = 0K$ and $\psi = 5K*$

$X \rightarrow$	$a/b \downarrow$	0.0		0.2		0.4		0.6		0.8		1.0	
$Y \downarrow$		Mode 1	Mode 2	Mode 1	Mode 2	Mode 1	Mode 2	Mode 1	Mode 2	Mode 1	Mode 2	Mode 1	Mode 2
0.2	0.25	0	0	5.891	4.929	13.384	10.138	13.384	10.138	5.981	4.929	0	0
		0	*0*	*4.226*	*1.270*	*9.601*	*2.611*	*9.601*	*2.611*	*4.226*	*1.270*	*0*	*0*
	0.50	0	0	21.200	14.698	48.222	27.190	48.222	27.190	21.200	14.698	0	0
		0	*0*	*14.818*	*3.561*	*37.704*	*6.469*	*33.704*	*6.469*	*14.818*	*3.561*	*0*	*0*
	0.75	0	0	42.104	25.195	95.281	38.214	95.281	38.214	42.104	25.195	0	0
		0	*0*	*27.735*	*4.857*	*62.766*	*7.366*	*62.766*	*7.366*	*27.735*	*4.857*	*0*	*0*
	1.00	0	0	65.899	33.067	148.681	37.872	148.681	37.872	65.899	33.067	0	0
		0	*0*	*39.081*	*4.252*	*88.175*	*4.870*	*88.175*	*4.870*	*39.081*	*4.252*	*0*	*0*
	1.25	0	0	91.021	37.759	205.947	26.186	205.947	26.186	91.021	37.759	0	0
		0	*0*	*46.214*	*2.630*	*104.565*	*1.825*	*104.565*	*1.825*	*46.214*	*2.630*	*0*	*0*
	1.50	0	0	115.639	39.540	263.273	6.438	263.273	6.438	115.639	39.540	0	0
		0	*0*	*47.862*	*1.839*	*108.967*	*0.299*	*108.967*	*0.299*	*47.862*	*1.839*	*0*	*0*

All the values written in italics show deflection for both the modes of vibration for $\psi = 5K$.

7. Comparison and conclusions

Authors compared frequency of present paper for both the modes of vibration with [7] with respect to taper constant (β) in Table 9 and thermal gradient(α) in Table 10, respectively at corresponding values of plate's parameters.

Table 9. Frequency found in present paper vs [7] at $\alpha_1 = 0.1$ and $a/b = 1.5$

β	$\alpha = 0.0$	
	Mode 1	Mode 2
0.0	65.22	257.76
	65.22	*257.76*
0.2	71.91	284.16
	69.34	*273.16*
0.4	78.84	311.46
	73.78	*289.72*
0.6	85.96	339.46
	78.47	*307.29*
0.8	93.22	367.98
	83.38	*325.74*
1.0	100.60	396.92
	88.47	*344.94*

Italics values of frequency are taken from [7].

Table 10. Frequency found in present paper vs [7] at $\alpha_1 = 0.1$ and $a/b = 1.5$

α	$\beta = 0.0$	
	Mode 1	Mode 2
0.0	65.22	257.76
	65.22	*257.76*
0.2	63.07	257.76
	62.16	*245.74*
0.4	60.84	240.66
	58.93	*233.11*
0.6	58.52	231.63
	55.50	*219.75*
0.8	56.11	222.24
	51.81	*205.54*
1.0	53.58	212.44
	47.82	*190.28*

Italics values of frequency are taken from [7].

On behalf of the above comparison, authors concluded the following:

i) Frequency of vibration of rectangular plate can be controlled effectively by choosing appropriate values of taper parameter.

ii) Frequency for both the modes of vibration is more in present paper (linear thickness variation) as compared to [7] (parabolic thickness variation) for non-

homogeneous plate under no thermal condition (zero thermal gradient).

iii) Frequency for both the modes of vibration is more in present paper (bi-directional thermal condition, i.e. linearly in x-direction and parabolic in y-direction) as compared to [7] (bi-parabolic thermal condition) for non-homogeneous plate of uniform thickness (zero taper constant).

iv) Non-homogeneity and aspect ratio directly affect the vibrational properties of visco-elastic tapered plate.

References

[1] A. W. Leissa: *Vibration of plates.* NASA SP, Scientific and Technical Information Division, National Aeronautics and Space Administration, USA, 160, (1969).

[2] A. W. Leissa: *The free vibration of rectangular plates.* Journal of Sound and Vibration *31* (1973), No. 3, 257–293.

[3] R. K. Jain, S. R. Soni: *Free vibrations of rectangular plates of parabolically varying thickness.* Indian Journal of Pure and Applied Mathematics *4* (1973), No. 3, 267–277.

[4] M. S. Dhotarad, N. Ganesan: *Vibration analysis of a rectangular plate subjected to a thermal gradient.* Journal of Sound and Vibration *60* (1978), No. 4, 481–497.

[5] A. Khanna, N. Kaur: *Theoretical study on vibration of non-homogeneous tapered visco-elastic rectangular plate.* Proceedings of the National Academy of Sciences, India, Section A *86* (2016), No. 2, 259–266.

[6] A. Khanna, N. Kaur: *Effect of thermal gradient on vibration of non-uniform visco-elastic rectangular plate.* Journal of The Institution of Engineers (India), Series C *97* (2016), No. 2, 141–148.

[7] A. Khanna, N. Kaur: *Effect of structural parameters on the vibrational response of a visco-elastic rectangular plate with clamped ends.* Proceedings of the Estonian Academy of Sciences *64* (2015), No. 2, 127–138.

[8] J. S. Tomar, A. K. Gupta: *Effect of thermal gradient on frequencies of an orthotropic rectangular plate whose thickness varies in two directions.* Journal of Sound and Vibration *98* (1985), No. 2, 257–262.

[9] B. Singh, V. Saxena: *Transverse vibration of rectangular plate with bi-directional thickness variation.* Journal of Sound and Vibration *198* (1996), No. 1, 51–65.

[10] W. L. Li: *Vibration analysis of rectangular plate with general elastic boundary supports.* Journal of Sound and Vibration *273*, (2004), No. 3, 619–635.

[11] A. K. Gupta, H. Kaur: *Study of the effect of thermal gradient on free vibration of clamped visco-elastic rectangular plate with linearly thickness variation in both directions.* Meccanica *43* (2008), No. 4, 449–458.

[12] S. Chakraverty: *Vibration of plates.* Taylor and Francis *1969.*

[13] R. Lal, Y. Kumar, U. S. Gupta: *Transverse vibrations of non-homogeneous rectangular plates of uniform thickness using boundary characteristic orthogonal polynomials.* International Journal of Applied Mathematics and Mechanics *6* (2010), No. 14, 93–109.

[14] A. K. Gupta, V. Panwar, R. P. Vats: *Vibrations of non-homogeneous rectangular plate of variable thickness in both directions with thermal gradient effect.* International Journal of Applied Mathematics and Mechanics *6* (2010), No. 16, 19–37.

[15] N. Kaur: *Some vibration problems of non-homogeneous tapered rectangular plate with bi-directional temperature variations.* Ph.D. thesis, Maharishi Markandeshwar University, Mullana, Ambala, India (2016).

Received September 18, 2017

Acta Technica *63* No. 3/2018, 369–384

Non-linear delamination fracture in multilayered two-dimensional unsymmetrical functionally graded beam

Victor Iliev Rizov[1]

Abstract. The present paper analyses the delamination fracture behavior of a multilayered two-dimensional unsymmetrical functionally graded cantilever beam configuration. The beam is made of arbitrary number of adhesively bonded vertical layers. A delamination crack is located arbitrary between layers. Thus, the crack arms have different widths. The layers have individual widths and material properties. It is assumed that the material is two-dimensional unsymmetrical functionally graded (a power law is used to describe the variation of the material property in both width and height directions in the cross-section of each layer). The fracture analysis is carried-out assuming non-linear behavior of the material. The delamination fracture behavior is studied in terms of the strain energy release rate. A comparison with the J-integral approach is performed for verification. Parametric investigations are carried-out in order to examine the effects of material gradients in both width and height directions of the layers, crack location along the width of the beam cross-section and the non-linear behavior of the material on the delamination fracture. The results obtained indicate that the delamination fracture performance can be optimized by choosing suitable material gradients and exponents in the design stage of the multilayered two-dimensional unsymmetrical functionally graded beam structure.

Key words. Two-dimensional unsymmetrical functionally graded beam, multilayered structure, delamination fracture, material non-linearity.

1. Introduction

The functionally graded materials are a new class of nonhomogeneous materials which have attracted a considerable amount of attention of the scientific community recently [1]–[3]. The properties of the functionally graded materials vary continuously in one or more spatial directions. In this way, one can optimize the performance of functionally graded structural members and components to external loads. Frac-

[1]Department of Technical Mechanics, University of Architecture, Civil Engineering and Geodesy, 1 Chr. Smirnensky blvd., 1046 – Sofia, Bulgaria; e-mail: V_RIZOV_FHE@UACG.BG

ture is the predominant failure mode for the functionally graded structures to loose their capacity and functionality [4]–[6]. That is why the study of fracture mechanics plays an important role in the design of various components and load-bearing structural members made of functionally graded materials.

An equivalent homogeneous beam of variable depth for evaluation of cracked functionally graded beams has been suggested in [4]. The methods of linear-elastic fracture mechanics have been applied. The compliance approach has been explored for cracked three-point bending beams. It has been found that the equivalent beam with cubic variation of the height captures very well the characteristics of the cracked functionally graded beams. It has been concluded that the compliance concept can be extended for analyzing other cracked functionally graded structural components loaded by concentrated forces.

Delamination fracture analysis of functionally graded beams exhibiting non-linear behavior of the material has been developed in [5]. The material is functionally graded along the height of the beam cross-section (i.e., the beam is one-dimensional functionally graded). It has been shown that the results obtained contribute for a better understanding of regularities of fracture in functionally graded load-bearing structures and components with material non-linearity.

Multilayered functionally graded structural members and components consist of adhesively bonded layers of functionally graded materials. Multilayered structures are frequently used especially in applications where strength, weight or cost are an important issue. However, multilayered structural members are quite susceptible to delamination fracture [7], [8]. The delamination, i.e. the separation of layers, reduces the strength and stiffness, deteriorates the dynamic response and complicates the post-buckling behavior of members loaded in compression. That is why, the delamination is a topic of active research [9].

An analytical study of delamination fracture in a multilayered functionally graded beam structure has been performed with taking into account the non-linear behavior of the material [9]. The material is one-dimensional functionally graded in each layer (the material is functionally graded in the thickness direction of the layer). It has been shown that the analysis developed is a useful tool for the understanding of delamination fracture in multilayered one-dimensional functionally graded beam configurations exhibiting non-linear behavior of the material.

The present paper is devoted to the delamination fracture in a multilayered two-dimensional unsymmetrical functionally graded cantilever beam configuration. A fracture analysis is carried-out in terms of the strain energy release rate with taking into account the material non-linearity. A comparison with the J-integral is performed for verification. The influence of material gradients, crack location along the width of the beam cross-section and the non-linear behavior of the material on the delamination fracture are investigated.

2. Non-linear analysis of the strain energy release rate

This section describes an analysis of the delamination fracture in the multilayered two-dimensional nonsymmetric functionally graded cantilever beam configuration

shown in Fig. 1. The beam consists of an arbitrary number of longitudinal vertical layers with individual widths and material properties. The material in each layer exhibits non-linear behavior. It is assumed that perfect adhesion exists between layers. The beam is clamped in section B. A delamination crack of length a is located arbitrarily between the layers. The widths of the right-hand and left-hand crack arms are denoted as b_1 and b_2, respectively. The beam is loaded by one bending moment M applied at the free end of the right-hand crack arm (Fig. 1). Apparently, the left-hand crack arm is free of stresses. The beam length is denoted by l. The cross-section of the beam is a rectangle of width b, and height $2h$.

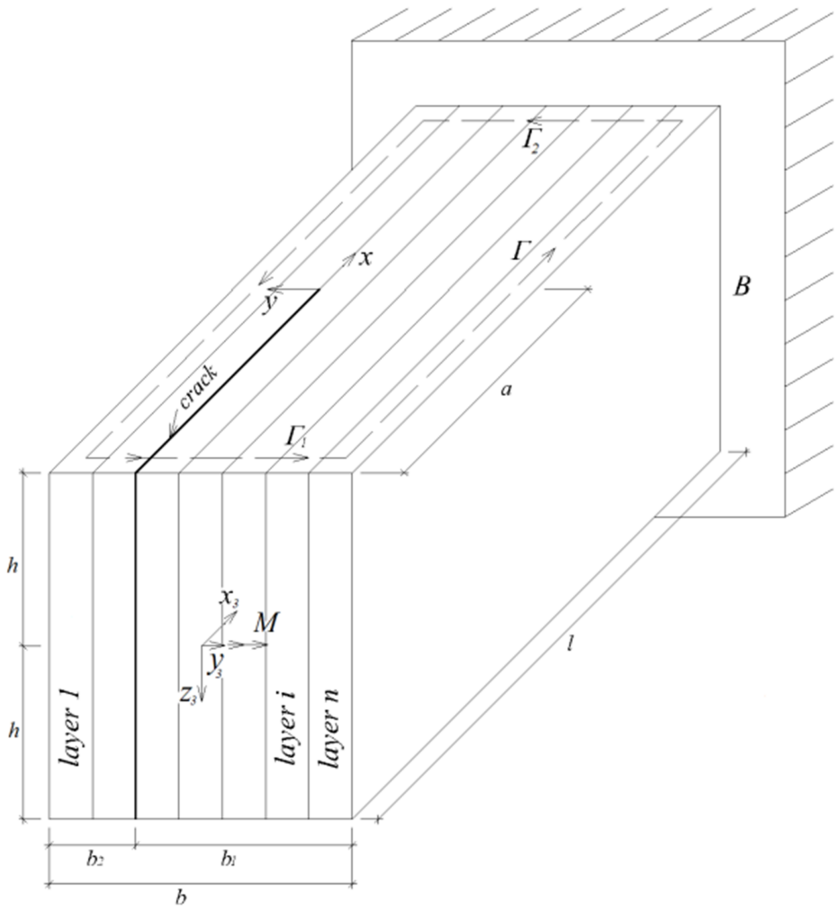

Fig. 1. Geometry and loading of the multilayered two-dimensional unsymmetrical functionally graded cantilever beam

The delamination fracture behavior is analyzed in terms of the strain energy release rate. For this purpose, the following expression for the strain energy release

rate G is applied [9]:

$$G = \frac{\mathrm{d}U^*}{2h\,\mathrm{d}a}\,, \tag{1}$$

where U^* is the complementary strain energy of the beam.

It should be mentioned that the present analysis is carried out by assuming validity of the small strains hypothesis.

Since the left-hand crack arm is free of stresses (Fig. 1), the complementary strain energy cumulated in this crack arm is zero. Therefore, the complementary strain energy of the beam is obtained by summation of the complementary strain energies U^*_{R} and U^*_{U}, cumulated, respectively, in the right-hand crack arm and the uncracked beam portion, $x > 0$:

$$U^* = U^*_{\mathrm{R}} + U^*_{\mathrm{U}}\,. \tag{2}$$

The complementary strain energy in the right-hand crack arm is obtained by summation of the complementary strain energies cumulated in the layers:

$$U^*_{\mathrm{R}} = a \sum_{i=1}^{i=n_{\mathrm{R}}} \int_{-h}^{h} \int_{y_{1i}}^{y_{1i+1}} u^*_{0_{R_i}}\,\mathrm{d}y_1\,\mathrm{d}z_1\,, \tag{3}$$

where n_{R} is the number of layers in the right-hand crack arm, $u^*_{0_{R_i}}$ is the complementary strain energy density in the ith layer, y_{1i} and y_{1i+1} are, respectively, the coordinates of the left-hand and right-hand surfaces of this layer, y_1 and z_1 are the centroidal axes of the cross-section of the right-hand crack arm (Fig. 2).

The complementary strain energy density, in principle, is equal to the area OQR that supplements the area OPQ, enclosed by the stress-strain curve, to a rectangle (Fig. 3). Thus, $u^*_{0_{R_i}}$ is expressed as

$$u^*_{0_{R_i}} = \sigma_i \varepsilon - u_{0_{R_i}}\,, \tag{4}$$

where σ_i is the longitudinal normal stress in ith layer, ε is the longitudinal strain and $u_{0_{R_i}}$ is the strain energy density in this layer.

In principle, the strain energy density is equal to the area OPQ (Fig. 3). Therefore, $u_{0_{R_i}}$ is written as

$$u_{0_{R_i}} = \int_0^{\varepsilon} \sigma_i(\varepsilon)\,\mathrm{d}\varepsilon\,. \tag{5}$$

The material behavior in the ith layer is described by the following non-linear stress-strain relation [10]:

$$\sigma_i = \frac{\varepsilon}{q_i + r_i \varepsilon}\,, \tag{6}$$

where q_i and r_i are material properties. By substituting of (6) into (5) one derives

$$u_{0_{R_i}} = \frac{1}{r_i}\left[\varepsilon - \beta_i \ln\left(\varepsilon + \beta_i\right) + \beta_i \ln\left(\beta_i\right)\right]\,, \tag{7}$$

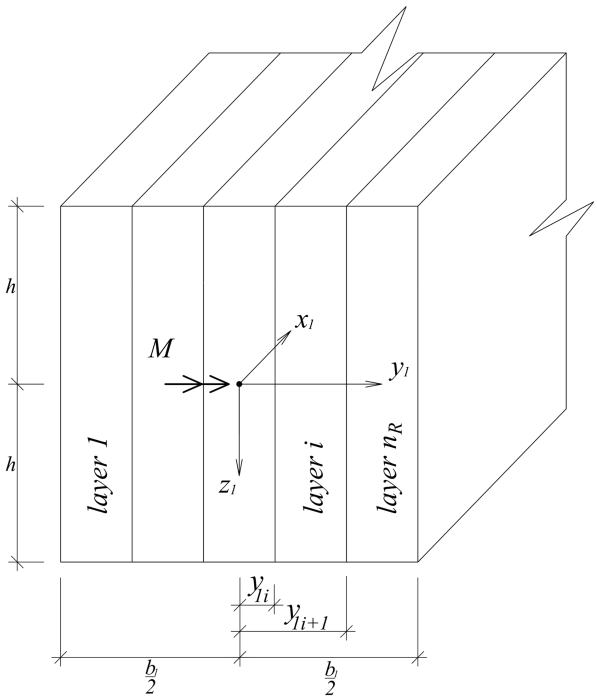

Fig. 2. Free end of the right-hand crack arm

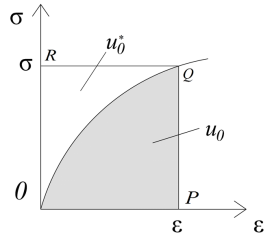

Fig. 3. Non-linear stress-strain curve (the strain energy and the complementary strain energy densities are denoted by u_0 and u_0^*, respectively

where

$$\beta_i = \frac{q_i}{r_i}\,. \tag{8}$$

By combining of (4), (6) and (7) one obtains

$$u^*_{0_{R_i}} = \frac{\varepsilon^2}{q_i + r_i\varepsilon} - \frac{\varepsilon}{r_i} + \frac{\beta_i}{r_i}\ln\left(\varepsilon + \beta_i\right) - \frac{\beta_i}{r_i}\ln\beta_i\,. \tag{9}$$

The distribution of ε is analyzed by applying the Bernoulli's hypothesis for the plane cross-sections because beams of large span to height ratio are under consideration in the present paper. Concerning the distribution of ε, it should also be noted

that since the beam is loaded in pure bending (Fig. 1), the only non-zero strain is ε. Therefore, according to the small strains compatibility equations, ε is distributed linearly. Hence, the distribution of ε in the right-hand crack arm cross-section is expressed as

$$\varepsilon = \varepsilon_{C_1} + \kappa_{y_1} y_1 + \kappa_{z_1} z_1 \,, \tag{10}$$

where ε_{C_1} is the strain in the center of the cross-section, κ_{y_1} and κ_{z_1} are the curvatures of the right-hand crack arm in the x_1y_1 and x_1z_1 planes, respectively.

The quantities, ε_{C_1}, κ_{y_1} and κ_{z_1} are determined from the following equations for equilibrium of the right-hand crack arm cross-section:

$$N_1 = \sum_{i=1}^{i=n_R} \int_{-h}^{h} \int_{y_{1i}}^{y_{1i+1}} \sigma_i \, \mathrm{d}y_1 \, \mathrm{d}z_1 \,, \tag{11}$$

$$M_{y_1} = \sum_{i=1}^{i=n_R} \int_{-h}^{h} \int_{y_{1i}}^{y_{1i+1}} \sigma_i z_1 \, \mathrm{d}y_1 \, \mathrm{d}z_1 \,, \tag{12}$$

$$M_{z_1} = \sum_{i=1}^{i=n_R} \int_{-h}^{h} \int_{y_{1i}}^{y_{1i+1}} \sigma_i y_1 \, \mathrm{d}y_1 \, \mathrm{d}z_1 \,, \tag{13}$$

where N_1 is the axial force, M_{y_1} and M_{z_1} are the bending moments about y_1 and z_1 axes, respectively. Figure 2 shows that

$$N_1 = 0, M_{y_1} = M, M_{z_1} = 0 \,. \tag{14}$$

The present study is performed by assuming that the material property q_i varies in both width (y_1 axis) and height (z_1 axis) directions of the ith layer according to the following power law:

$$q_i = (q_{E_i} - q_{D_i}) \left(\frac{y_1 - y_{1i}}{y_{1i+1} - y_{1i}} \right)^{f_i} + (q_{H_i} - q_{D_i}) \left(\frac{z_1}{2h} + \frac{1}{2} \right)^{f_i} + q_{D_i} \,, \tag{15}$$

where

$$y_{1i} \le y_1 \le y_{1i+1}, \; -h \le z_1 \le h \,. \tag{16}$$

In (15), q_{D_i}, q_{E_i}, q_{H_i} and f_i are material properties.

By substituting of (6), (10) and (15) into (11), (12) and (13), one arrives at

$$\begin{aligned} N_1 = \sum_{i=1}^{i=n_R} \Bigg[\quad & 2h\eta_i \left(\varepsilon_{C_1} \mu_i + \frac{h^2}{3} \kappa_{z_1} \omega_i + \frac{h^2}{3} \varepsilon_{C_1} \zeta_i \right) + \\ & + h\chi_i \left(\varepsilon_{C_1} \nu_i + \kappa_{y_1} \mu_i + \frac{h^2}{3} \zeta_i \kappa_{y_1} + \frac{h^2}{3} \rho_i \kappa_{z_1} \right) + \\ & + \frac{2}{3} h \upsilon_i \left(\kappa_{y_1} \nu_i + \varepsilon_{C_1} \theta_i \right) + \frac{h}{2} \kappa_{y_1} \theta_i \varphi_i \quad \Bigg] , \end{aligned} \tag{17}$$

$$M_{y_1} = \sum_{i=1}^{i=n_R} \Bigg[\quad 2h^3\eta_i \left(\frac{1}{3}\varepsilon_{C_1}\omega_i + \frac{1}{3}\kappa_{z_1}\mu_i + \frac{h^2}{5}\kappa_{z_1}\zeta_i \right) + \\ + \frac{h^3}{3}\chi_i \left(\kappa_{y_1}\omega_i + \kappa_{z_1}\nu_i + \varepsilon_{C_1}\rho_i \right) + \\ + \frac{2}{9}h^3\upsilon_i \left(\kappa_{y_1}\rho_i + \kappa_{z_1}\theta_i \right) \quad \Bigg] , \tag{18}$$

$$M_{z_1} = \sum_{i=1}^{i=n_R} \Bigg[\quad h\chi_i \left(\varepsilon_{C_1}\mu_i + \frac{h^2}{3}\kappa_{z_1}\omega_i + \frac{h^2}{3}\chi_i\varepsilon_{C_1}\zeta_i \right) + \\ + \frac{2}{3}h\upsilon_i \left(\varepsilon_{C_1}\nu_i + \kappa_{y_1}\mu_i + \frac{h^2}{3}\zeta_i\kappa_{y_1} + \frac{h^2}{3}\kappa_{z_1}\rho_i \right) + \\ + \frac{h}{2}\varphi_i \left(\kappa_{y_1}\nu_i + \varepsilon_{C_1}\theta_i \right) + \frac{2}{5}h\kappa_{y_1}\theta_i\psi_i \quad \Bigg] , \tag{19}$$

where

$$\eta_i = y_{1i+1} - y_{1i} , \tag{20}$$

$$\chi_i = y_{1i+1}^2 - y_{1i}^2 , \tag{21}$$

$$\upsilon_i = y_{1i+1}^3 - y_{1i}^3 , \tag{22}$$

$$\varphi_i = y_{1i+1}^4 - y_{1i}^4 , \tag{23}$$

$$\psi_i = y_{1i+1}^5 - y_{1i}^5 , \tag{24}$$

$$\delta_i = \frac{q_{E_i} - q_{D_i}}{\eta_i^{f_i}} , \tag{25}$$

$$\lambda_i = \frac{q_{H_i} - q_{D_i}}{(2h)^{f_i}} , \tag{26}$$

$$\gamma_i = \delta_i \left(-y_{1i} \right)^{f_i} + \lambda_i h^{f_i} + q_{D_i} + r_i\varepsilon_{C_1} , \tag{27}$$

$$\mu_i = \frac{1}{\gamma_i} , \tag{28}$$

$$\nu_i = -\frac{\delta_i f_i \left(-y_{1i} \right)^{f_i - 1} + r_i\kappa_{y_1}}{\gamma_i^2} , \tag{29}$$

$$\omega_i = -\frac{\lambda_i f_i h^{f_i - 1} + r_i\kappa_{z_1}}{\gamma_i^2} , \tag{30}$$

$$\theta_i = \frac{1}{2\gamma_i^3}\left\{-\delta_i f_i\left(f_i-1\right)\left(-y_{1i}\right)^{f_i-2}\gamma_i + 2\left[\delta_i f_i\left(-y_{1i}\right)^{f_i-1} + r_i\kappa_{y_1}\right]^2\right\}, \tag{31}$$

$$\rho_i = \frac{2}{\gamma_i^3}\left[\delta_i f_i\left(-y_{1i}\right)^{f_i-1} + r_i\kappa_{y_1}\right]\left(\lambda_i f_i h^{f_i-1} + r_i\kappa_{z_1}\right), \tag{32}$$

$$\zeta_i = \frac{1}{2\gamma_i^3}\left[-\lambda_i f_i\left(f_i-1\right)h^{f_i-2}\gamma_i + 2\left(\lambda_i f_i h^{f_i-1} + r_i\kappa_{z_1}\right)^2\right]. \tag{33}$$

At $n_R = 1$, $q_{E_i} = q_{H_i} = q_{D_i}$ and $r_i \to 0$, equations (17), (18) and (19) transform into

$$N_1 = 2hb_1\varepsilon_{C_1}\frac{1}{q_{D_i}}, \tag{34}$$

$$M_{y_1} = \frac{2}{3}h^3 b_1\kappa_{z_1}\frac{1}{q_{D_i}}, \tag{35}$$

$$M_{Z_1} = \frac{1}{6}hb_1^3\kappa_{y_1}\frac{1}{q_{D_i}}. \tag{36}$$

It should be noted that (34), (35) and (36) are exact matches of the equations for equilibrium of linear-elastic homogeneous beam of rectangular cross-section of width b_1 and height $2h$. This fact is an indication for the consistency of equations (17), (18) and (19) since at $r_i \to 0$ the non-linear stress-strain relation (6) transforms into the Hooke law assuming that $1/q_{D_i}$ is the modulus of elasticity.

Equations (17), (18) and (19) should be solved with respect to ε_{C_1}, κ_{y_1} and κ_{z_1} by using the MatLab computer program.

The complementary strain energy cumulated in the noncracked beam portion is written as

$$U_{\mathrm{U}}^* = (l-a)\sum_{i=1}^{i=n}\int_{-h}^{h}\int_{y_{2i}}^{y_{2i+1}} u_{0_{U_i}}^*\,\mathrm{d}y_2\,\mathrm{d}z_2, \tag{37}$$

where n is the number of layers in the noncracked beam portion, y_{2i} and y_{2i+1} are, respectively, the coordinates of the left-hand and the right-hand surfaces of the ith layer, $u_{0_{U_i}}^*$ is the complementary strain energy density in the same layer, y_2 and z_2 are the centroidal axes of the cross-section of the noncracked beam portion.

The complementary strain energy density in the ith layer of the noncracked beam portion is obtained by formula (9). For this purpose, ε and q_i are replaced, respectively, with ε_{U} and q_{U_i}. The distribution of material property, q_{U_i}, is expressed by replacing of y_1, z_1, y_{1i} and y_{1i+1}, respectively, with y_2, z_2, y_{2i} and y_{2i+1} in formula (15). The distribution of the longitudinal strains ε_{U} in the cross-section of the noncracked beam portion is obtained by formula (10). For this purpose, y_1, z_1, ε_{C_1}, κ_{y_1} and κ_{z_1} are replaced, respectively, with y_2, z_2, ε_{C_2}, κ_{y_2} and κ_{z_2}, where ε_{C_2} is the strain in the center of the cross-section of the noncracked beam portion, κ_{y_2} and κ_{z_2} are, respectively, the curvatures in the x_2y_2 and x_2z_2 planes. The quantities ε_{C_2}, κ_{y_2} and κ_{z_2} are determined from the equilibrium equations (17), (18) and (19).

For this purpose, N_1, M_{y_1}, M_{z_1}, n_{R}, ε_{C_1}, κ_{y_1}, κ_{z_1}, η_i, χ_i, υ_i, φ_i, ψ_i, δ_i, γ_i, μ_i, ν_i, ω_i, θ_i, ρ_i and ζ_i are replaced, respectively, with N_2, M_{y_2}, M_{z_2}, n, ε_{C_2}, κ_{y_2}, κ_{z_2}, η_{Ui}, χ_{Ui}, υ_{Ui}, φ_{Ui}, ψ_{Ui}, δ_{Ui}, γ_{Ui}, μ_{Ui}, ν_{Ui}, ω_{Ui}, θ_{Ui}, ρ_{Ui} and ζ_{Ui}, where N_2 is the axial force in the un-cracked beam portion, M_{y_2} and M_{z_2} are the bending moments about y_2 and z_2 axes (it is obvious that $N_2 = 0$, $M_{y_2} = M$ and $M_{z_2} = 0$). The quantities η_{Ui}, χ_{Ui}, υ_{Ui}, φ_{Ui}, ψ_{Ui}, δ_{Ui}, γ_{Ui}, μ_{Ui}, ν_{Ui}, ω_{Ui}, θ_{Ui}, ρ_{Ui} and ζ_{Ui} are obtained by replacing of y_{1i}, y_{1i+1}, ε_{C_1}, κ_{y_1} and κ_{z_1}, respectively, with y_{2i}, y_{2i+1}, ε_{C_2}, $\kappa_{y_2}$and κ_{z_2} in formulae (20)–(33).

By combining of (1), (2), (3) and (37), one arrives at

$$G = \frac{1}{2h} \sum_{i=1}^{i=n_R} \int_{-h}^{h} \int_{y_{1i}}^{y_{1i+1}} u^*_{0_{R_i}} \, \mathrm{d}y_1 \, \mathrm{d}z_1 - \frac{1}{2h} \sum_{i=1}^{i=n} \int_{-h}^{h} \int_{y_{2i}}^{y_{2i+1}} u^*_{0_{U_i}} \, \mathrm{d}y_2 \, \mathrm{d}z_2 \,. \tag{38}$$

Formula (38) expresses the strain energy release rate in the multilayered two-dimensional functionally graded beam (Fig. 1). The integration in (38) should be performed by using the MatLab computer program.

The J-integral approach [11] is applied in order to verify (38). The integration is carried out along integration contour, Γ, which coincides with the beam contour (Fig. 1). Apparently, the J-integral is non-zero only in segments Γ_1 and Γ_2 of the integration contour, where Γ_1 coincides with the free end of the right-hand crack arm and Γ_2 coincides with the clamping. The J-integral value is obtained by summing of the J-integral values J_{Γ_1} and J_{Γ_2} in segments Γ_1 and Γ_2:

$$J = J_{\Gamma_1} + J_{\Gamma_2} \,. \tag{39}$$

The J-integral in segment Γ_1, is written as

$$J_{\Gamma_1} = \sum_{i=1}^{i=n_R} \int_{y_{1i}}^{y_{1i+1}} \left[u_{0_{R_i}} \cos\alpha - \left(p_{xi} \frac{\partial u}{\partial x} + p_{yi} \frac{\partial v}{\partial x} \right) \right] \mathrm{d}s, \tag{40}$$

where α is the angle between the outwards normal vector to the contour of integration and the crack direction, p_{xi} and p_{yi} are the components of stress vector in the ith layer of the lower crack arm, u and v are the components of displacement vector with respect to the crack tip coordinate system xy (x being directed along the delamination crack), and $\mathrm{d}s$ is a differential element along the contour.

The components of J_{Γ_1} are obtained as

$$p_{xi} = -\sigma_i \,, \tag{41}$$

$$p_{yi} = 0 \,, \tag{42}$$

$$\mathrm{d}s = \mathrm{d}y_1 \,, \tag{43}$$

$$\cos\alpha = -1\,. \tag{44}$$

The stress σ_i, in n (41) is obtained by (6). The partial derivative, $\partial u/\partial x$, in (40) is written as

$$\frac{\partial u}{\partial x} = \varepsilon = \varepsilon_{C_1} + \kappa_{y_1} y_1 + \kappa_{z_1} z_1. \tag{45}$$

The J-integral in segment Γ_2 of the integration contour (Fig. 1) is expressed as

$$J_{\Gamma_2} = \sum_{i=1}^{i=n} \int_{y_{2i}}^{y_{2i+1}} \left[u_{0_{U_i}} \cos\alpha_U - \left(p_{xUi} \frac{\partial u}{\partial x_U} + p_{yUi} \frac{\partial v}{\partial x_U} \right) \right] \mathrm{d}s_U, \tag{46}$$

where the strain energy density $u_{0_{U_i}}$ in the ith layer of the noncracked beam portion is obtained by formula (7). For this purpose, ε and q_i are replaced, respectively, with ε_{U} and q_{U_i}. The other components of J_{Γ_2} are found as

$$p_{xUi} = \sigma_i\,, \tag{47}$$

$$p_{yUi} = 0\,, \tag{48}$$

$$\mathrm{d}s_U = -\,\mathrm{d}y_2\,, \tag{49}$$

$$\cos\alpha_U = 1\,, \tag{50}$$

$$\frac{\partial u}{\partial x_U} = \varepsilon_{C_2} + \kappa_{y_2} y_2 + \kappa_{z_2} z_2\,. \tag{51}$$

The stress σ_i which participates in (47) is found by replacing of ε and q_i, respectively, with ε_U and q_{U_i} in formula (6).

The average value of the J-integral along the delamination crack front is expressed as

$$J_{\mathrm{av}} = \frac{1}{2h} \int_{-h}^{h} J\,\mathrm{d}z_1\,. \tag{52}$$

By combining of (39), (40), (46) and (52) one arrives at

$$J_{av} = \frac{1}{2h} \sum_{i=1}^{i=n_R} \int_{-h}^{h} \int_{y_{1i}}^{y_{1i+1}} \left[u_{0_{R_i}} \cos\alpha - \left(p_{xi} \frac{\partial u}{\partial x} + p_{yi} \frac{\partial v}{\partial x} \right) \right] ds dz_1 +$$

$$+ \frac{1}{2h} \sum_{i=1}^{i=n} \int_{-h}^{h} \int_{y_{2i}}^{y_{2i+1}} \left[u_{0_{U_i}} \cos\alpha_U - \left(p_{xUi} \frac{\partial u}{\partial x_U} + p_{yUi} \frac{\partial v}{\partial x_U} \right) \right] ds_U dz_1. \tag{53}$$

The integration in (53) should be performed by the MatLab computer program. It should be mentioned that the J-integral value obtained by (53) is exact match of

the strain energy release rate calculated by (38). This fact is a verification of the non-linear delamination fracture analysis developed in the present paper.

3. Parametric investigation

Through this section, results obtained by applying the fracture analysis developed in the previous section are presented. A cantilever beam consisting of three layers of two-dimensional unsymmetrical functionally graded material is considered (Fig. 4a). There is a delamination crack located between layers 2 and 3. The beam is loaded by one bending moment, M, applied at the free end of the right-hand crack arm. A three-layered two-dimensional functionally graded cantilever beam which has a delamination crack located between layers 1 and 2 is also examined (Fig. 4b) in order to investigate the influence of the crack location along the width of the beam cross-section on the delamination fracture behavior. In both beam configurations, the width of each layer is t (Fig. 4). The strain energy release rate is calculated by Eq. (38). It is assumed that $t = 0.004\,\mathrm{m}$, $h = 0.009\,\mathrm{m}$ and $M = 40\,\mathrm{Nm}$. The strain energy release rate is presented in non-dimensional form by using the formula $G_N = Gq_{D_3}/b$. Calculations are performed for both beam configurations shown in Fig. 4 assuming that $q_{H_3}/q_{D_3} = 1.8$, $q_{D_2}/q_{D_3} = 2$, $q_{H_2}/q_{D_2} = 1.4$, $q_{E_2}/q_{D_2} = 1.5$, $q_{D_1}/q_{D_3} = 0.6$, $q_{H_1}/q_{D_1} = 1.3$, $q_{E_1}/q_{D_1} = 1.7$, $r_1 = 0.3q_{D_1}$, $r_2 = 0.1q_{D_2}$, $r_3 = 0.2q_{D_3}$ and $f_1 = f_2 = f_3 = 0.3$. The influence of the material gradient in the width direction of layer 3 on the delamination fracture behavior is analyzed. For this purpose, a ratio of q_{E_3}/q_{D_3}, which characterizes the material gradient introduced in the width direction of layer 3. The strain energy release rate in non-dimensional form is plotted against q_{E_3}/q_{D_3} ratio in Fig. 5 for both three-layered beam configurations is shown in Fig. 4. The curves in Fig. 5 indicate that the strain energy release rate increases with increasing of q_{E_3}/q_{D_3} ratio. This finding is attributed to the decrease of the beam stiffness. Concerning the influence of the crack location along the width of the beam cross-section, one can observe in Fig. 5 that when the crack is located between layers 2 and 3 (refer to Fig. 4a), the strain energy release rate is higher in comparison with the case when the crack is between layers 1 and 2 (refer to Fig. 4b). This is due to the fact that the width of the cross-section of the right-hand crack arm is lower when the crack is located between layers 2 and 3.

The effect of the material gradient in the height direction of layer 3 on the delamination fracture is evaluated too. The three-layered beam configuration shown in Fig. 4a is analyzed. The material gradient in the height direction of layer 3 is characterized by q_{H_3}/q_{D_3} ratio. The strain energy release rate in non-dimensional form is presented as a function of q_{H_3}/q_{D_3} ratio in Fig. 6 at $q_{E_3}/q_{D_3} = 1.8$. It can be observed in Fig. 6 that the strain energy release rate increases with increasing of q_{H_3}/q_{D_3} ratio. The reason of this behavior is the decrease of the beam stiffness. The effect of the non-linear behavior of the material on the delamination fracture is also evaluated. For this purpose, the strain energy release rate obtained assuming linear-elastic behavior of the three-layered two-dimensional functionally graded beam configuration (refer to Fig. 4a) is plotted in non-dimensional form against q_{H_3}/q_{D_3} ratio in Fig. 6 for comparison with the non-linear solution (it should be noted that

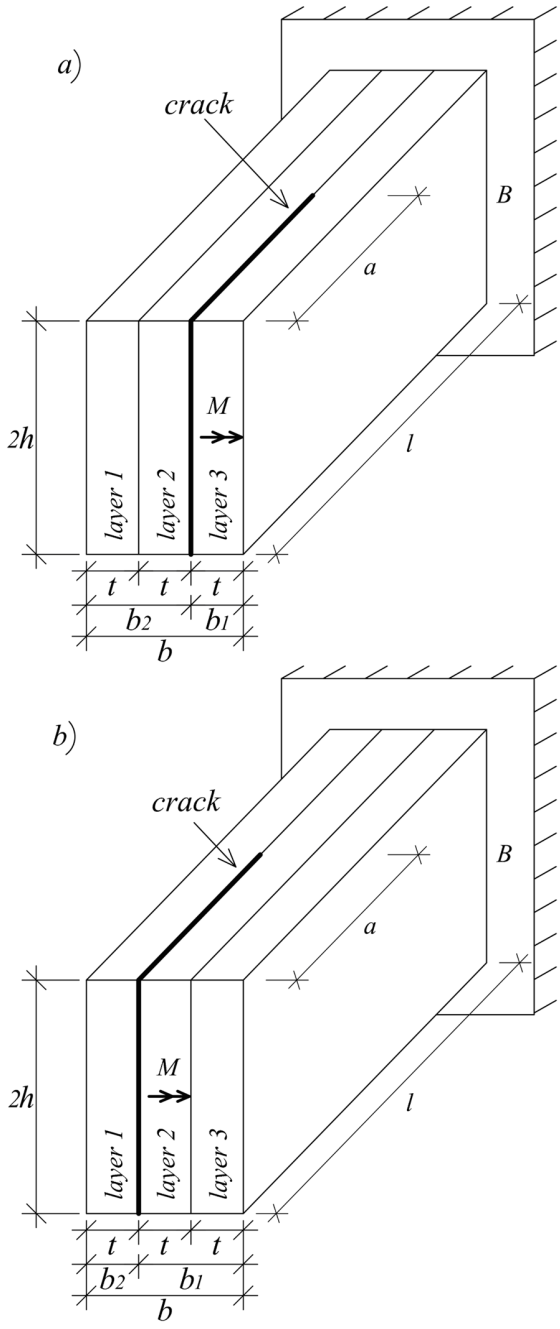

Fig. 4. Two three-layered two-dimensional unsymmetrical functionally graded cantilever beam configurations

the linear-elastic solution is obtained by Eq. (38) at $r_i \to 0$, where $i = 1,\ 2,\ 3$). Figure 6 shows that the non-linear behavior of the material leads to increase of the strain energy release rate. In order to examine the influence of the exponent, f_1, on the delamination fracture behavior, the strain energy release rate in non-dimensional form is plotted as a function of f_1 in Fig. 7 for two q_{D_2}/q_{D_3} ratios at $q_{E_3}/q_{D_3} = 1.9$ and $f_1 = f_2 = f_3$.

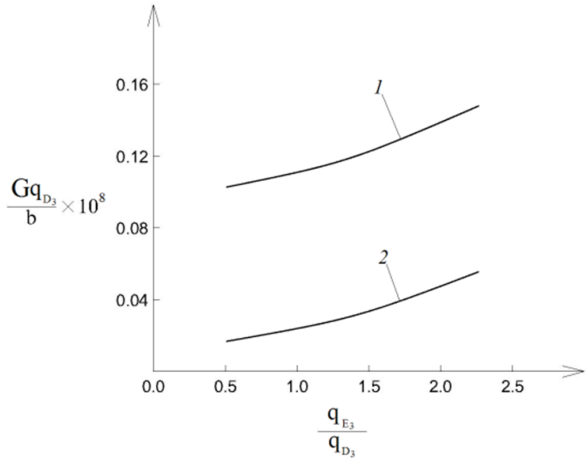

Fig. 5. The strain energy release rate in non-dimensional form plotted against q_{E_3}/q_{D_3} ratio (curve 1–for the beam configuration with a crack located between layers 2 and 3 (refer to Fig. 4a), curve 2–for the beam configuration with a crack located between layers 1 and 2 (refer to Fig. 4a)

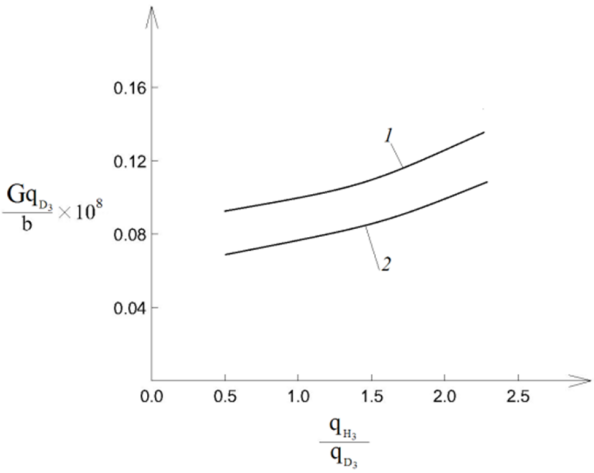

Fig. 6. The strain energy release rate in non-dimensional form presented as a function of q_{H_3}/q_{D_3} ratio (curve 1–at non-linear behavior of material, curve 2–at linear-elastic behavior of material)

The three-layered two-dimensional functionally graded beam configuration shown in Fig. 4a is considered. The curves in Fig. 7 indicate that the increase of f_1 leads to decrease of the strain energy release rate. It can also be seen that the increase of q_{D_2}/q_{D_3} ratio leads to increase of the strain energy release rate (Fig. 7).

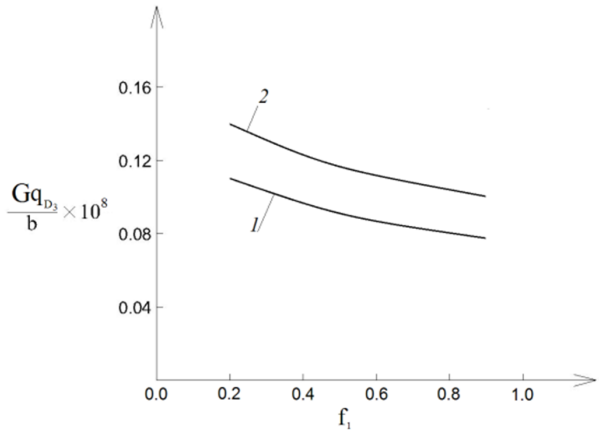

Fig. 7. The strain energy release rate in non-dimensional form plotted as a function of the exponent, f_1, at $q_{D_2}/q_{D_3} = 1.2$ (curve 1) and $q_{D_2}/q_{D_3} = 1.9$ (curve 2)

4. Conclusion

The delamination fracture in the multilayered two-dimensional unsymmetrical functionally graded cantilever beam which consists of an arbitrary number of adhesively bonded longitudinal vertical layers is analyzed. The layers have different widths and material properties. A delamination crack is located arbitrary between layers. The beam is loaded by one bending moment applied at the free end of the right-hand crack arm. The material in each layer exhibits non-linear behavior. Besides, the material is two-dimensional functionally graded in the cross-section of each layer (a power law is applied to describe the variation of the material property, q_i, in both height and width directions of each layer). The delamination fracture behavior is studied in terms of the strain energy release rate. A comparison with the J-integral approach is performed for verification purpose. The strain energy release rate analysis developed in the present paper is applied to investigate the influences of material gradients, crack location and the non-linear behavior of the material on the delamination fracture. The material gradients along the width and the height of the ith layer are characterized by q_{E_i}/q_{D_i} and q_{H_i}/q_{D_i} ratios, respectively. The main findings can be summarized as follows:

1. The strain energy release rate increases as q_{E_i}/q_{D_i} and q_{H_i}/q_{D_i} ratios increase.
2. The increase of the exponent, f_i, of the power law causes a decrement in the strain energy release rate.

3. Findings 1 and 2 indicate that the delamination fracture behavior of the multilayered two-dimensional functionally graded beams can be optimized by choosing suitable material gradients and exponents in the design stage of the beams.

4. The strain energy release rate is greatly influenced by the crack location along the width of the beam cross-section. The increase of the width of the right-hand crack arm leads to decrease of the strain energy release rate.

5. The non-linear behavior of the material causes a significant increase of the strain energy release rate.

References

[1] S. Suresh, A. Mortensen: *Fundamentals of functionally graded materials.* IOM Communications Ltd., London, UK (1998).

[2] M. M. Gasik: *Functionally graded materials: Bulk processing techniques.* International Journal of Materials and Product Technology *39* (2010), No. 1, 20–29.

[3] S. Bohidar, R. Sharma, P. Mishra: *Functionally graded materials: A critical review.* International Journal of Research *1* (2014), No. 7, 289–301.

[4] A. K. Upadhyay, K. R. Y. Simha: *Equivalent homogeneous variable depth beams for cracked FGM beams; Compliance approach.* International Journal of Fracture *144* (2007), No. 3, 209–213.

[5] V. I. Rizov: *Analytical study of elastic-plastic longitudinal fracture in a functionally graded beam.* Strength, Fracture and Complexity *10* (2017), No. 1, 11–22.

[6] V. I. Rizov: *An analytical solution to the strain energy release rate of a crack in functionally graded nonlinear elastic beams.* European Journal of Mechanics - A/Solids *65* (2017), 301–312.

[7] N. A. Dolgov: *Determination of stresses in a two-layer coating.* Strength of Materials *37* (2005), No. 4, 422–431.

[8] N. A. Dolgov: *Analytical methods to determine the stress state in the substrate–coating system under mechanical loads.* Strength of Materials *48* (2016), No. 5, 658–667.

[9] V. I. Rizov: *Delamination fracture in a functionally graded multilayered beam with material nonlinearity.* Archive of Applied Mechanics *87* (2017), No. 6, 1037–1048.

[10] V. V. Petrov: *Non-linear Incremental Structural Mechanics.* Infra-Injeneria, M. (2014).

[11] D. Broek: *Elementary engineering fracture mechanics.* Book Publisher: Springer (1986).

Received 15, 2017

Acta Technica *63* No. 3/2018, 385–406

Thermal instability of double-diffusive natural convection in an inclined open square cavity[1]

O. A. I. Noreldin[2], S. Mondal[3,4], P. Sibanda[2]

Abstract. The thermal instability of fluid layer is investigated in an inclined open square cavity with an inclined magnetic field. A Galerkin-type method is used to solve the equations in the case of linear stability, and in the nonlinear case a truncated Fourier series is used to obtain a system of five general Lorenz type equations. A multi-domain spectral collocation method was used to solve the differential equations that describe the evolution of the disturbances in the nonlinear regime. The influence of the important physical parameters on the thermal instability is investigated. The results are presented in terms of streamlines, isotherms, isoconcentrations, the Nusselt and the Sherwood numbers. The trapping region provide useful information about the trajectories. A limited phase space analysis with trajectories of the disturbances is presented.

Key words. Thermal instability, double-diffusive convection, inclined open cavity, multi-domain spectral collocation method.

1. Introduction

The thermal instability of a Rayleigh–Benard problem with various physical configuration is well reported in Chandrasekhar [1] and Drazin and Reid [2]. Also, Simó et al. [3] examined the dynamics of particle trajectories in a Rayleigh–Benard problem. Laroze and Pleiner [4] studied thermal convection in a nonlinear non-Newtonian magnetic fluid. Double diffusive convection in a fluid-saturated porous medium in a square cavity has received considerable attention in recent years due to its wide range of applications in engineering and science, for example in nuclear reactors, packed beds, the cooling of electronic devices, solar energy, drying technologies and

[1]The authors are grateful to the University of KwaZulu-Natal, South Africa and Amity University, Kolkata, India for the necessary support.

[2]School of Mathematics, Statistics & Computer Science University of KwaZulu-Natal, Pietermaritzburg-3209, South Africa

[3]Department of Mathematics, Amity University, Kolkata, Newtown-700135, West Bengal, India

[4]Corresponding author; e-mail: sabya.mondal.2007@gmail.com

high performance insulation buildings, etc. Studies on natural convective heat transfer in fluid-saturated porous media includes those by Nield and Bejan [5], Ingham and Pop [6, 7], Bejan et al. [8] and Vafai [9]. In these studies it was shown that the effect of the Lorentz force in an electrically conducting fluid is to suppress convection currents by reducing the fluid velocity. For this reason, it has been suggested that the presence of an external magnetic field can thus be an active control mechanism in manufacturing processes.

Le Quere et al. [10] studied thermally driven laminar flow in cavities of rectangular cross-section. Chamkha and Al-Naser [11] investigated the laminar double diffusive convective flow of a binary gas mixture in an inclined rectangular porous enclosure. Wang et al. [12] analyzed natural convection and heat transfer in an inclined porous cavity with time-periodic boundary conditions. Double diffusive convection in an electrically conducting fluid layer in inclined cavities was also studied by Polate et al. [13] and Khanafer et al. [14]. Double diffusive magneto-convection has received considerable attention because of its wide application in oceanography, geophysics, astrophysics and engineering problem, Turner [15] and Rudraiah [16]. Hydromagnetic convection in a conducting fluid flow through a porous medium has been studied by Bian et al. [17]. They found that the temperature and the velocity are significantly modified through the application of a magnetic field. Revnic et al. [18] studied the magnetic field effect on the unsteady free convection flow in a square cavity filled with porous medium and with a constant heat generation. Mansour et al. [19] investigated the effects of an inclined magnetic field on unsteady natural convection in a porous inclined cavity with a heat source in the solid phase.

Recently, Mondal and Sibanda [20] studied unsteady double diffusive convection in an inclined rectangular lid-driven enclosure for different magnetic field angles and non-uniform boundary conditions. They found that different angles of the magnetic field may suppress the convection flow with significant changes in the flow pattern. Narayana et al. [21] studied double diffusive magneto-convection in viscoelastic fluids. They found that the magnetic field has the effect of delaying the onset of convection. Siddheshwar and Pranesh [22, 23] investigated the effect of the magnetic field on the thermal instability under temperature and gravity modulation for an electrically conducting fluid with internal angular momentum. Rudraiah et al. [24] studied finite amplitude convection in a two-component fluid saturated porous layer. They found that subcritical instabilities are possible for such fluid flow. Gaikwad and Kouser [25] studied double diffusive convection in a porous layer saturated with a couple stress fluid with an internal heat source, using linear and weakly nonlinear stability analysis.

The interaction between the fluid velocity and electromagnetic forces gives rise to the flow structure. The electromagnetic effect tends to stabilize the flow and suppress the oscillatory instabilities. The instability in double diffusive convection can occur, depending on whether the solute gradient is stabilizing or destabilizing. If the solute gradient is destabilizing and the temperature gradient is stabilizing, the stationary conductive state becomes unstable through a super-critical bifurcation. On the contradictory, if the solute gradient is stabilizing and the temperature gradient is destabilizing,the instability occurs in the form of a sub-critical bifurcation where

the conductive state may lose stability to a growing oscillatory mode or may even lead to the formation of convection rolls well below the critical Rayleigh number [21]. Lehotzky et al. [26] studied the extension of the spectral element method for stability analysis of time-periodic delay-differential equations.

From the literature, there are many studies on double diffusive convection in square inclined open cavities. To the best of our knowledge none of the studies deal with the analysis of double diffusive convection in open square inclined cavity. The objective of this paper is to investigate thermal instability in double diffusive natural convection in an inclined open cavity. The non-oscillatory and oscillatory convection addressed in this work. The trapping region of the trajectories are determined. The general Lorenz types equations have been solved numerically. The multi-domain spectral collocation method (see [27]) has been used to solve the differential equations. The effects of various controlling parameters are discussed in terms of streamlines, isotherms and iso-concentrations and phase space analysis.

2. Mathematical formulation

Consider the two-dimensional laminar flow of an incompressible and electrically conducting Newtonian fluid which is permeated by a uniform magnetic field $\bar{B}$ with strength B_0 and an inclination angle ϕ. The inclined open square cavity has inclination angle φ from the horizontal plane in an anticlockwise direction. We assume that gravity acts in the vertical direction, all the fluid properties are constant and fluid density variations are neglected except in the buoyancy force term. Under these assumption the continuity, momentum, energy and concentrations equations are given as follows (see Fig. 1):

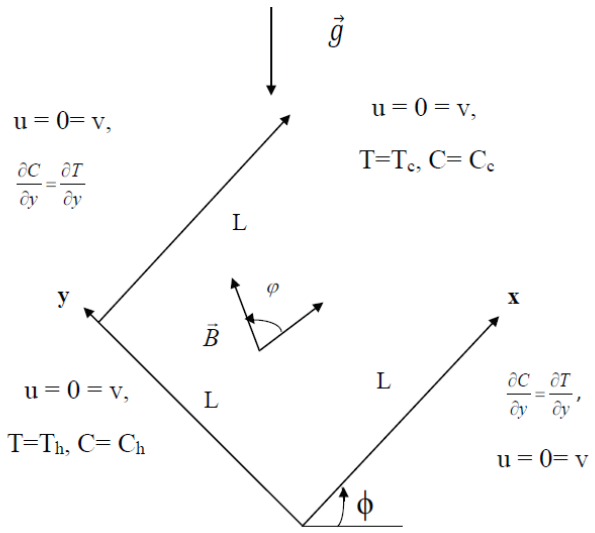

Fig. 1. Physical configuration and coordinate system

$$\frac{\partial u}{\partial x}+\frac{\partial v}{\partial y}=0, \tag{1}$$

$$\rho_0\Big(\frac{\partial u}{\partial t}+u\frac{\partial u}{\partial x}+v\frac{\partial u}{\partial y}\Big)=-\frac{\partial p}{\partial x}+\mu\nabla^2 u+\rho_0\beta_1 g(T-T_\infty)\cos\varphi - \rho_0\beta_2 g(C-C_\infty)\cos\varphi+\sigma|\boldsymbol{B}_0|^2(v\sin\phi\cos\phi-u\sin^2\phi), \tag{2}$$

$$\rho_0\Big(\frac{\partial v}{\partial t}+u\frac{\partial v}{\partial x}+v\frac{\partial v}{\partial y}\Big)=-\frac{\partial p}{\partial y}+\mu\nabla^2 v+\rho_0\beta_1 g(T-T_\infty)\sin\varphi - \rho_0\beta_2 g(C-C_\infty)\sin\varphi+\sigma|\boldsymbol{B}_0|^2(u\sin\phi\cos\phi-v\cos^2\phi), \tag{3}$$

$$\frac{\partial T}{\partial t}+u\frac{\partial T}{\partial x}+v\frac{\partial T}{\partial y}=\alpha\nabla^2 T, \tag{4}$$

$$\frac{\partial C}{\partial t}+u\frac{\partial C}{\partial x}+v\frac{\partial C}{\partial y}=D_{\mathrm{s}}\nabla^2 C. \tag{5}$$

The variables (u,v) are the velocity components in the x and y directions respectively, T, C are the temperature and concentration fields, respectively, g is the gravitation acceleration, p is the pressure and the $\mu, \rho_0, \beta_1, \beta_2, \sigma, \alpha, D_{\mathrm{s}}$ are the viscosity, density, thermal expansion coefficient, solute expansion coefficient, the electrical conductivity, thermal diffusivity and mass diffusivity, respectively.

Introducing the dimensionless variables

$$(X,Y)=\frac{(x,x)}{L},\quad (U,V)=\frac{(u,v)L}{\alpha},\quad P=\frac{pL^2}{\rho_0\alpha^2}, \tag{6}$$

$$\tau=\frac{\alpha t}{L^2},\quad \theta=\frac{T-T_\infty}{T_1-T_\infty},\quad S=\frac{C-C_\infty}{C_1-C_\infty} \tag{7}$$

and substituting equations (6)–(7) into equations (1)–(5) we have

$$\frac{\partial U}{\partial X}+\frac{\partial V}{\partial Y}=0, \tag{8}$$

$$\frac{\partial U}{\partial \tau}+U\frac{\partial U}{\partial X}+V\frac{\partial U}{\partial Y}=-\frac{\partial P}{\partial X}+\mathrm{Pr}\nabla^2 U+\mathrm{Pr}\,(\mathrm{Ra}\,\theta-\mathrm{Rs}\,S)\cos\varphi + \mathrm{Pr}\,\mathrm{Ha}^2(V\sin\phi\cos\phi-U\sin^2\phi), \tag{9}$$

$$\frac{\partial V}{\partial \tau}+U\frac{\partial V}{\partial X}+V\frac{\partial V}{\partial Y}=-\frac{\partial P}{\partial Y}+\mathrm{Pr}\nabla^2 V+\mathrm{Pr}\,(\mathrm{Ra}\,\theta-\mathrm{Rs})\sin\varphi + \mathrm{Pr}\,\mathrm{Ha}^2(U\sin\phi\cos\phi-V\cos^2\phi), \tag{10}$$

$$\frac{\partial \theta}{\partial \tau}+U\frac{\partial \theta}{\partial X}+V\frac{\partial \theta}{\partial Y}=\nabla^2\theta, \tag{11}$$

$$\frac{\partial S}{\partial \tau}+U\frac{\partial S}{\partial X}+V\frac{\partial S}{\partial Y}=\frac{1}{\mathrm{Le}}\nabla^2 S, \tag{12}$$

where $\mathrm{Pr} = \nu/\alpha$ is the Prandtl number, $\mathrm{Ha} = B_0 L/\sqrt{\nu}$ is the Hartmann number, $\mathrm{Ra} = g\beta_1(T_1 - T_\infty)L^3/(\alpha\nu)$ is the thermal Rayleigh number, $\mathrm{Le} = \alpha/D_\mathrm{s}$ is the Lewis number, and $\mathrm{Rs} = g\beta_1(C_1 - C_\infty)L^3/(\alpha\nu)$ is the concentration Rayleigh number.

The basic state solution is described as follows:

$$U_\mathrm{b} = V_\mathrm{b} = 0,\ P_\mathrm{b} = P_\mathrm{b}(Y),\ \theta_\mathrm{b}(Y) = 1 - Y,\ S_\mathrm{b}(Y) = 1 - Y. \tag{13}$$

We superimpose small perturbation on the basic state solution to determine the stability of the fluid and define the fluid quantities as follows:

$$U = U_\mathrm{b} + U',\ \ V = V_\mathrm{b} + V',\ \theta = \theta_\mathrm{b} + \theta',\ S = S_\mathrm{b} + S', \tag{14}$$

where the prime describes a perturbed quantity. Substituting (14) into equations (8)–(12), introducing the stream function ψ as $U' = \partial\psi'/\partial Y, V' = -\partial\psi'/\partial X$ and eliminating the pressure terms in equations (9)–(10) we obtain the perturbed equations

$$\begin{aligned}&\left\{\mathrm{Pr}\nabla^4 - \frac{\partial}{\partial\tau}\nabla^2 + \mathrm{Pr}\,\mathrm{Ha}^2\left(\frac{\partial^2}{\partial X\partial Y}\sin\phi\cos\phi + \frac{\partial^2}{\partial X^2}\cos^2\phi + \frac{\partial^2}{\partial Y^2}\sin^2\phi\right)\right\}\psi' \\ &+ \mathrm{Pr}\,\mathrm{Ra}\left(\frac{\partial\theta'}{\partial Y}\cos\varphi - \frac{\partial\theta'}{\partial X}\sin\varphi\right) - \mathrm{Pr}\,\mathrm{Rs}\left(\frac{\partial S'}{\partial Y}\cos\varphi - \frac{\partial S'}{\partial X}\sin\varphi\right) = \mathcal{J}(\psi', \nabla^2\psi'),\end{aligned} \tag{15}$$

$$\frac{\partial\psi'}{\partial X} + \left(\frac{\partial}{\partial\tau} - \nabla^2\right)\theta' = \mathcal{J}(\psi', \theta'), \tag{16}$$

$$\frac{\partial\psi'}{\partial X} + \left(\frac{\partial}{\partial\tau} - Le^{-1}\nabla^2\right)S' = \mathcal{J}(\psi', S'), \tag{17}$$

where $\mathcal{J}(.,.)$ is the Jacobian determinant.

3. Linear stability analysis

In this section we give a linear stability analysis of the fluid flow. We linearized equations (15)–(17) by neglecting the nonlinear terms. Assume that all perturbed quantities have the following form

$$\psi' = \Psi'(Y)\mathrm{e}^{s\tau}\sin ax, \tag{18}$$

$$\theta' = \Theta'(Y)\mathrm{e}^{s\tau}\cos ax, \tag{19}$$

$$S' = S'(Y)\mathrm{e}^{s\tau}\cos ax, \tag{20}$$

where a is the wave number, and $s = i\omega$, where ω is the frequency of the oscillations. We obtain the following eigenvalue problem by substituting (18)–(20) into (15)-(17)

$$\left\{\Pr(D^2-a^2)^2 - s(D^2-a^2) + \Pr \mathrm{Ha}^2(D^2\sin^2\phi - a^2\cos^2\phi)\right\}\Psi'$$
$$+\Pr \mathrm{Ra}(D\Theta'\cos\varphi + a\sin\varphi\Theta') - \Pr \mathrm{Rs}(DS'\cos\varphi + a\sin\varphi S') = 0, \tag{21}$$
$$a\Psi' + \left\{(D^2-a^2) - s\right\}\Theta' = 0, \tag{22}$$
$$a\Psi' + \left\{\mathrm{Le}^{-1}(D^2-a^2) - s\right\}S' = 0, \tag{23}$$

where $D(\cdot) = \frac{d}{dY}(\cdot)$. Subject to the boundary conditions

$$\Psi' = D^2\Psi' = D\Theta' = DS' = 0 \text{ at } Y = 0 \text{ and } 1. \tag{24}$$

We employ a Galerkin type weighted residual method to obtain approximate solutions of the above system of ordinary differential equations by setting

$$\Psi' = \sum_{n=1}^{N_1} a_n\Psi_n,\ \Theta' = \sum_{n=1}^{N_1} b_n\Theta_n,\ S' = \sum_{n=1}^{N_1} c_nS_n, \tag{25}$$

and choosing the trial functions:

$$\Psi_n = \sin n\pi Y,\ \Theta_n = S_n = \cos n\pi Y. \tag{26}$$

Substituting (25)–(26) into (21)–(23), we obtain a system of $(3 \times N_1)$ linear algebraic equations with $(3 \times N_1)$ unknowns a_n, b_n, c_n for $n = 1, 2, \cdots, N_1$. For simplicity we confine ourselves to the one-term Galerkin approximation with $N_1 = 1$. Thus gives

$$A\tilde{X} = 0 \tag{27}$$

where $\tilde{X} = (a_1, b_1, c_1)$ and

$$A = \begin{pmatrix} \Pr\gamma^2 - s\gamma - \Pr \mathrm{Ha}^2\delta_1 & -\Pr \mathrm{Ra}\delta_2 & \Pr \mathrm{Rs}\delta_2 \\ a & -\gamma - s & 0 \\ a & 0 & -\frac{\gamma}{\mathrm{Le}} - s \end{pmatrix}, \tag{28}$$

where $\gamma = \pi^2 + a^2$. For non-trivial solutions, we require the determinant of (28) to vanish. We obtain the thermal Rayleigh number Ra in terms of other parameters,

$$\mathrm{Ra} = \frac{\left(\gamma^2 - \frac{s}{\Pr}\gamma - \mathrm{Ha}^2\delta_1\right)(\gamma + s)}{a\delta_2} + \mathrm{Rs}\,\mathrm{Le}\frac{\gamma + s}{\gamma + s\,\mathrm{Le}}, \tag{29}$$

where $\delta_1 = \pi^2\sin^2\phi + a^2\cos^2\phi$ and $\delta_2 = \pi\cos\varphi - a\sin\varphi$.

Stationary convection occurs when $s = 0$ and oscillatory convection occurs when $s = iw$. The non-oscillatory and oscillatory convection regimes are discussed below.

3.1. Non-oscillatory convection

Non-oscillatory convection arise when $s = 0$, we obtain the stationary Rayleigh number,

$$\mathrm{Ra}^{st} = \frac{(\pi^2 + a^2)^3 - \mathrm{Ha}^2\delta_1(\pi^2 + a^2)}{a\delta_2} + \mathrm{Rs}\,\mathrm{Le}. \tag{30}$$

When $\mathrm{Rs} = 0$, the magnetic field inclination angle $\phi = 3\pi/2$ and the inclination angle of the cavity $\varphi = \pi/2$, then we obtain the stationary Rayleigh number

$$\mathrm{Ra}^{\mathrm{st}} = \frac{\pi^2 + a^2}{a^2}((\pi^2 + a^2)^2 + \mathrm{Ha}^2\pi^2). \tag{31}$$

This result agrees with the result obtain by Chandreasekhar [1]. We obtain the critical wave number a_{c} and corresponding critical Rayleigh number Ra_{c} by minimizing the stationary Rayleigh number,

$$\frac{\partial}{\partial a^2}(\mathrm{Ra}^{\mathrm{st}}) = \frac{\partial}{\partial a^2}\left(\frac{(\pi^2 + a^2)^3 + \mathrm{Ha}^2\pi^2(\pi^2 + a^2)}{a^2}\right) = 0, \tag{32}$$

which implies that

$$2a^6 + 3\pi^2a^4 - \pi^6 - \pi^4\mathrm{Ha}^2 = 0. \tag{33}$$

By setting $x = a^2/\pi^2$ we obtain

$$2x^3 + 3x^2 - 1 - \mathrm{Ha}^2/\pi^2 = 0. \tag{34}$$

This equation depends only on the Hartmann number hence, the influence of the magnetic field on the onset of convection will be significant. If we assume Ha to be very large then we obtain $a_{\mathrm{c}} = \pi/\sqrt{2}$ and the corresponding critical Rayleigh number Ra_{c} is $Ra_{\mathrm{c}} = \frac{27}{4}\pi^4$.

This result again agrees with Chandrasekhar [1] and Nield and Kuznetsov [28].

3.2. Oscillatory convection

Substituting $s = i\omega$ into equation (29) and imposing the condition $\omega^2 > 0$ (which is required for ω to be real to get over stability) we obtain

$$\mathrm{Ra}^{\mathrm{osc}} = \frac{\left(\gamma^2 - \frac{i\omega}{\mathrm{Pr}}\gamma - \mathrm{Ha}^2\delta_1\right)(\gamma + i\omega)}{a\delta_2} + \mathrm{Rs}\,\mathrm{Le}\frac{\gamma + i\omega}{\gamma + i\omega\mathrm{Le}}. \tag{35}$$

Equation (35) can be reduced to

$$\mathrm{Ra}^{\mathrm{osc}} = \Delta_1 + i\omega\Delta_2, \tag{36}$$

where Δ_1 and Δ_2 are the real and imaginary parts given as follows:

$$\Delta_1 = \frac{\gamma\left(\mathrm{Pr}\left(\gamma^2 - \delta_1\mathrm{Ha}^2\right) + \omega^2\right)}{a\delta_2\mathrm{Pr}} + \frac{\mathrm{Le}\,\mathrm{Rs}\left(\gamma^2 + \omega^2\mathrm{Le}\right)}{\gamma^2 + \omega^2\mathrm{Le}^2}, \tag{37}$$

$$\Delta_2 = \omega\left(\frac{\mathrm{Pr}\left(\gamma^2 - \delta_1\mathrm{Ha}^2\right) - \gamma^2}{a\delta_2\mathrm{Pr}} - \frac{\gamma\left(\mathrm{Le} - 1\right)\mathrm{Le}\,\mathrm{Rs}}{\gamma^2 + \omega^2 Le^2}\right). \tag{38}$$

Since the Rayleigh number is always real, this implies that $\Delta_2 = 0$. Therefore, we obtain the angular frequency ω of the oscillatory convection as

$$\omega^2 = \frac{a\delta_1\mathrm{Pr}(\gamma(\mathrm{Le}-1)\mathrm{Le}\,\mathrm{Rs} - \gamma^2(\mathrm{Pr}(\gamma^2 - \delta_1\mathrm{Ha}^2) - \gamma^2)}{\mathrm{Le}^2(\mathrm{Pr}(\gamma^2 - \delta_2\mathrm{Ha}^2) - \gamma^2)}. \tag{39}$$

The oscillatory convection is then defined by

$$\mathrm{Ra}^{\mathrm{osc}} = \frac{\gamma\left(\mathrm{Pr}\left(\gamma^2 - \delta_1\mathrm{Ha}^2\right) + \omega^2\right)}{a\delta_2\mathrm{Pr}} + \frac{\mathrm{Le}\,\mathrm{Rs}\left(\gamma^2 + \omega^2\mathrm{Le}\right)}{\gamma^2 + \omega^2\mathrm{Le}^2}. \tag{40}$$

4. Nonlinear stability

The nonlinear stability analysis is presented using a minimal truncated Fourier series that consists of two terms. The linear stability analysis fails to provide insights into the convection amplitudes and the rate of heat and mass transfer.

We assume a minimal truncated Fourier series to describe the finite amplitude convection defined by

$$\psi' = A_{11}(\tau)\sin ax \sin \pi y, \tag{41}$$

$$\theta' = B_{11}(\tau)\cos ax \sin \pi y + B_{02}(\tau)\sin 2\pi y, \tag{42}$$

$$S' = C_{11}(\tau)\cos ax \sin \pi y + C_{02}(\tau)\sin 2\pi y, \tag{43}$$

where $A_{11}, B_{02}, B_{02}, C_{11}$ and C_{02} are time dependent convective amplitudes. Nonlinear autonomous equations are obtained after substituting equations (41)–(43) into (15)–(17) and introducing new variables

$$Y_1 = \frac{a\pi}{\gamma}A_{11},\ Y_2 = -\pi R B_{11},\ Y_3 = -\pi R B_{02}, \tag{44}$$

$$Y_4 = -\pi R C_{11},\ Y_5 = -\pi R C_{02},\ \tau^* = \gamma\tau, G = \frac{4\pi^2}{\gamma}. \tag{45}$$

After dropping the asterisk from τ for clarity, we obtain

$$\dot{Y_1} = Pr(-bY_1 + \sin\varphi(Y_2 - NY_4)), \tag{46}$$

$$\dot{Y_2} = RY_1 - Y_2 - Y_1Y_3, \tag{47}$$

$$\dot{Y_3} = \frac{1}{2}Y_1Y_2 - GY_3, \tag{48}$$

$$\dot{Y_4} = RY_1 - Y_1Y_5 - Le^{-1}Y_4, \tag{49}$$

$$\dot{Y_5} = \frac{1}{2}Y_1Y_4 - \frac{G}{\mathrm{Le}}Y_5, \tag{50}$$

where $b = \mathrm{Ha}^2(a^2\cos^2\phi + \pi^2\sin^2\phi)/\gamma^2 - 1$, $R = a^2\mathrm{Ra}/\gamma^3$ is revised Rayleigh number and $N = \mathrm{Rs}/\mathrm{Ra}$ is the buoyancy ratio.

4.1. Steady finite amplitude convection

The general Lorenz type model (46)–(50) has the steady state solutions

$$Y_1^2 = \frac{-B \pm \sqrt{B^2 - 4AC}}{2A}, \quad Y_2 = \frac{2GRY_1}{2G + Y_1^2},$$
$$Y_3 = \frac{RY_1^2}{2G + Y_1^2}, \quad Y_4 = \frac{2G\,\mathrm{Le}\,RY_1}{2G + \mathrm{Le}^2Y_1^2}, \quad Y_5 = \frac{\mathrm{Le}^2RY_1^2}{2G + \mathrm{Le}^2Y_1^2}, \tag{51}$$

where $A = b\,\mathrm{Le}^2$, $B = 2G(b(1+Le) + R\,\mathrm{Le}(\mathrm{Le} - N)\sin\varphi)$ and $C = 4G^2(1 + R(1 - N\,\mathrm{Le})\sin\varphi)$. The equations (46)–(50) are uniformly bounded in time and dissipative in the phase space. To this end, we obtain

$$\sum_{n=1}^{5} \frac{\partial \dot{Y_n}}{\partial Y_n} = -\left(\mathrm{Pr}b + 1 + G + \mathrm{Le}^{-1} + G\,Le^{-1}\right) \tag{52}$$

Equation (52) will always be negative if and only if $b \geq 0$ implies that $\mathrm{Ha}^2 \geq \gamma/(a^2\cos^2\phi + \pi^2\sin^2\phi)$. Therefore, the trajectories may be attracted to a fixed point or limit cycle or any strange attractor. Also, from equations (46)–(50), the volume V_0 at time $t = 0$ is contracted by the flow into a volume element defined by

$$V = V_0 \exp\left\{ -\left(\mathrm{Pr}\,b + 1 + G + \mathrm{Le}^{-1} + G\mathrm{Le}^{-1}\right)t \right\} \tag{53}$$

in time t. Thus, each volume containing the trajectory of this system of equations shrink to zero as $t \to \infty$. Further, the system of equations (46)–(50) are invariant under the transformation $S(Y_n) = -Y_n$ for $n = 1, 2, \cdots, 5$.

4.2. The trapping region

In the classical Lorenz model, the trajectories are known to remain within a finite volume. The trapping region of the trajectories of the system of equations (46)–(50) is a smooth real-valued function $\Sigma(\Lambda(t))$, where $\Lambda(t)$ is the solution of the system of equations (46)–(50) (see [29]). This function has to satisfy the condition $\Sigma(\Lambda(t)) \longrightarrow \infty$ as $\| \Lambda \| \longrightarrow \infty$. The nonlinear terms keep the trajectories confined. We follow the procedure of Sidddheshwar and Titus [29] to find the trapping region $\Sigma(\Lambda)$ as follows

$$\frac{\mathrm{d}\Sigma}{\mathrm{d}t} = Y_1\frac{\mathrm{d}Y_1}{\mathrm{d}t} + \frac{1}{2}Y_2\frac{\mathrm{d}Y_2}{\mathrm{d}t} + (Y_3 - R - \frac{\sin\varphi}{2})\frac{\mathrm{d}(Y_3 - R - \frac{\sin\varphi}{2})}{\mathrm{d}t} + \frac{1}{2}Y_4\frac{\mathrm{d}Y_4}{\mathrm{d}t} + (Y_5 - R + \frac{N\sin\varphi}{2})\frac{\mathrm{d}(Y_5 - R + \frac{N\sin\varphi}{2})}{\mathrm{d}t}. \tag{54}$$

We obtain the trapping region of the system (46)–(50) as an ellipsoid in five dimensions by integrating the above equations which gives

$$Y_1^2 + \frac{Y_2^2}{2} + (Y_3 - R - \frac{\sin\varphi}{2})^2 + \frac{Y_4^2}{2} + (Y_5 - R + \frac{N\sin\varphi}{2})^2 = 2. \tag{55}$$

For the stability of the fixed point we linearized the general autonomous Lorenz-type equations (46)–(50) around the fixed point, we obtain

$$\boldsymbol{J}(0,0,0,0,0) = \begin{pmatrix} -\mathrm{Pr}\,b & \mathrm{Pr}\sin\varphi & 0 & -N\mathrm{Pr}\sin\varphi & 0 \\ R & -1 & 0 & 0 & 0 \\ 0 & 0 & -G & 0 & 0 \\ R & 0 & 0 & -\mathrm{Le}^{-1} & 0 \\ 0 & & 0 & 0 & -G\,\mathrm{Pr}^{-1} \end{pmatrix}. \tag{56}$$

The eigenvalues of equation (56) are

$$\lambda_1 \;=\; -1,\;\; \lambda_2 = -G,\;\; \lambda_3 = -G\,\mathrm{Le}^2,\;\; \lambda_{\pm 4} = \frac{-\zeta \pm \sqrt{\zeta^2 - 4\mathrm{Pr}\eta}}{2}, \tag{57}$$

where $\zeta = \mathrm{Pr}\,b + \mathrm{Le}^{-1}$ and $\eta = b$
$, \mathrm{Le}^{-1} + R\sin\varphi(N - \mathrm{Le}^{-1})$. It's clear that λ_1, λ_2 and λ_3 all have negative real parts. While $\lambda_{\pm 4}$ are have negative real part if and only if $\zeta^2 - 4\mathrm{Pr}\eta < 0$. Hence, the fixed point $(0,0,0,0,0)$ is stable.

5. Method of solution

Since an analytical solution of equations (46)–(50) is not possible, we solved the equations numerically. We used a newly developed multi-domain spectral collocation method to solve this system of equations [27]. To apply the method first divided the interval $[0, T]$ into sub-intervals $\Omega_i = [t_{i-1}, t_i]$ for $i = 1, 2, \cdots, p$ and use the

transformation

$$t = \frac{t_i - t_{i-1}}{2}\tau + \frac{t_i + t_{i-1}}{2} \tag{58}$$

to transform each sub-interval to $[-1, 1]$. The Gauss-Lobatto collocation points are defined by

$$\tau_j^i = \cos\frac{\pi j}{M}, \quad \text{for } j = 0, 1, \cdots M. \tag{59}$$

The derivatives at the collocation points of the unknown functions $Y_{n,r+1}^i(t)$ are given by

$$\frac{\mathrm{d}Y_{n,r+1}^i}{\mathrm{d}t}(\tau_j^i) = \sum_{k=0}^{M} \boldsymbol{D}_{jk} Y_{n,r+1}^i(\tau_j^j) = \boldsymbol{D}\boldsymbol{U}_{n,r+1}^i, \tag{60}$$

where $\boldsymbol{D} = 2D/(t_i - t_{i-1})$. D is the Chebyshev derivative which is given in [27] and $\boldsymbol{U}_{n,r+1}^i = (Y_{n,r+1}^i(\tau_0^i), \cdots Y_{n,r+1}^i(\tau_M^i))$ is the vector of the unknown functions at the collocation points and r is the number of iteration. Now substituting these into equations (46)–(50) and reducing the outcomes in the matrix form

$$\begin{pmatrix} A_{11} & A_{12} & A_{13} & A_{14} & A_{15} \\ A_{21} & A_{22} & A_{23} & A_{24} & A_{25} \\ A_{31} & A_{32} & A_{33} & A_{34} & A_{35} \\ A_{41} & A_{42} & A_{43} & A_{44} & A_{45} \\ A_{51} & A_{52} & A_{53} & A_{54} & A_{55} \end{pmatrix} \begin{pmatrix} \boldsymbol{U}_{1,r+1}^i \\ \boldsymbol{U}_{2,r+1}^i \\ \boldsymbol{U}_{3,r+1}^i \\ \boldsymbol{U}_{4,r+1}^i \\ \boldsymbol{U}_{5,r+1}^i \end{pmatrix} = \begin{pmatrix} \boldsymbol{R}_{1,r}^i \\ \boldsymbol{R}_{2,r}^i \\ \boldsymbol{R}_{3,r}^i \\ \boldsymbol{R}_{4,r}^i \\ \boldsymbol{R}_{5,r}^i \end{pmatrix} \tag{61}$$

where the matrices A_{ij} and $\boldsymbol{R}_n^i$ are given as follows:

$$A_{11} = \boldsymbol{d}(-b\,\mathrm{Pr}), \quad A_{12} = \boldsymbol{d}(\mathrm{Pr}\sin\varphi), \quad A_{14} = \boldsymbol{d}(-N\,\mathrm{Pr}\sin\varphi), \quad A_{13} = A_{15} = \boldsymbol{0}$$

$$A_{21} = \boldsymbol{d}(R - Y_{3,r}^i), \quad A_{22} = \boldsymbol{d}(-1), \quad A_{23} = \boldsymbol{d}(-Y_{1,r}^i), \quad A_{24} = A_{25} = \boldsymbol{0}$$

$$A_{31} = \boldsymbol{d}(\frac{Y_{2,r}^i}{2}), \quad A_{32} = \boldsymbol{d}(\frac{Y_{1,r}^i}{2}), \quad A_{33} = \boldsymbol{d}(-G), \quad A_{34} = A_{35} = \boldsymbol{0}$$

$$A_{41} = \boldsymbol{d}(R - Y_{5,r}^i), \quad A_{44} = \boldsymbol{d}(-\frac{1}{Le}), \quad A_{45} = \boldsymbol{d}(-Y_{1,r}^i), \quad A_{42} = A_{43} = \boldsymbol{0}$$

$$A_{51} = \boldsymbol{d}(\frac{Y_{4,r}^i}{2}), \quad A_{54} = \boldsymbol{d}(\frac{Y_{1,r}^i}{2}), \quad A_{55} = \boldsymbol{d}(-\frac{G}{\mathrm{Le}}), \quad A_{52} = A_{53} = \boldsymbol{0},$$

($\boldsymbol{d}$ denoting diagonal matrix) and the right-hand side matrices are

$$\boldsymbol{R}_{1,r}^i = 0, \quad \boldsymbol{R}_{2,r}^i = -Y_{1,r}^i Y_{3,r}^i, \quad \boldsymbol{R}_{3,r}^i = 1/2(Y_{1,r}^i Y_{2,r}^i),$$

$$\boldsymbol{R}_{4,r}^i = -Y_{1,r}^i Y_{5,r}^i, \quad \boldsymbol{R}_{5,r}^i = 1/2(Y_{1,r}^i Y_{4,r}^i).$$

6. Heat and mass transfers

Heat and mass transfer rates in terms of the Nusselt number (Nu) and Sherwood number (Sh) can be calculated with the help of the above solution method. The dimensionless temperature gradient and concentration gradient of the hot wall are defined as

$$\mathrm{Nu} = -\frac{a}{2\pi}\int_0^{\frac{a}{2\pi}} \left(\frac{\partial \Theta}{\partial Y}\right)|_{Y=0}\,\mathrm{d}X = -2\pi C = \frac{2}{R}Y_3 \tag{62}$$

$$\mathrm{Sh} = -\frac{a}{2\pi}\int_0^{\frac{a}{2\pi}} \left(\frac{\partial S}{\partial Y}\right)|_{Y=0}\,\mathrm{d}X = -2\pi E = \frac{2}{R}Y_5. \tag{63}$$

7. Results and discussion

The main purpose of our investigation was to study the thermal instability in double-diffusive convection in an electrically conducting fluid in an inclined open square cavity using linear and weakly nonlinear stability analysis. Analytical expressions for the stationary and oscillatory Rayleigh numbers have been obtained using linear stability analysis. Moreover, the critical Rayleigh number and corresponding critical waver number for the onset of non-oscillatory convection are determined here. The linear stability theory fails to give a good analysis of nonlinear regime. Therefore, the finite amplitude convection is employed here to study the chaotic behavior of the system and investigate the heat and mass transfer rate of the fluid. So, the nonlinear stability analysis has been discussed here numerically using multi-domain spectral collocation method. Also, the effects of various parameters on heat and mass transfer in terms of Nusselt number and Sherwood number are seen here. In this study, the Lewis number has to change its value from 0.1 to 10, the buoyancy ratio various its value from -10 to 10 and Prandtl number has the value 0.7 and above.

Figure 2 shows the stationary Rayleigh stability curves for various parameters.

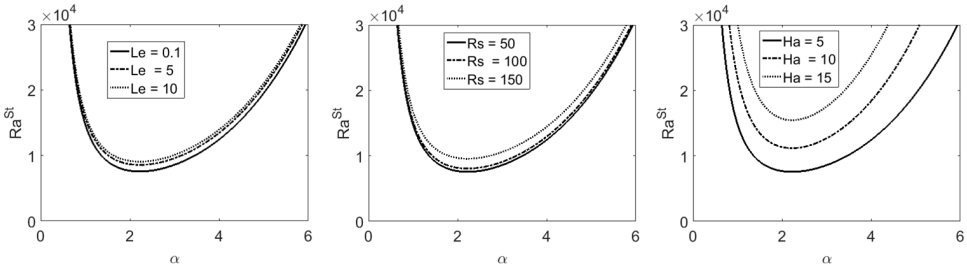

Fig. 2. Effect of critical Rayleigh number Ra with wave number α for various values of the Lewis number Le–left, of the concentration Rayleigh number Rs–middle, of the Hartmann number Ha–right

Its left and middle parts show the effect of increasing the Lewis number Le and concentration Rayleigh number Rs on stationary Rayleigh number. It can be seen

that an increasing value of Le and Rs increase the value of stationary Rayleigh number, which means that both Le and Rs have significant effect on stabilizing the system. The right part of Fig. 2 shows the effect of different values of Hartmann number Ha on the stationary Rayleigh number. It can be observed that an increasing values of Ha increases the value of stationary Rayleigh number which stabilize the system. It is conventional that the magnetic field offers a resistance to the motion of the fluid due to Lorenz force. As a result a huge amount of energy is used by the system to overcome this resistance. Then the convection is delayed the stabilization effect of those parameters on fluid.

Figure 3 shows the effect of different values of Ha on oscillatory Rayleigh number with respect to the concentration Rayleigh number, Lewis number and Prandtl number, respectively. It is seen that increasing value of Ha has a significant effect on increasing oscillatory Rayleigh number which stabilize the system. Hence, the influence of these parameters are used to stabilize the double diffusive convection on an inclined cavity.

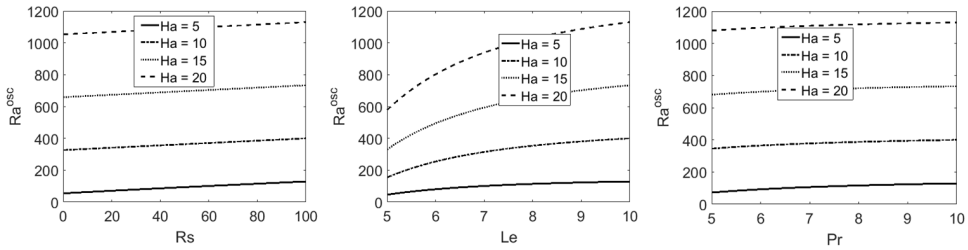

Fig. 3. Effect of Hartmann number Ha on critical oscillatory Rayleigh number Ra^{osc} for various values of the concentration Rayleigh number Rs–left, of the Lewis number Le–middle, of the Prandlt number Pr–right

Figure 4 shows the effect of Ha on behavior of the Nusselt and Sherwood numbers with respect to time.

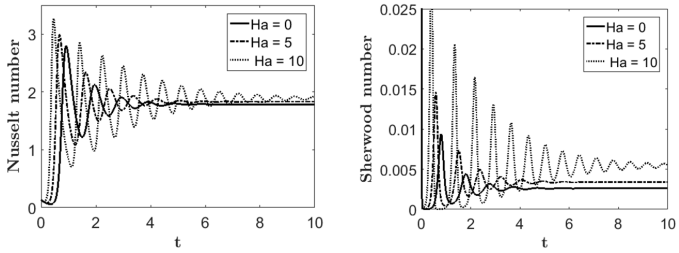

Fig. 4. Variation of average Nusselt number Nu (left) and average Sherwood number Sh (right) with time t for different values of Hartmann number Ha

It was found that increasing Ha increases both the rate of heat and mass transfer. It was also observed that both the Nusselt and Sherwood numbers tend to the state steady faster for small values of Ha than for large values of Ha.

Figure 5 shows the influence of Pr on the Nusselt and Sherwood numbers with respect to time. It is seen that increasing Pr increases both the Nusselt and Sherwood

numbers. Also, it is seen that the rates of heat and mass transfers tend to their steady state after some time faster for large value of Pr than small value of Pr.

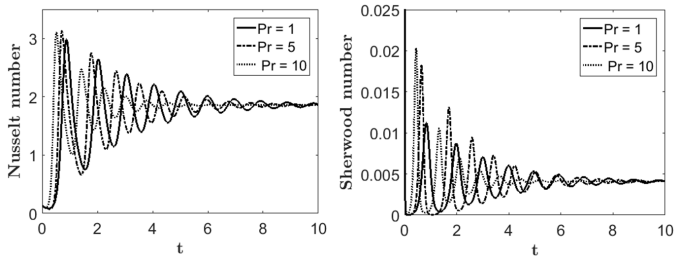

Fig. 5. Variation of average Nusselt number Nu (left) and average Sherwood number Sh (right) with time t for different values of Prandtl number Pr

Figure 6 displays the transient behavior of Nusselt number and Sherwood number for various values of Le.

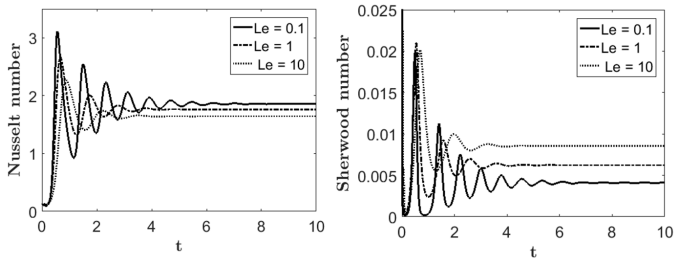

Fig. 6. Variation of average Nusselt number Nu (left) and average Sherwood number Sh (right) with time t for different values of Lewis number Le

The Nusselt number and Sherwood number decrease with increasing value of Le from 0.1 to 10. It is seen that the Nusselt number and Sherwood number attain their steady state faster for the larger values of Le. It is seen that initially Nusselt number and Sherwood number fluctuate and this fluctuation decrease as the time increases to the steady state values. Again, it is observed that increasing Pr increases the amplitude of fluctuations in these transient curves but also helps Nusselt and Sherwood numbers to reach their steady state values much earlier where the opposite trend can be found for Ha. But for increasing values of Le increases the amplitude of fluctuations in these transient curves and the Nusselt and Sherwood numbers reach their steady state values much earlier than small value of Le.

Figures 7–10 display the phase space of Y_iY_j plane for the sensitivity of different revised Rayleigh number Ra. However, these phase space plots are staying within the finiteness of an ellipsoid nature given by equation (55) (within the trapping region). It can be observed that the trajectories occupies a finite phase space region. However this finiteness of the phase space region is due to the nonlinear terms in the system of equations (46)–(50), which turn the trajectories into a finite region. Furthermore, these trajectories enter into trapping region and look like an ellipsoid given by equation (55) toggling between the phase space around the critical points.

The "saddle points" can be observed in "butterfly diagrams". Its seem that various bifurcations reported in Sparrow [30] and Siddheshwar and Titus [29] hold good comparison with the present results. Also our results show that there exist closed orbits.

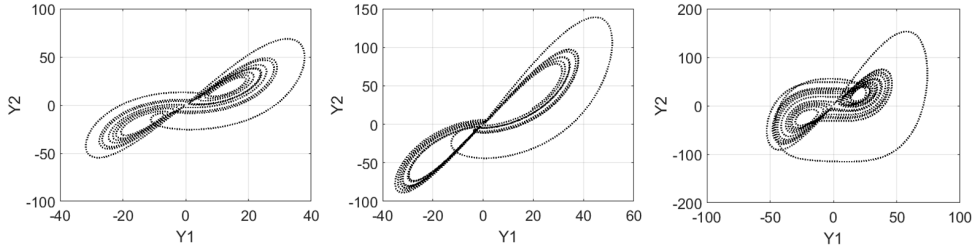

Fig. 7. Evolution of system of nonlinear equation solution shown the sensitivity to Rayleigh number when the solution is projected into Y_1Y_2 plane: left–$R = 50$, middle–$R = 100$, right–$R = 150$

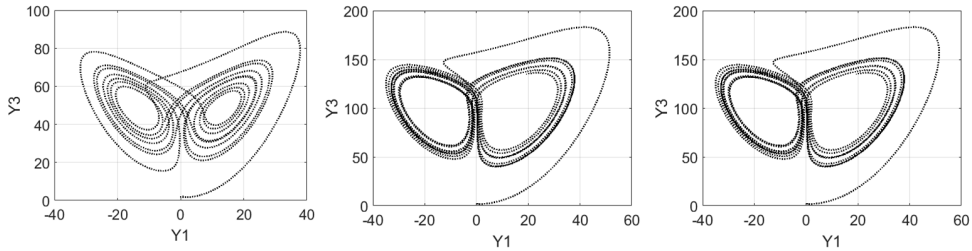

Fig. 8. Evolution of system of nonlinear equation solution shown the sensitivity to Rayleigh number when the solution is projected into Y_1Y_3 plane: left–$R = 50$, middle–$R = 100$, right–$R = 150$

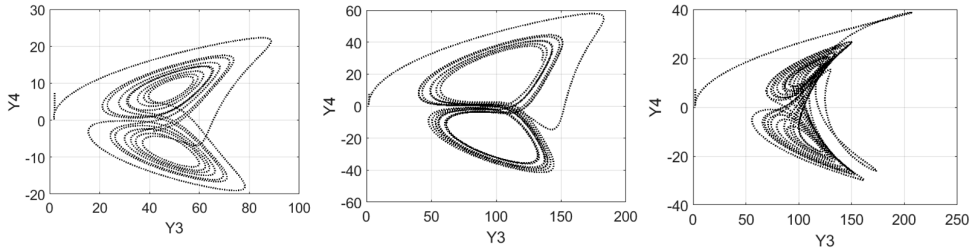

Fig. 9. Evolution of system of nonlinear equation solution shown the sensitivity to Rayleigh number when the solution is projected into Y_3Y_4 plane: left–$R = 50$, middle–$R = 100$, right–$R = 150$

Figure 11 displays the three-dimensional bifurcations which are solution of equations (46)–(50) as the revised Rayleigh number changed from 50 to 150 with fixed Prandtl number Pr = 10 and Lewis number 0.1. These chaotic structures are similar to those in the two-phase space. The only differences are in the shape of the phase space. The phase space in three-dimensional bifurcations are different for different

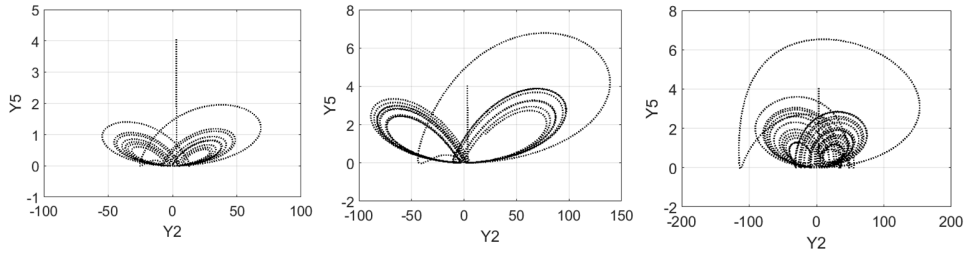

Fig. 10. Evolution of system of nonlinear equation solution shown the sensitivity to Rayleigh number when the solution is projected into Y_2Y_5 plane: left–$R = 50$, middle–$R = 100$, right–$R = 150$

space combinations. Some of these bifurcations have not been seen in literature before. It can, however, be observed that the system stabilizes with increasing values of R.

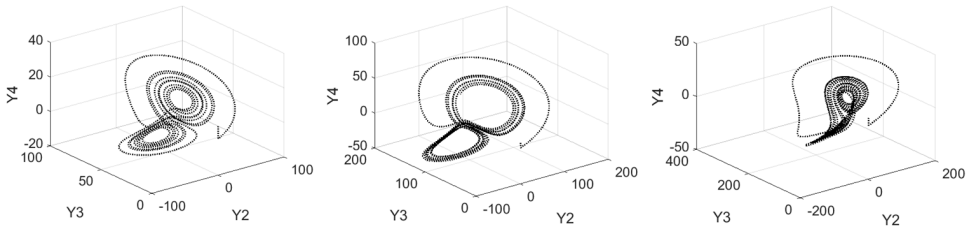

Fig. 11. Evolution of system of nonlinear equation solution shown the sensitivity to Rayleigh number when the solution is projected into $Y_2Y_3Y_4$ plane: left–$R = 50$, middle–$R = 100$, right–$R = 150$

The relative importance of the thermal and solutal buoyancy forces is denoted by the buoyancy ratio N, and is defined as the ratio of the solutal buoyancy force and the thermal buoyancy force. Here, this parameter is varied through the range $-10 < N < 10$. The concentration-dominated opposing flow can be seen when $N = -10$, pure thermal convection dominated flow for $N = 0$, and concentration-dominated aiding flow can be seen for $N = 10$. The flow is steady when $N = 1$, this is because the two buoyancy forces are equal and oppose each other. The buoyancy forces that drive the fluid motion are mainly due to the gradients of temperature if N is sufficiently small which indicates that the mass buoyancy is greater than the thermal buoyancy. Negative value of N represents the opposing nature of two buoyancy forces due to the negative coefficient of concentration expansion. In this limit, the so-called heat transfer-driven flows, the distribution of constituent does not influence the flow pattern and the heat transfer rate. The flow are mainly due to gradients of solute concentration due to solutal gradients if $N > 1$. The negative values of streamlines, isotherms and iso-concentration indicate clockwise rotation and positive value indicate anticlockwise rotation.

Figures 12–14 display the effect of different buoyancy ratios on the streamline, isotherm and iso-concentration profiles for different magnetic field angle when the inclination angle of the cavity is fixed at angle 90° and the bottom wall is heated.

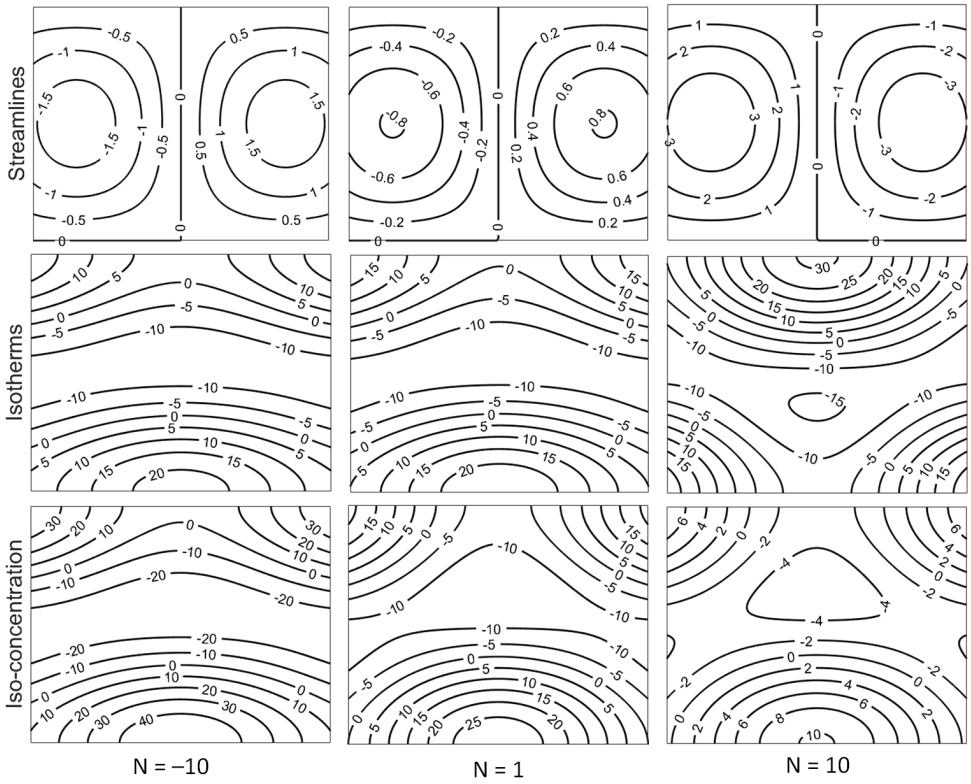

Fig. 12. The streamlines, isotherms and iso-concentration for different values of the buoyancy ratio N, inclination angle $\varphi = 90°$ and magnetic angle $\phi = 45°$

As expected, due to the cold vertical walls, fluids rise up from middle portion of the bottom wall and flow down along the two vertical walls forming two symmetric rolls clockwise and anticlockwise rotations inside the cavity. Actually, the fluid circulation is strongly dependent on buoyancy ratio and different magnetic field angles. Figure 12 illustrates that the streamlines, isotherms and iso-concentrations for magnetic field angle $\phi = 45°$ and different values of N which are mentioned above. It is seen from this figure that the flow is seen to be very week for $N = -10$ and $N = 1$ compared to other streamline graph for $N = 10$. Therefore, the temperature distribution is similar to that with stationary fluid and the heat transfer will be purely conduction. During conduction dominant heat transfer, some isotherms ≤ 5 occur symmetrically near the top corners of the side walls in the enclosure and some isotherm are concentrated at the bottom wall. The other isotherms are smooth curves which span entire enclosure in clockwise and anticlockwise directions. But the isotherms are mainly concentrated near two bottom edges and top wall of the cavity when $N = 0$. And single eddy with clockwise rotation can be found at the center of the cavity with highest value 15. The similar type of iso-concentrations can be found as isotherms for $N = -10$ and $N = 1$. But, it can be seen five different

types of iso-concentration contours due to the higher value of N i.e, $N = 10$ and magnetic field angle $\phi = 45°$.

Figures 13 and 14 show the streamlines,isotherms and iso-concentration for high values of the magnetic field angle ϕ and different values of N compared to Fig. 12. Figure 13 depicts the effect of changing the magnetic field angle to $\phi = 90°$ and different values of N on streamlines, isotherms and iso-concentrations. The main difference compared to Fig. 12 is that the flow is stronger for any value of N compared to the streamline values in Fig. 12. The isotherms are due to heat conduction when $N = -10$ and similar patterns as in Fig. 12 can be observed. However, the isotherms patterns change as N increases in value, showing that the isotherm pattern depends on N. It is also observed that the iso-concentrations depend mainly on the magnetic field angle since large changes can be seen as the magnetic field angles. We found at least four eddies with different patterns of iso-concentrations due to the increasing value of the magnetic field angle.

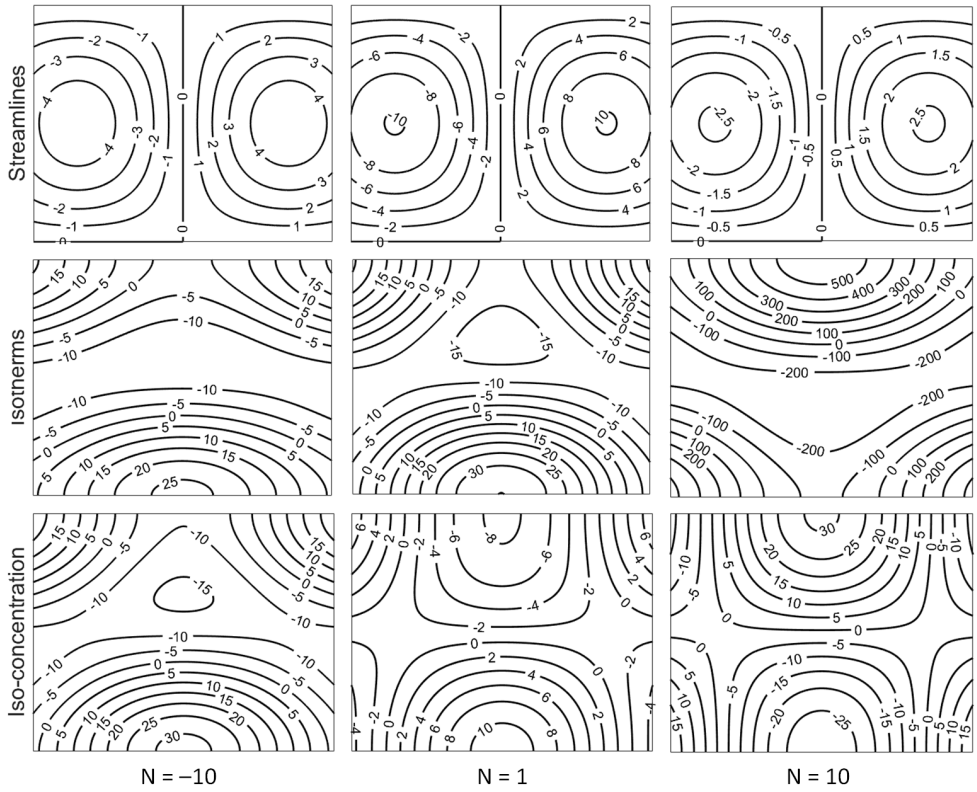

Fig. 13. The streamlines, isotherms and iso-concentration for different values of the buoyancy ratio N, inclination angle $\varphi = 90°$ and magnetic angle $\phi = 90°$

Figure 14 displays the effect of a higher magnetic field angle i.e., 135° for different values of N on the streamlines, isotherms and iso-concentrations. When the magnetic field angle changes from $\phi = 90°$ to $\phi = 135°$, the streamlines pattern does

no change while the values of central eddies changed. As the magnetic field angle increased from 45° to 135°, the isotherm and iso-concentration patterns changed and the values of the central eddies increased. The isotherms are smooth curves which span the entire enclosure in clockwise and anticlockwise directions for higher values of N. Also, as the buoyancy ratio increased from 1 to 10, the iso-concentration eddies became larger due to increasing solutal concentration gradients.

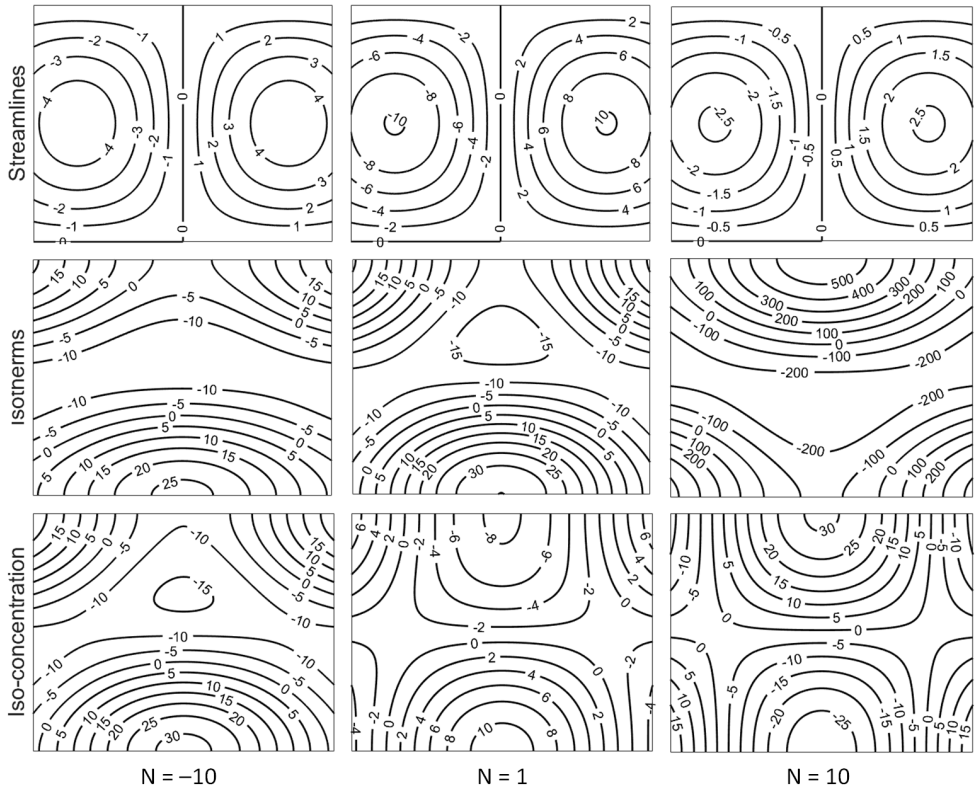

Fig. 14. The streamlines, isotherms and iso-concentration for different values of the buoyancy ratio N, inclination angle $\varphi = 135°$ and magnetic angle $\phi = 90°$

8. Conclusion

In this paper, the focus of the study was on the linear and nonlinear stability analysis of flow in an open inclined square cavity. The effect of Hartmann number on the stationary and oscillatory convection has been presented graphically. The stability of general Lorenz types equations has been studied. The nonlinear equations were solved numerically using a multi-domain spectral collocation approach. The influence of various parameters on the flow has been discussed. The following conclusion can drawn from this study.

1 . The magnetic field parameter has the effect of increasing both stationary and oscillatory convection, hence this has the effect of stabilizing the fluid motion.

2 . The trajectories in phase space of the general Lorenz types equations has been shown to be bounded within a finite ellipsoidal trapping region. Also, the chaotic behaviour is shown for the inclined open square cavity.

3 . The streamlines are seen to be weak when $\phi = 45°$ but stronger for higher value of ϕ than $\phi = 45°$. While some isotherms occur symmetrically near the top corners of the side walls in the enclosure and some isotherm are concentrated at the bottom wall due to the conduction dominant heat transfer for $N = -10$ when $\phi = 45°$ and $90°$ but opposite trend is observed for $\phi = 45°$ and $\phi = 135°$.

References

[1] S. Chandrasekhar: *Hydrodynamic and hydromagnetic stability.* Oxford University Press (1961).

[2] P. G. Drazin, W. H. Reid: *Hydrodynamic stability.* Combridge University Press (1981).

[3] C. Simó, D. Puigjaner, J. Herrero, F. Giralt: *Dynamics of particle trajectories in a Rayleigh–Bénard problem.* Communications in Nonlinear Science and Numerical Simulation *15* (2010), No. 1, 24–39.

[4] D. Laroze, H. Pleiner: *Thermal convection in a nonlinear non-Newtonian magnetic fluid.* Communications in Nonlinear Science and Numerical Simulation *26* (2015), Nos. 1–3, 167–183.

[5] D. A. Nield, A. Bejan: *Convection in porous media.* Springer-Verlag New York (2006).

[6] D. B. Ingham, I. Pop: *Transports phenomena in porous media.* Pergamon, Oxford *3* (2005).

[7] I. Pop, D. B. Ingham: *Convective heat transfer: Mathematical and computional modeling of viscous fluid and porous media.* Pergamon, Oxford (2001).

[8] A. Bejan, I. Dincer, S. Lorente, A. F. Miguel, A. H. Reis: *Porous and complex flows structures in modern technologies.* Springer Nature, Berlin (2004).

[9] K. Vafai: *Handbook of porous media.* CRC Press, Taylor & Francis Group (2005).

[10] P. Le Quere, J. A. C. Humphrey, F. S. Sherman: *Numereical calculation of thermally driven two-dimensinal unsteady laminar flow in cavities of rectangular cross section.* Numerical Heat Transfer *4* (1981), No. 3, 249-283.

[11] A. J. Chamkha, H. Al-Naser: *Double-diffusive convection in an inclined porous enclosure with opposing temperature and concentration gradients.* International Journal of Thermal Sciences *40* (2001), No. 3, 227–244.

[12] G. Wang, Q. Wang, M. Zeng, H. Ozoe: *Numerical study of natural convection heat transfer in an inclined porous cavity with time-periodic boundary conditions.* Transport in Porous Media *74* (2008), No. 3, 293–309.

[13] O. Polat, E. Bilgen: *Laminar natural convection in inclined open shallow cavities.* International Journal of Thermal Sciences *41* (2002), No. 4, 360–368.

[14] K. M. Khanafer, A. J. Chamkha: *Hydromagnetic natural convection from an inlinced porous square enclosure with heat generation.* Numerical Heat Transfer, Part A: Applications *33* (1998), No. 8, 891–910.

[15] J. S. Turner: *Buoyancy effects in fluids.* Cambridge University Press (1979).

[16] N. Rudraiah: *Double-diffusive magnetoconvection.* Pramana *27* (1986), Nos. 1–2, 233–266.

[17] W. Bian, P. Vasseur, E. Bilgen, F. Meng: *Effect of an electromagnetic field on natural convection in an inclined porous medium.* International Journal of Heat and Fluid Flow *17* (1996), No. 1, 36–44.

[18] C. Revnic, T. Grosan, I. Pop, D. B. Ingham: *Magnetic field effect on the unsteady free convection flow in a square cavity filled with a porous medium with a constant heat generation.* International Journal of Heat and Mass Transfer *54* (2011), Nos. 9–10, 1734–1742.

[19] M. A. Mansour, A. J. Chamkha, R. A. Mohamed, M. M. Abd, El-Aziz, S. E. Ahmed: *MHD natural convection in an inclined cavity filled with a fluid saturated porous medium with heat source in the solid phase.* Nonlinear Analysis: Modelling and Control *15* (2010), No. 1, 55–70.

[20] S. Mondal, P. Sibanda: *Unsteady double diffusive convection in an inclined rectangular lid-driven enclosure with different magnetic field angles and non-uniform boundary conditions.* International Journal of Heat and Mass Transfer *90* (2015), 900-910.

[21] M. Narayana, S. N. Gaikwad, P. Sibanda, R. B. Malge: *Double diffusive magneto-convection in viscoelastic fluids.* International Journal of Heat and Mass Transfer *67* (2013), 194–201.

[22] P. G. Siddheshwar, S. Pranesh: *Effect of temperature/gravity modulation on the onset of magneto-convection in weak electrically conducting fluids with internal angular momentum.* Journal of Magnetism and Magnetic Materials *192* (1999), No. 1, 159–176.

[23] P. G. Siddheshwar, S. Pranesh: *Effect of temperature/gravity modulation on the onset of magneto-convection in electrically conducting fluids with internal angular momentum.* Journal of Magnetism and Magnetic Materials *219* (2000), No. 2, 153–162.

[24] N. Rudraiah, P. K. Srimani, R. Friedrich: *Finite amplitude convection in a two-component fluid saturated porous layer.* International Journal of Heat and Mass Transfer *25* (1982), No. 5, 715–722.

[25] S. N. Gaikwad, S. Kouser: *Double diffusive convection in a couple stress fluid saturated porous layer with internal heat source.* International Journal of Heat and Mass Transfer *78* (2014), 1254–1264.

[26] D. Lehotzky, T. Insperger, G. Stepan: *Extension of the spectral element method for stability analysis of time-periodic delay-differential equations with multiple and distributed delays.* Communications in Nonlinear Science and Numerical Simulation *35* (2016), 177–189.

[27] S. S. Motsa, P. Dlamini, M. Khumalo: *A new multistage spectral relaxation method for solving chaotic initial value systems.* Nonlinear Dynamics *72* (2013), Nos. 1–2, 265–283.

[28] A. V. Kuznetsov, D. A. Nield: *Thermal instability in a porous medium layer saturated by a nanofluid: Brinkman model.* Transport in Porous Media *81* (2010), No. 1, 409–422.

[29] P. G. Siddheshwar, P. S. Titus: *Nonlinear Rayleigh-Bénard convection with variable heat source.* Journal of Heat Transfer *135* (2013), No. 12, 122502, Paper No: HT-13-1010.

[30] C. Sparrow: *The Lorenz equations: Bifurcations, chaos and strange attractors.* Springer-Verlag New York (1981).

Received October 12, 2017

Acta Technica *63* No. 3/2018, 407–422

Triple diffusive flow along a stretching sheet with variable thickness in a porous medium

Nancy Samuel[1]

Abstract. The objective of the present study is to investigate the simultaneous effects of thermal and concentration diffusion on a mixed convection boundary layer flow over a stretching sheet with variable thickness immersed in a porous medium. The non-linear coupled partial differential equations governing the flow, thermal and concentration fields are first transformed into a set of non-linear coupled ordinary differential equations by using a set of suitable similarity transformations. The resulting system of non-linear coupled ordinary differential equations is solved using MATLAB program bvp4c. The results are compared with the available data and are found to be in excellent agreement. The effects of various controlling parameters such as porosity, wall thickness, velocity power index, and buoyancy ratio parameters on the fluid flow as well as heat and mass transfer are presented graphically and discussed quantitatively. The heat and mass transfer rate gets suppressed due to the significant effect of wall thickness parameter.

Key words. Triple diffusion, stretching sheet, variable thickness, porous medium, self similar solution.

1. Introduction

The phenomenon of multi-diffusion driven by natural convection in porous media finds its application in migration of moisture through air contained in fibrous insulation, grain storage and dispersion of chemical contaminants through water saturated soil etc. Double diffusive convection or thermo-solutal convection phenomena appears in buoyancy driven flow due to the combination of temperature and concentration gradients. The research on double diffusive convection is being continuously enriched and enlarged by considering new effects like, introduction of vertical and horizontal heterogeneity [1], thermal non-equilibrium [2, 3], taking into account different geometries [4–7] and different fluids [8, 9]. However, in many practical applications the presence of more than two diffusive components has been

[1]Department of Mathematics, Ramaiah Institute of Technology, Bangalore, 560054, India; e-mail: samuelnancy1984@gmail.com

reported. For example, this phenomenon is noticed in thermohaline convection in geothermal systems where the salinity is the sum of comparable concentrations of many salts, convection in magma and substratum of water reservoirs. The impact of a third diffusing component on the onset of double diffusive convection was studied by Poulikakos [10]. He extended the linear stability analysis procedures used in double diffusion and found that the third diffusing component with small diffusivity can significantly change the nature of the convective instabilities in the system. Rionero [11] investigated a triple diffusive fluid mixture saturating a porous horizontal layer, heated from below and salted from above. He obtained conditions sufficient for inhibiting the onset of convection and for global nonlinear stability of thermal conduction solution. Following this work, Khan et al. [12, 13] studied the influence of triple diffusion on boundary layer flow along a horizontal plate immersed in a porous medium subject to a convective boundary condition. They used a Darcy model to analyze two different scenarios where salts with different compositions were dissolved in a fluid saturated porous medium. Very recently, Rana et al. [14] have performed a linear stability analysis on triple diffusive convection in a horizontal layer of nanofluid. Also, Ghalambaz et al. [15, 16] have examined the triple diffusive natural convective heat transfer of a three component mixture comprising of a base fluid and two dissolved pollutants in an enclosure filled with a fluid saturated porous medium.

Studies on boundary layer flow over a stretching sheet have attracted much attention because of its ever growing industrial applications. Practically the stretching sheet may be uneven and it may occur in the engineering relevance more habitually than a flat surface. For a linearly stretching sheet made of incompressible materials, the thickness of the sheet reduces linearly with the distance, owing to the fact that the stretching speed varies linearly to the distance from the slot. For other materials with different extensibility the sheet thickness may change according to other profiles [17]. The study on boundary layer flow over a surface of variable thickness was first initiated by Lee [18]. He has presented an analysis on the flow passing a needle with variable diameter. Later, Fang et al. [19] obtained an analytical and numerical solution to the two-dimensional boundary layer flow due to a non-flat stretching sheet. Eventually, this problem was extended by Subhashini et al. [20] by including the energy equation. They obtained multiple solutions using shooting method and found that thermal boundary layer thicknesses for the first solution were thinner than those of the second solution. Numerical solution for the flow of a Newtonian fluid over a non-flat stretching sheet with slip velocity was studied by Khaddar et al. [21]. Devi and Prakash [22, 23] have analyzed the flow over a variable thickness stretching sheet under the influence of thermal radiation and slip flow in the presence of magnetic field. Ramesh et al. [24] have presented a mathematical analysis for a Casson fluid taking into account the variable thickness and thermal radiation. Further, Patil et al. [25] have obtained non-similar solution for the double diffusive mixed convection flow over a semi-infinite vertical stretching sheet of variable thickness, when the sheet is permeable.

The objective of the present study is to analyze numerically the triple diffusive convection over a vertical stretching sheet of variable thickness. The self-similar

solution of the coupled non-linear partial differential equations governing the flow has been obtained numerically using MATLAB package bvp4c [26]. The results for some particular cases are compared and found to agree with the available results in literature [25].

2. Analysis

Steady two-dimensional laminar mixed convection flow of a viscous incompressible fluid over a semi-infinite vertical stretching sheet with variable thickness embedded in a porous medium is considered. The x-axis is taken along the stretching sheet and the y-axis is taken normal to it. The coordinate system and the flow model are shown in Fig. 1.

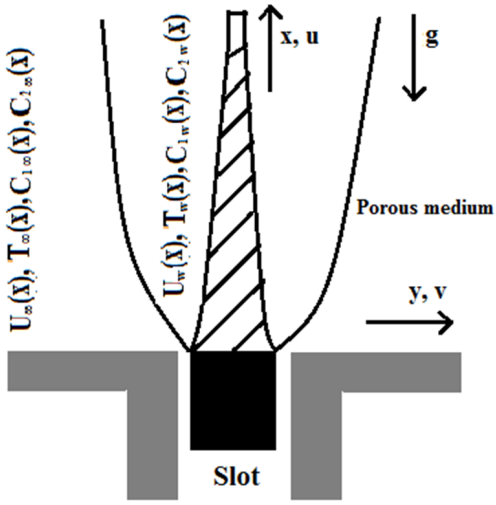

Fig. 1. Physical model and coordinate system

It is assumed that the impermeable sheet stretches with the velocity $U_{\mathrm{w}}(x) = U_0(x+b)^m$, where U_0 is a constant, b is the stretching sheet related constant and m is the velocity power index. The variable thickness of the sheet for the given profile is specified as $y = a(x+b)^{(1-m)/2}$, where a is a coefficient related to the stretching sheet. The acceleration or deceleration of the sheet causes increase or decrease in the thickness of the sheet with distance from the slot. The change in the thickness of the sheet is dependent on the value of the velocity power index m. The value of coefficient a is chosen small so that the sheet can be sufficiently thin. Following Rionero [11], it is assumed that two different chemical components (salts) S_n, $(n = 1, 2)$ have dissolved in the fluid saturated porous medium, which has concentrations C_n, $(n = 1, 2)$, respectively. The buoyancy forces arise due to temperature and concentration difference in the fluid. The Boussinesq approximation is invoked for the fluid properties to relate density changes, and to couple in this way the temperature and concentration fields to the flow field. In this analysis of the flow in

the porous medium, the differential equation governing the fluid motion is based on Darcy's law. Under these assumptions, the governing boundary layer equations are

$$\frac{\partial u}{\partial x}+\frac{\partial v}{\partial y}=0\,, \tag{1}$$

$$u\frac{\partial u}{\partial x}+v\frac{\partial u}{\partial y}=\upsilon\frac{\partial^2 u}{\partial y^2}+g\beta(T-T_\infty)+g\beta_{C1}(C_1-C_{1\infty})+g\beta_{C2}(C_2-C_{2\infty})-\frac{\upsilon}{k}u\,, \tag{2}$$

$$u\frac{\partial T}{\partial x}+v\frac{\partial T}{\partial y}=\alpha\frac{\partial^2 T}{\partial y^2}\,, \tag{3}$$

$$u\frac{\partial C_1}{\partial x}+v\frac{\partial C_1}{\partial y}=D_1\frac{\partial^2 C_1}{\partial y^2}\,, \tag{4}$$

$$u\frac{\partial C_2}{\partial x}+v\frac{\partial C_2}{\partial y}=D_2\frac{\partial^2 C_2}{\partial y^2}\,, \tag{5}$$

where u and v are the velocity components in the x-direction and y-direction, respectively, g is the acceleration due to gravity, υ is the kinematic viscosity, β is the volumetric coefficient of thermal expansion, β_{C1} and β_{C2} are the volumetric coefficients of concentration expansion, k is the permeability of porous medium, α is the thermal diffusivity, D_1 and D_2 are the mass diffusivities of salts S_1 and S_2, respectively, T is the fluid temperature in the boundary layer, C_1 and C_2 are the salt concentrations in the boundary layer. The relevant boundary conditions are

$$u=U_{\mathrm{w}}(x),\ v=0,\ T=T_{\mathrm{w}}(x),\ C_1=C_{1\mathrm{w}}(x),\ C_2=C_{2\mathrm{w}}(x)\ \text{as}\ y=a(x+b)^{(1-m)/2}\,,$$

$$u\to 0,\ T\to T_\infty,\ C_1\to C_{1\infty},\ C_2\to C_{2\infty}\ \text{as}\ y\to\infty\,. \tag{6}$$

In order to obtain similarity solutions the velocity, temperature and the concentrations at the wall are considered in the following form

$$U_{\mathrm{w}}(x)=U_0(x+b)^m,\ T_{\mathrm{w}}(x)=T_\infty+T_0(x+b)^{2m-1},$$

$$C_{1\mathrm{w}}(x)=C_{1\infty}+C_{10}(x+b)^{2m-1},\ C_{2\mathrm{w}}(x)=C_{2\infty}+C_{20}(x+b)^{2m-1}\,. \tag{7}$$

The following similarity transformations

$$\eta=y\left(\frac{U_0}{\upsilon}\right)^{1/2}(x+b)^{(m-1)/2},\ \psi=(\upsilon U_0)^{1/2}(x+b)^{(m+1)/2}f(\eta),$$

$$\theta(\eta)=\frac{T-T_\infty}{T_{\mathrm{w}}-T_\infty},\ \phi_1(\eta)=\frac{C_1-C_{1\infty}}{C_{1\mathrm{w}}-C_{1\infty}},\ \phi_2(\eta)=\frac{C_2-C_{2\infty}}{C_{2\mathrm{w}}-C_{2\infty}} \tag{8}$$

are used in Eqs. (1)–(5), so that (1) is identically satisfied and the velocity components u and v are obtained as

$$u = U_0(x+b)^m f'(\eta),$$

$$v = -(\upsilon U_0)^{1/2}(x+b)^{(m-1)/2}\left[\left(\frac{m+1}{2}\right)f(\eta) + \left(\frac{m-1}{2}\right)\eta f'(\eta)\right], \tag{9}$$

where primes denote differentiation with respect to η. On substituting the similarity variables (8), Eqs. (2)–(5) are reduced to the following set of ordinary differential equations

$$f''' + \left(\frac{m+1}{2}\right) f\, f'' - m\, f'^2 + Ri\,[\theta + N_1\phi_1 + N_2\phi_2] - k_1 f' = 0\,, \tag{10}$$

$$\theta'' + \Pr\left(\frac{m+1}{2}\right) f\,\theta' - \Pr(2m-1) f'\theta = 0\,, \tag{11}$$

$$\phi_1^{''} + Sc_1\left(\frac{m+1}{2}\right) f\,\phi_1^{'} - Sc_1\,(2m-1) f'\phi_1 = 0\,, \tag{12}$$

$$\phi_2^{''} + Sc_2\left(\frac{m+1}{2}\right) f\,\phi_2^{'} - Sc_2\,(2m-1) f'\phi_2 = 0\,, \tag{13}$$

subject to the transformed boundary conditions

$$f'(\chi) = 1,\ f(\chi) = \chi\frac{1-m}{1+m},\ \theta(\chi) = \phi_1(\chi) = \phi_2(\chi) = 1 \text{ at } \eta = \chi\,,$$

$$f'(\eta_\infty) = 0,\ \theta(\eta_\infty) = \phi_1(\eta_\infty) = \phi_2(\eta_\infty) = 0 \text{ as } \eta \to \eta_\infty\,, \tag{14}$$

where η_∞ is the edge of the boundary layer and $\chi = a\,(U_0/\upsilon)^{1/2}$ is a parameter related to the thickness of the wall. Equations (10) to (13) with boundary conditions (14) are nonlinear differential equations with the domain $[\chi, \infty]$. In order to facilitate the computation and to transform the domain into $[0, \infty]$, define $h(\xi) = h\,(\eta - \chi) = f\,(\eta)$, $\Theta(\xi) = \Theta\,(\eta - \chi) = \theta\,(\eta)$, $\Phi_1(\xi) = \Phi_1\,(\eta - \chi) = \phi_1\,(\eta)$ and $\Phi_2(\xi) = \Phi_2\,(\eta - \chi) = \phi_2\,(\eta)$. The similarity equations become

$$h''' + \left(\frac{m+1}{2}\right) h\, h'' - m\, h'^2 + Ri\,[\Theta + N_1\Phi_1 + N_2\Phi_2] - k_1 h' = 0\,, \tag{15}$$

$$\Theta'' + \Pr\left(\frac{m+1}{2}\right) h\,\Theta' - \Pr(2m-1)\, h'\,\Theta = 0\,, \tag{16}$$

$$\Phi_1'' + Sc_1\left(\frac{m+1}{2}\right) h\,\Phi_1' - Sc_1\,(2m-1)\, h'\,\Phi_1 = 0\,, \tag{17}$$

$$\Phi_2'' + Sc_2 \left(\frac{m+1}{2}\right) h\, \Phi_2' - Sc_2\,(2m-1)\, h'\, \Phi_2 = 0\,, \tag{18}$$

with the boundary conditions

$$h(\xi) = \chi \left(\frac{1-m}{1+m}\right),\ h'(\xi) = 1,\ \Theta(\xi) = \Phi_1(\xi) = \Phi_2(\xi) = 1 \text{ at } \xi = 0,$$

$$h'(\xi) = 0,\ \Theta(\xi) = \Phi_1(\xi) = \Phi_2(\xi) = 0 \text{ as } \xi \to \infty\,, \tag{19}$$

where the primes denote differentiation with respect to ξ. Further, Richardson number Ri is the mixed convection parameter, N_1 and N_2 are the dimensionless parameters representing the ratio between the thermal and concentration buoyancy forces, which are defined as

$$\mathrm{Ri} = \frac{\mathrm{Gr}_x}{\mathrm{Re}_x^2},\ N_1 = \frac{\mathrm{Gr}_{1x}}{\mathrm{Gr}_x},\ N_2 = \frac{\mathrm{Gr}_{2x}}{\mathrm{Gr}_x}.$$

Here, $\mathrm{Gr}_x = g\beta(T_\mathrm{w} - T_\infty)(x+b)^3/\upsilon^2$ is the Grashof number referring to the wall temperature, $\mathrm{Gr}_{1x} = g\beta_1(C_{1\mathrm{w}} - C_{1\infty})(x+b)^3/\upsilon^2$ and $Gr_{2x} = g\beta_2(C_{2\mathrm{w}} - C_{2\infty})(x+b)^3/\upsilon^2$ are the Grashof numbers referring to the wall concentrations and $\mathrm{Re}_x = U_0(x+b)^{m+1}/\upsilon$ is the local Reynolds number. It should be mentioned that Ri>0 ($T_\mathrm{w} > T_\infty$) corresponds to assisting flow, Ri<0 ($T_\mathrm{w} < T_\infty$) corresponds to opposing flow and Ri=0 ($T_\mathrm{w} = T_\infty$) corresponds to forced convection flow case. Also, $N_1, N_2 > 0$ corresponds to assisting flows, $N_1, N_2 < 0$ corresponds to opposing flows, $N_1, N_2 = 0$ for no buoyancy effect due to mass diffusion, $N_1, N_2 = 1$ for the thermal and concentration forces of the same strength and $N_1, N_2 \to \infty$ for no buoyancy effect due to thermal diffusion. Also, $\mathrm{Sc}_1 = \upsilon/D_1$, $\mathrm{Sc}_2 = \upsilon/D_2$ are the Schmidt numbers and $k_1 = 1/\mathrm{Da}_x\mathrm{Re}_x$ is the permeability parameter where $\mathrm{Da}_x = k/(x+b)^2$ is the local Darcy number. The physical quantities of practical interest are local skin friction coefficient $C_{\mathrm{f}x}$, the local Nusselt number Nu_x and the local Sherwood numbers Sh_{x1} and Sh_{x2} for both salts, which are defined as

$$C_{\mathrm{f}x} = 2\mathrm{Re}_x^{-1/2} h''(0),\ \mathrm{Nu}_x = -\mathrm{Re}_x^{-1/2}\Theta'(0),$$

$$\mathrm{Sh}_{x1} = -\mathrm{Re}_x^{-1/2}\Phi_1'(0),\ \mathrm{Sh}_{x2} = -\mathrm{Re}_x^{-1/2}\Phi_2'(0). \tag{20}$$

3. Method of solution

The non-linear ordinary differential equations (15)–(18) under the boundary conditions (19) have been solved numerically by using the MATLAB program bvp4c. It is a finite difference method that implements the three-stage Lobatto IIIa formula, which is a collocation method with fourth-order accuracy [27]. In this approach, the differential equations are first reduced to a system of first order equations by intro-

ducing new variables. Mesh selection and error control are based on the residual of the continuous solution. In this study the relative error tolerance is set to 10^{-5}. A detailed description of this method is given by Shampine et al. [26].

4. Results and discussion

The computations have been carried out for various values of Pr ($0.7 \leq \mathrm{Pr} \leq 10.0$), Ri ($-0.1 \leq \mathrm{Ri} \leq 0.7$), $0.2 \leq \chi \leq 2.0$, N_1 ($-0.2 \leq N_1 \leq 3.0$), N_2 ($-0.2 \leq N_2 \leq 2.0$), m ($0.1 \leq m \leq 1.2$), Sc_1 ($0.22 \leq \mathrm{Sc}_1 \leq 2.57$), Sc_2 ($0.22 \leq \mathrm{Sc}_2 \leq 2.57$) and k_1 ($0.2 \leq k_1 \leq 1.2$). The edge of the boundary layer (η_∞) has been taken between 4.0 and 15.0 depending on the values of the parameters. In order to verify the correctness of the present numerical approach, the computed results are compared with those of Patil et al. [25].

The effects of Prandtl number (Pr) and mixed convection parameter Ri on velocity profile ($h'(\xi)$) are presented in Fig. 2.

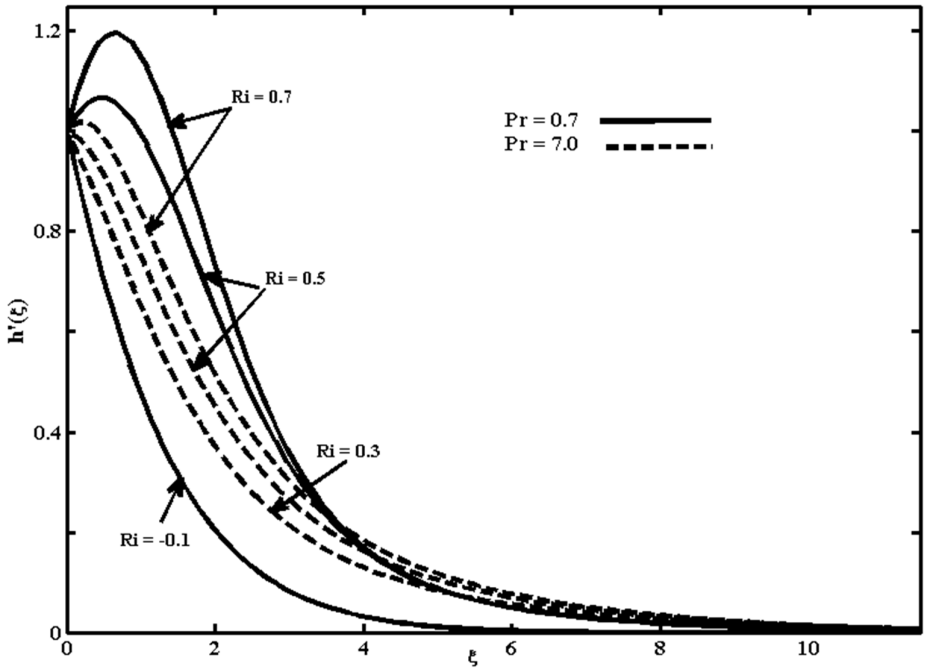

Fig. 2. Effect of Pr and Ri on velocity profile $h'(\xi)$ for $\chi = 0.2$, $N_1 = 0.2$, $N_2 = 0.3$, $\mathrm{Sc}_1 = 0.22$, $\mathrm{Sc}_2 = 0.94$, $m = 0.1$ and $k_1 = 0.1$

In the presence of assisting buoyancy effect ($\mathrm{Ri} > 0$), the buoyancy force shows a significant overshoot in the velocity profiles near the wall for lower Prandtl number fluid ($\mathrm{Pr} = 0.7$). The magnitude of the overshoot increases with the buoyancy parameter Ri, but decreases as the Prandtl number Pr increases. The physical reason is that the effect of buoyancy force is more in low Prandtl number fluid due to the

low viscosity of the fluid, which increases the velocity within the boundary layer as the assisting buoyancy force acts like a favorable pressure gradient. In particular, for Pr = 0.7 (air) the velocity profile exhibits approximately 15 % increase in overshoot within the boundary layer when Ri increases from 0.5 to 0.7. For higher Prandtl number fluids, the overshoot is not present because higher Prandtl number implies more viscous fluid which makes it less sensitive to buoyancy parameter Ri. Also, it is noticed that for opposing buoyancy effect (Ri < 0), the buoyancy force reduces the magnitude of velocity profiles significantly within the boundary layer. The effect of Ri is comparatively less in temperature and concentration profiles because Ri does not appear directly in the energy and concentration equations.

Figure 3 depicts the effect of buoyancy ratio parameters N_1 and N_2 (ratio of concentration buoyancy force to thermal buoyancy force parameter) on the velocity distribution.

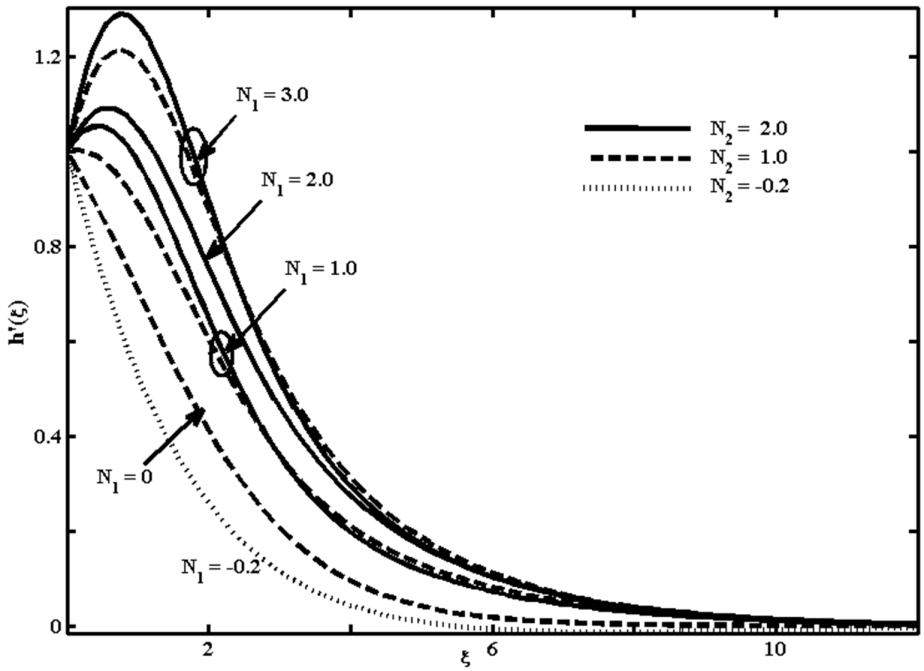

Fig. 3. Effect of N_1 and N_2 on velocity profile $h'(\xi)$ for Ri = 0.2, Pr = 0.7, $\mathrm{Sc}_1 = 0.22$, $\mathrm{Sc}_2 = 0.94$, $m = 0.1$, $\chi = 0.2$ and $k_1 = 0.1$

The positive values of N_1 and N_2 imply that the buoyancy forces of the concentration and the thermal buoyancy force act in the same direction. On the contrary, the negative values of N_1 and N_2 appear when thermal and concentration buoyancy forces act in opposite directions. In case of assisting flow (Ri > 0), the dimensionless velocity at the surface increases with increasing buoyancy ratios of both salts. It can be noted from Fig. 3 that as N_1 and N_2 increases, the velocity overshoot increases for buoyancy assisting flow (Ri = 0.2), near the wall. For example, for $N_2 = 2.0$, approximately, 9 % increase in overshoot is noticed as N_1 increases from

2.0 to 3.0. Similarly, for $N_1 = 3.0$, approximately, 4 % increase in overshoot is noticed as N_2 increases from 1.0 to 2.0. The physical reason is that the buoyancy forces act like pressure gradient which accelerates the fluid within the boundary layer. For $N_1 = -0.2$ and $N_2 = -0.2$, a significant reduction in the magnitude of the velocity profile is noticed this is because N_1 and N_2 acts in the direction opposite to the thermal buoyancy force and thereby decelerates the fluid flow. The effect of N_1 and N_2 on the temperature and concentration profiles is very less because the buoyancy ratio parameters are explicitly present only in the momentum equation. The effect of wall thickness parameter (χ) on velocity ($h'(\xi)$), temperature ($\Theta(\xi)$) and concentration ($\Phi_1(\xi), \Phi_2(\xi)$) profiles is presented in Fig. 4.

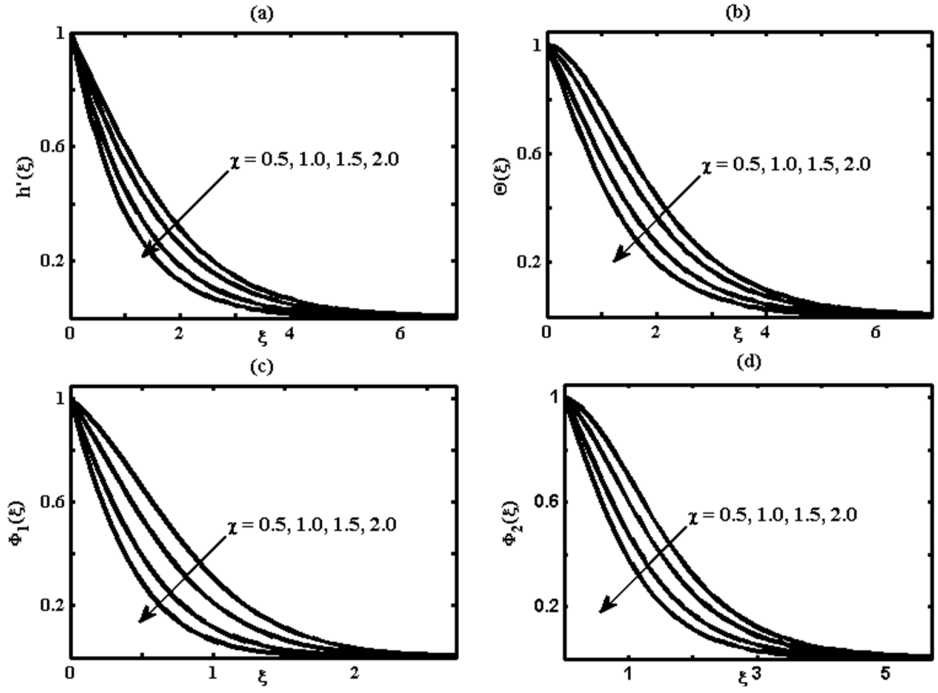

Fig. 4. Effect of $\xi = 0.2$ temperature $\Theta(\xi)$ and concentrations $\varphi_1(\xi), \varphi_2(\xi)$ profiles when $\mathrm{Pr} = 0.7$, $\mathrm{Sc}_1 = 2.57$, $\mathrm{Sc}_2 = 0.94$, $m = 0.1$, $N_1 = 0.2$, $N_2 = 0.3$, $k_1 = 0.2$ and $\mathrm{Ri} = 0.3$

It is noted that the velocity gets decelerated for increasing values of wall thickness parameter (Fig. 4(a)). Increase in wall thickness parameter of the stretching sheet acts as a factor which retards the fluid flow. Also, increase in χ reduces the thermal boundary layer thickness (Fig. 4(b)). It happens due to less heat transfer form thicker regions to the flow than the thinner regions. Similarly, increase in wall thickness parameter decreases the concentration boundary layer thickness ($\Phi_1(\xi)$, $\Phi_2(\xi)$) because of less mass transfer from the fluid near the thicker regions of the wall to the outer flow.

Figure 5 elucidates the effect of velocity power index m and permeability parameter k_1 on velocity profile $h'(\xi)$.

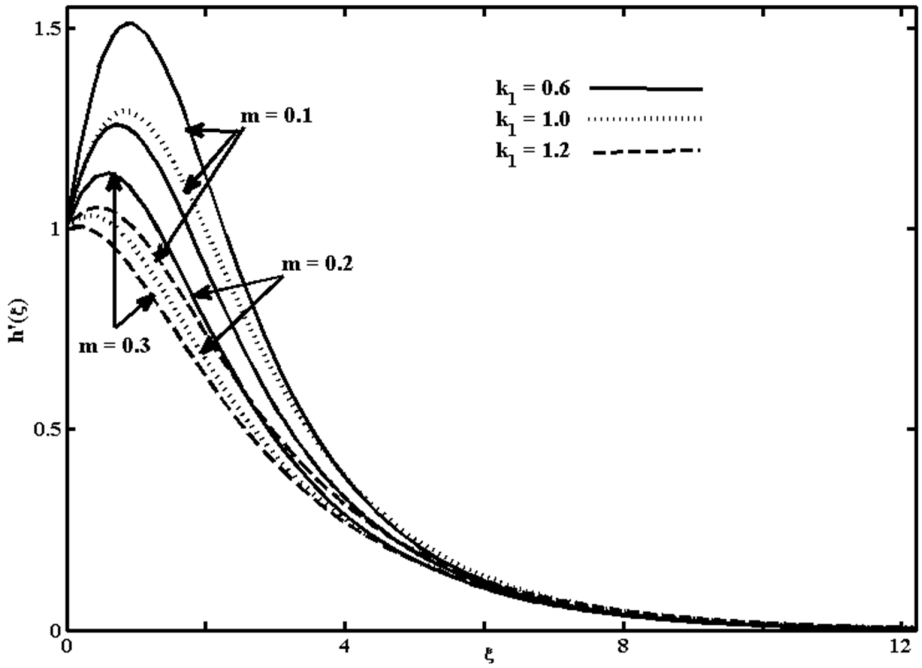

Fig. 5. Effect of k_1 and m on velocity profile $h'(\xi)$ for Pr $= 0.7$, $\mathrm{Sc}_1 = 0.22$, $\mathrm{Sc}_2 = 0.94$, $N_1 = 2.0$, $N_2 = 1.0$, $\chi = 0.2$ and Ri $= 0.5$

It is observed that as the velocity power index increases from $m = 0.1$ to $m = 0.3$ there is a considerable decrease in velocity near the wall. This is due to the fact that increase in index parameter m leads to fluid deceleration. Furthermore, increase in the permeability parameter k_1 produces a resistive force and hence leads to deceleration of fluid near the wall. For example, 50 % overshoot is observed for $m = 0.1$ and $k_1 = 0.6$, whereas, only 30 % overshoot is observed when $m = 0.1$ and $k_1 = 1.0$. It can be noted from Fig. 5 that significant overshoot is observed for lower value of the velocity power index parameter m and permeability parameter k_1. Further, it is observed that increase in index parameter (m) decreases the thermal boundary layer thickness (Fig. 6). This is because as m increases fluid particle decelerates, reducing heat transfer from the wall. Also, increase in permeability parameter causes decrease in thermal boundary layer thickness. The impact of permeability parameter k_1 and wall thickness parameter χ on shear stress distribution $h''(\xi)$ and temperature gradient variation $(\Theta'(\xi))$ are presented in Fig. 7. It is noted that the shear stress distribution near the wall gets decreased due to relaxed flow. As the sheet slender away from the slot, the flow gains its velocity and increases the shear stress distribution. Increase in index parameter decelerates the flow near the wall whereas reverse trend is observed away from the wall (Fig. 7(a)). Also, it is evident through Fig. 7(b) that increase in wall thickness parameter reduces the temperature gradient near the wall, this happens due to less heat transfer from the thicker wall than from the thinner wall.

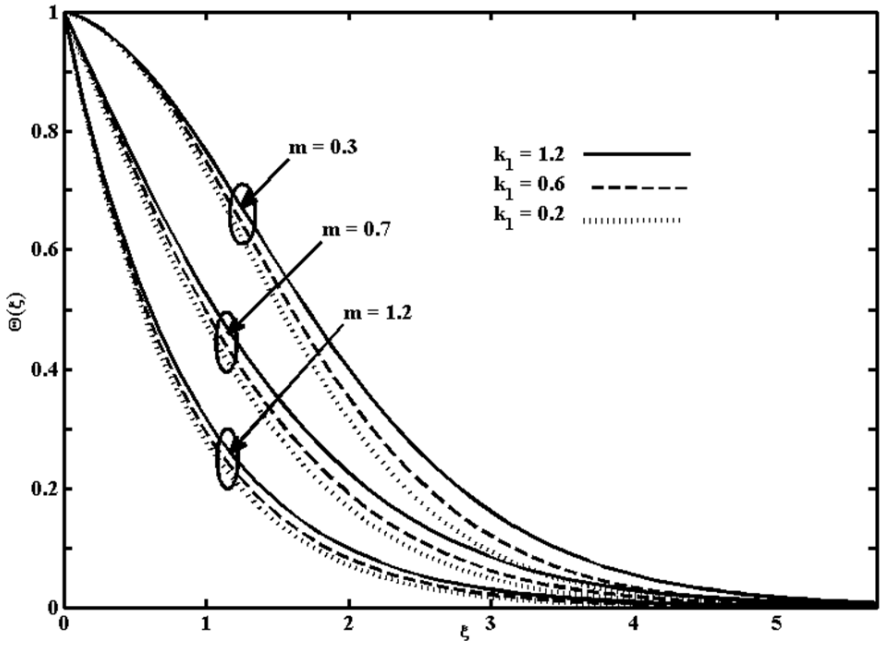

Fig. 6. Effect of m and k_1 on temperature profile $\Theta(\xi)$ for $\mathrm{Pr} = 0.7$, $\mathrm{Sc}_1 = 0.22$, $\mathrm{Sc}_2 = 0.94$, $N_1 = 2.0$, $N_2 = 1.0$, $\chi = 0.2$ and $\mathrm{Ri} = 0.5$

The effect of velocity power index m on the heat transfer at the wall $-\Theta'(0)$ for various values of Pr and Ri is presented in Fig. 8. Increase in Prandtl number causes a significant increase in heat transfer coefficient thereby decreasing the thermal boundary layer thickness as the higher Prandtl number has a lower thermal conductivity. It is interesting to observe in Fig. 8 that as Prandtl number increases from 1.0 to 3.0, the heat transfer coefficient $-\Theta'(0)$ increases approximately by 71 % for $\mathrm{Ri} = 0.5$, $m = 1.0$, $k_1 = 0.4$, $\mathrm{Sc}_1 = 0.22$, $\mathrm{Sc}_2 = 0.94$, $N_1 = 1.0$, $N_2 = 2.0$ and $\chi = 0.5$. It can be observed that the effect of mixed convection parameter Ri has less influence on the heat transfer coefficient $-\Theta'(0)$. Further, increase in mixed convection parameter and the index parameter causes increase in heat transfer coefficient. The influence of permeability parameter k_1 on local skin friction coefficient $h''(0)$ for different values of mixed convection parameter Ri and buoyancy ratio parameters $N_1,\ N_2$) is depicted in Fig. 9. It is observed that as the mixed convection parameter increases the local skin friction coefficient decreases. About 30 % decrease in $h''(0)$ is noticed as Ri increases from 0.5 to 0.7 when $k_1 = 0.2$, $N_1 = 2.0$ and $N_2 = 2.0$. Also, increase in the buoyancy ratio parameter causes increase in local skin friction coefficient. The effects of buoyancy ratios N_1 and N_2 on the dimensionless concentrations $\Phi_1(\xi)$ and $\Phi_2(\xi)$ for different values of Schmidt numbers Sc_1 and Sc_2 can be observed in Fig. 10. The dimensionless concentration decreases with increasing buoyancy ratios. Further, it can be noted that the concentration boundary layer thickness decreases with increase in Schmidt number. In each case, the dimensionless

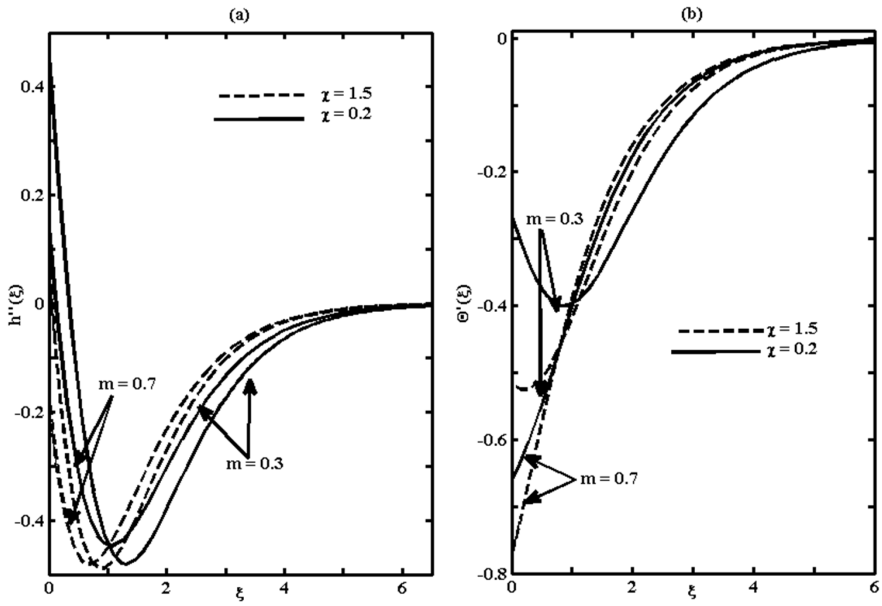

Fig. 7. Effect of m and χ on shear stress distribution $h''(\xi)$ and temperature gradient distribution $\Theta(\xi)$ for Pr $= 0.7$, $\mathrm{Sc}_1 = 0.94$, $\mathrm{Sc}_2 = 2.57$, $N_1 = 2.0$, $N_2 = 1.0$, $k_1 = 0.2$ and Ri $= 0.5$

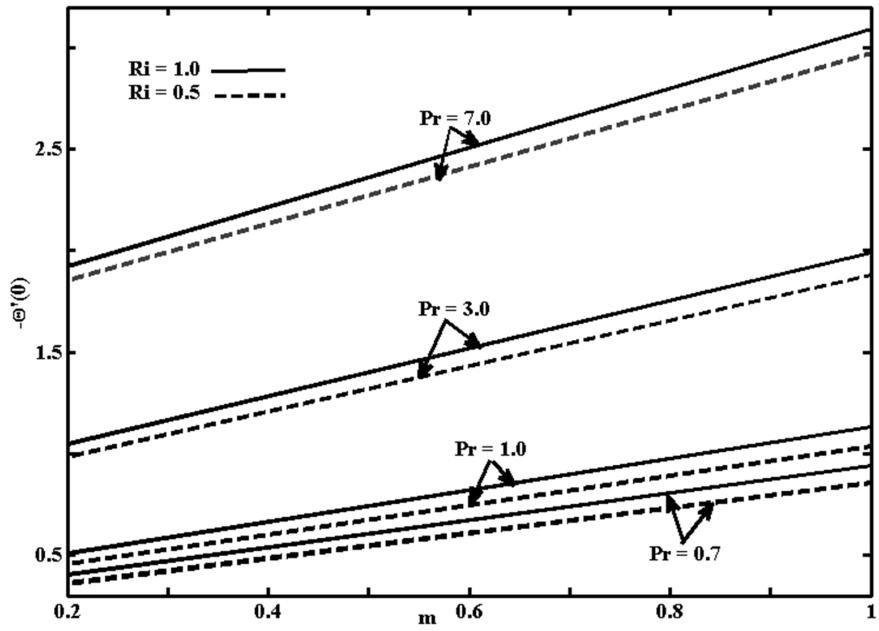

Fig. 8. Variation of $-\Theta'(0)$ with m for various values of Ri and Pr when $\mathrm{Sc}_1 = 0.22$, $\mathrm{Sc}_2 = 0.94$, $N_1 = 1.0$, $N_2 = 2.0$, $\chi = 0.5$ and $k_1 = 0.4$

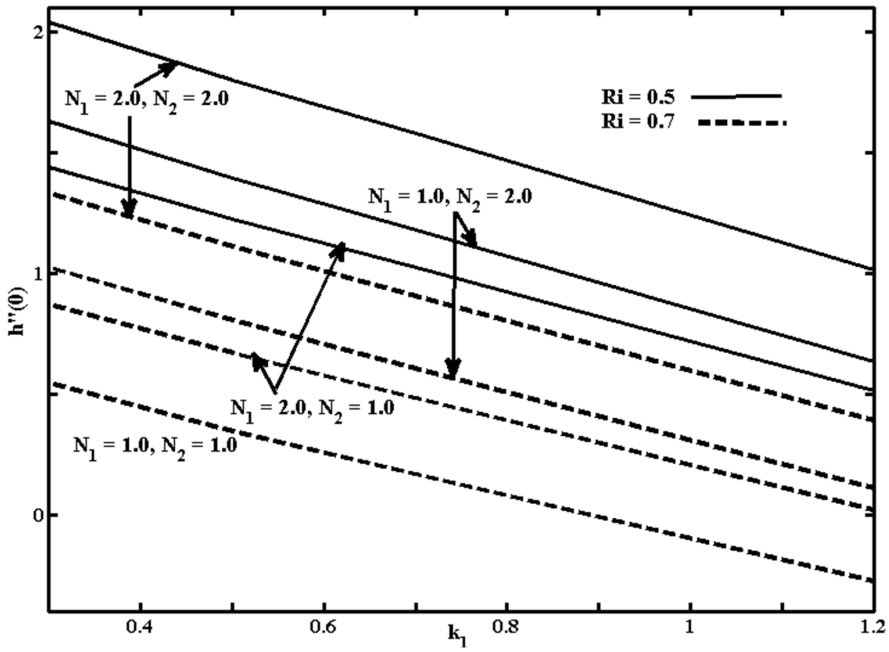

Fig. 9. Variation of $h''(0)$ with k_1 for various values of Ri, N_1 and N_2 when Pr = 0.7, $\mathrm{Sc}_1 = 0.94$, $\mathrm{Sc}_2 = 0.22$, $m = 0.2$ and $\chi = 0.5$

wall concentration drops quickly in a very short distance to zero for large Schmidt numbers. Physically, the increase of Schmidt number means a decrease of molecular diffusivity and the concentration profiles show significant variation for different values of Schmidt numbers Sc_1 and Sc_2.

5. Conclusion

Steady triple diffusive convection flow over a stretching sheet of variable thickness has been studied numerically. Conclusions of the study are as follows

1. The buoyancy assisting force produces significant velocity overshoot near the wall for low Prandtl number fluid but for high Prandtl number fluid, the velocity overshoot is not present.

2. Approximately 5% increase in velocity overshoot is observed with the increase in the value of buoyancy ratios N_1 and N_2 for buoyancy assisting flow (Ri = 0.2).

3. Increase in the velocity power index m causes decrease in velocity and temperature near the wall.

4. Approximately 20 % reduction in velocity overshoot is observed as the permeability parameter k_1 increases from 0.6 to 1.0. Also, increase in permeability

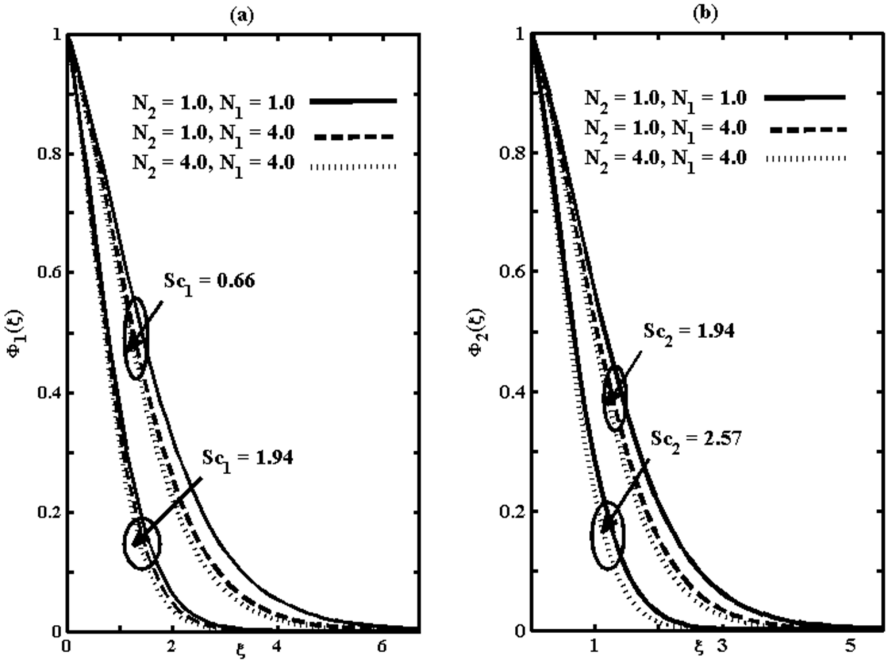

Fig. 10. Effect of Sc_1, Sc_2, N_1 and N_2 on concentration profiles $\Phi_1(\xi), \Phi_2(\xi)$ when $\mathrm{Pr} = 0.7$, $k_1 = 0.2$, $\chi = 0.2$, $m = 0.3$ and $\mathrm{Ri} = 0.5$

decreases thermal boundary layer thickness.

5. Increase in wall thickness parameter (χ) decreases the boundary layer thickness of velocity, temperature and concentration.

6. It is noted that as Prandtl number increases from 1.0 to 3.0, heat transfer coefficient increases approximately by 71 %.

References

[1] A. V. Kuznetsov, D. A. Nield: *The effects of combined horizontal and vertical heterogeneity on the onset of convection in a porous medium: Double diffusive case.* Transport in Porous Media *72* (2008), No. 2, 157–170.

[2] M. S. Malashetty, M. S. Swamy, R. Heera: *Double diffusive convection in a porous layer using a thermal non-equilibrium model.* International Journal of Thermal Sciences *47* (2008), No. 9, 1131–1147.

[3] M. S. Malashetty, R. Heera: *The onset of double diffusive convection in a sparsely packed porous layer using a thermal non-equilibrium model.* Acta Mechanica *204* (2009), No. 1, 1–20.

[4] S. V. Subhashini, Nancy Samuel, I. Pop: *Numerical investigation of dual solutions for double diffusive convection from a permeable horizontal flat plate.* International Journal of Heat and Mass Transfer *55* (2012), Nos. 19–20, 4981–4986.

[5] S. V. Subhashini, R. Sumathi, I. Pop: *Dual solutions in a double-diffusive convection near stagnation point region over a stretching vertical surface.* International Journal of Heat and Mass Transfer *55* (2012), Nos. 9–10, 2524–2530.

[6] D. A. Nield, A. V. Kuznetsov: *The onset of double-diffusive convection in a vertical cylinder with vertical throughflow.* Journal of Heat Transfer *135* (2013), No. 3, p. 034502.

[7] N. A. Khan, F. Sultan: *On the double diffusive convection flow of Eyring-Powell fluid due to cone through a porous medium with Soret and Dufour effects.* AIP Advances (2015), No. 5, p. 057140.

[8] A. V. Kuznetsov, D. A. Nield: *Double-diffusive natural convective boundary-layer flow of a nanofluid past a vertical plate.* International Journal of Thermal Sciences *50* (2011), No. 5, 712–717.

[9] M. S. Malashetty, A. A. Hill, M. Swamy: *Double diffusive convection in a viscoelastic fluid-saturated porous layer using a thermal non-equilibrium model.* Acta Mechanica *223* (2012), No. 5, 967–983.

[10] D. Poulikakos: *The effect of a third diffusing component on the onset of convection in a horizontal porous layer.* AIP Physics of Fluids (1985), No. 28, p. 3172–3174.

[11] S. Rionero: *Triple diffusive convection in porous media.* Acta Mechanica *224* (2013), No. 2, 447–458.

[12] Z. H. Khan, W. A. Khan, I. Pop: *Triple diffusive free convection along a horizontal plate in porous media saturated by a nanofluid with convective boundary condition.* International Journal of Heat and Mass Transfer *66* (2013), No. 2, 603–612.

[13] W. A. Khan, J. R. Culham, Z. H. Khan, I. Pop: *Triple diffusion along a horizontal plate in a porous medium with convective boundary condition.* International Journal of Thermal Sciences *86* (2014), 60–67.

[14] G. C. Rana, Ramesh Chand, Veena Sharma, Abhilasha Sharda: *On the onset of triple-diffusive convection in a layer of nanofluid.* Journal of Computational Applied Mechanics *47* (2016), No. 1, 67–77.

[15] M. Ghalambaz, F. Moattar, M. A. Sheremet, I. Pop: *Triple-diffusive natural convection in a square porous cavity.* Transport in Porous Media *111* (2016), No. 1, 59-79.

[16] M. Ghalambaz, F. Moattar, A. Karbassi, M. A. Shereme, I. Pop: *Triple-diffusive mixed convection in a porous open cavity.* Transport in Porous Media *116* (2017), No. 2, 473–491.

[17] N. Acharya, Kalidas Das, P. K. Kundu: *Ramification of variable thickness on MHD TiO_2 and Ag nanofluid flow over a slendering stretching sheet using NDM.* European Physical Journal Plus *131* (2016), No. 9, p. 303.

[18] L. L. Lee: *Boundary layer over a thin needle.* AIP Physics of Fluids *10* (1967), No. 4, 820–828.

[19] T. Fang, J. Zhang, Y. Zhong: *Boundary layer flow over a stretching sheet with variable thickness.* Applied Mathematics and Computation *218* (2012), No. 13, 7241–7252.

[20] S. V. Subhashini, R. Sumathi, I. Pop: *Dual solutions in a thermal diffusive flow over a stretching sheet with variable thickness.* International Communications in Heat and Mass Transfer *48* (2013), 61–66.

[21] M. M. Khader, A. M. Megahed: *Boundary layer flow due to a stretching sheet with a variable thickness and slip velocity.* Journal of Applied Mechanics and Technical Physics *56* (2015), No. 2, 241–247.

[22] S. P. A. Devi, M. Prakash: *Thermal radiation effects on hydromagnetic flow over a slendering stretching sheet.* Journal of the Brazilian Society of Mechanical Sciences and Engineering *38* (2016), No. 2, 423–431.

[23] S. P. A. Devi, M. Prakash: *Slip flow effects over hydromagnetic forced convective flow over a slendering setching sheet.* Journal of Applied Fluid Mechanics *9* (2016), No. 2, 683–692.

[24] G. K. Ramesh, B. C. Prasannakumara, B. J. Gireesha, M. M. Rashidi: *Casson fluid flow near the stagnation point over a stretching sheet with variable thickness and radiation*. Journal of Applied Fluid Mechanics *9* (2016), No. 3, 1115–1122.

[25] P. M. Patil, S. Roy, R. J. Moitsheki, E. Momoniat: *Double diffusive flows over a stretching sheet of variable thickness with or without surface mass transfer*. Heat Transfer–Asian Research *46* (2017), No. 8, 1087–1103.

[26] L. F. Shampine, I. Gladwell, S. Thompson: *Solving ODEs with Matlab*. Cambridge University Press New York, USA (2003).

[27] Y. Y. Lok, I. Pop: *Stretching or shrinking sheet problem for unsteady separated stagnation-point flow*. Meccanica *49* (2014), No. 6, 1479–1492.

Received July 27, 2017

Acta Technica *63* No. 3/2018, 423–432

Modeling the dynamic behavior of machine tool considering joint dynamic characteristics[1]

Liao Yongyi[2,3,4], Liao Baiyu[2]

Abstract. A method of establishing the dynamic analytic model of machine tool considering joint dynamic characteristics is developed and analyzed. The method is based on study of joint dynamic characteristics to obtain dynamic values of combined surface incorporating joint dynamic data, and build up the dynamic model using design drawing or actual structure. Firstly, according to the structure characteristics of the machine tool and the vibration displacement for each component in exciting test, the motion coordinates of each component are selected, and the machine tool is simplified reasonably. Secondly, analyzing and studying the specific joint, according to the way and condition of the joint, the equivalent dynamic parameters of each joint are calculated by applying the general joint surface dynamic data. Calculation methods of dynamic values for some typical joints in machine tool structures are analyzed and presented. Based on the second type of Lagrange equations, the dynamic model can be finally obtained. As a practical example, a tool-milling machine is represented by a dynamic model with 19 degrees of freedom, the computations of dynamic characteristics and response are completed and the results agree with that of exciting test. The dynamic model can well simulate the actual dynamic characteristics, and thus proving the method effective and applicable.

Key words. Machine tool, modeling, dynamic model, dynamic behavior, joints, modal flexibility.

1. Introduction

To analyze the structural dynamics of machine tool and realize dynamically optimum design, it is necessary to establish the dynamic analytic model that simulates

[1]The authors wish to express gratitude to the Test chamber of Kunming milling machine plant for providing design drawings and giving much help in performing experiments, and acknowledge the support from National Natural Science Foundation of China grant program (51465021).

[2]Adult Education College, Kunming University of Science and Technology, Kunming 650051, China

[3]Key Laboratory of Vibration and Noise under Ministry of Education of Yunnan Province, Kunming 650500, China

[4]Corresponding author; e-mail: yongyiliao@163.com

the machine tool structures. For complex machine tool structure system, it is still difficult to obtain the dynamic model from its physical coordinates. Now the methods of building up the dynamic analytic model can be summarized as following three kinds:

The first method, by applying machine tool drawings or a real structure, simplifies machine tool to a certain extent in accordance with different ways, and builds up a lumped-parameter model, a beam distributed model or a finite element model correspondingly [1–3]. Because of the complexity of machine tool structures, especially joints, this kind of modeling now is rather limited [4], and the modeling precision is below the dynamically optimum design requirements.

In the second method, based on the theory of experimental modal analysis, using experimental data of modal test for machine tool, the modal model is established [5–7]. First, from modal test data the modal parameters are obtained. Then, according to the evaluated coupling distributions of mass, stiffness and damping of machine tool, initial geometrical state of the model can be given, and the place and direction of motion coordinates are determined. The dynamic structural parameters are finally identified in accordance with transformation of modal coordinates and physical coordinates. This kind of modeling was limited by the modal numbers excited, so that the dynamic model with only a few degrees of freedom can be obtained.

The third method is substructure method [8], which divides the total structure into many parts; each part is called a substructure. In the light of the structural characteristics of each substructure, a lumped-parameter model, a beam distributed model or a finite element model can be modeled correspondingly. The dynamic characteristics of the substructures are determined by an analysis or experiment. Then, by applying modal synthesis method or mechanical impedance method, the dynamic model of complete structure is obtained by synthesis of all substructures according to joint conditions [9–10].

With developing the experimental modal analysis technology, although it is easy to determine the modal mass, modal stiffness and modal damping ratio for each modal of machine tool, as viewed from design improvement and optimum design, the obtained modal model cannot be related directly to the specific design improvement and optimum design, only some approximately concussions can be obtained. On the contrary, the dynamic model in physical coordinates is convenient and direct from this viewpoint.

Based on the first method as stated above, a method of modeling the dynamic analytic model of a machine tool considering joint dynamic characteristics and using design drawing is developed. Above all, in accordance with the characteristics of structure and displacement in exciting test for each component of the machine tool, the motion coordinates for each component are decided, and the machine tool is simplified reasonably. Upon that, making a study of the specific joint, the equivalent parameters of each joint can be calculated by applying the general joint surface dynamic data. Based on the second type of Lagrange equations, the dynamics equations of machine tool structure can be finally developed.

2. The dynamic analytic model for milling machine

This tool-milling machine is a middle-sized product with broad versatility. In accordance with the structural features and distributions of this machine, it is divided up eight parts: (1) Bed (including bottom base), (2) Horizontal spindle body (including main motor with stand and cross beam, (3) Vertical milling head support, (4) Vertical milling head, (5) Vertical cutter arbor, (6) Horizontal table, (7) Vertical table, (8) Compound slide.

Compound slide fits bed with rectangular slideway. Between the horizontal spindle body and bed as well as vertical table and compound slide are all fitted each other with dovetail slideway.

According to the characteristics of displacement in exciting test, the milling machine is represented by a dynamic model involving lumped and distributed masses with 19 degrees of freedom. By applying the second type of Lagrange equations, the differential equations of machine tool are obtained as follows

$$\frac{\mathrm{d}}{\mathrm{d}t}\left[\frac{\partial T}{\partial \dot{q}_j}\right] - \frac{\partial T}{\partial q_j} + \frac{\partial U}{\partial q_j} + \frac{\partial D}{\partial \dot{q}_j} = Q_j, \quad j = 1, 2, \cdots, 19\,, \tag{1}$$

where T is the total kinetic energy of the system, q_j is the generalized coordinate of the system, U is the total potential energy of the system, D is the Rayleigh energy dissipation function, and Q_j is the exciting force.

According to the dynamic model, the total kinetic energy T, the total potential energy U and Rayleigh energy function D of the structure are calculated, and after substituting for T, D and U in equation (1), then we obtain

$$\boldsymbol{M}_{19\times 19}\ddot{\boldsymbol{q}}_{19\times 1} + \boldsymbol{C}_{19\times 19}\dot{\boldsymbol{q}}_{19\times 1} + \boldsymbol{K}_{19\times 19}\boldsymbol{q}_{19\times 1} = \boldsymbol{F}(t)_{19\times 1}\,. \tag{2}$$

Here, $\boldsymbol{M}$ denotes the mass matrix, $\boldsymbol{C}$ is the damping matrix and $\boldsymbol{K}$ is the stiffness matrix, while $\boldsymbol{q}$ is the column matrix of generalized coordinates and $\boldsymbol{F}(t)$ is the column matrix of exciting forces.

Masses of each component involved in the model are found by weighing actual structures. By the principle of compound pendulum, moments of inertia are determined by measuring the oscillation frequency in gravity field, while neglecting the effect of friction moment on the edge of the blade bearing.

The key to modeling is to determine the physical parameters of joints in the model accurate comparatively. Based on analysis of characteristics of joints, by applying the general joint surface dynamic data [11] $k_i(P_n)$ and $c_i(P_n)$, $i = 1, 2$, the equivalent spring stiffness and viscous damping coefficients of each joint in the model are calculated in this paper. Data $k_i(P_n)$ and $c_i(P_n)$, $i = 1, 2$, denote equivalent spring stiffness and damping coefficients per unit area, which are obtained by experiment and computer simulation. They are functions of the contact pressure. Subscripts $i = 1, 2$ represent the shear direction and normal direction, respectively. It is confirmed that the joint dynamics data $k_i(P_n)$ and $c_i(P_n)$, $i = 1, 2$, which depend on the mean contact pressure, can be applied satisfactorily to general joints which have the same contact surface properties but differ in shape and contact area.

In the joints of machine tool structure, with fixed and sliding of joint ways, as well as with surface contact, rectangular slideway and dovetail slideway of joint patterns, and with different state of forces, therefore, to calculate the parameters of these joints, it is necessary to further analyze these joints by using general joint surface dynamic data.

For a contact surface, the forms of dynamic force supported on contact surface are determined by modal shapes. The contact surface can be supported by six different forms of dynamic forces, which are generalized forces over six coordinates as shown in Fig. 1. These dynamic forces are normal force F_y along axis y and the shearing forces F_x, F_z along axes x and z, bending moment $M_{\theta x}$, $M_{\theta z}$ around axes x and z, and shear bending moment $M_{\theta y}$ around axis y. The contact surface may be supported all of them or any of these forces. Integral over area replaced by the point G, the equivalent spring stiffness and damping coefficients at point G are obtained as indicated in the following equations:

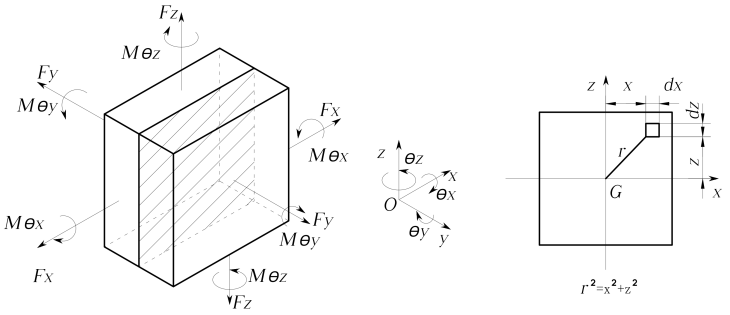

Fig. 1. Sketch of the forces on contact surface

$$K_x = \int\int k_1(P_n)\,\mathrm{d}x\,\mathrm{d}z = K_z, \quad K_y = \int\int k_2(P_n)\,\mathrm{d}x\,\mathrm{d}z\,,$$

$$K_{\theta y} = \int\int (y^2+z^2)k_1(P_n)\,\mathrm{d}x\,\mathrm{d}z, \quad K_{\theta x} = \int\int z^2 k_2(P_n)\,\mathrm{d}x\,\mathrm{d}z\,,$$

$$K_{\theta z} = \int\int y^2 k_2(P_n)\,\mathrm{d}x\,\mathrm{d}z \tag{3}$$

and

$$C_x = \int\int c_1(P_n)\,\mathrm{d}x\,\mathrm{d}z = c_z, \quad C_y = \int\int c_2(P_n)\,\mathrm{d}x\,\mathrm{d}z\,,$$

$$C_{\theta y} = \int\int (y^2+z^2)c_1(P_n)\,\mathrm{d}x\,\mathrm{d}z, \quad C_{\theta x} = \int\int z^2 c_2(P_n)\,\mathrm{d}x\,\mathrm{d}z\,,$$

$$C_{\theta z} = \int\int y^2 c_2(P_n)\,\mathrm{d}x\,\mathrm{d}z\,. \tag{4}$$

Based on the equation (3), for dovetail slideway joint shown in Fig. 2, the equivalent spring stiffness at point G can be derived by calculating the spring stiffness

around point G as follows:

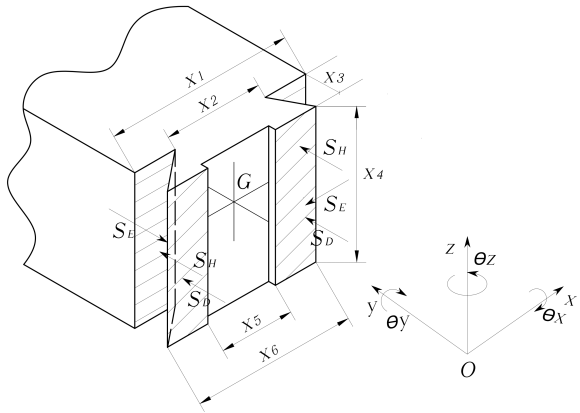

Fig. 2. Dovetail slideway joint

$$K_x = 2(K_{Dx} + K_{Hx} + K_{Ex}\cos\theta + K_{Ey}\sin\theta)\,,$$

$$K_y = 2(K_{Dy} + K_{Hy} + K_{Ex}\sin\theta + K_{Ey}\cos\theta), \quad K_z = 2(K_{Dz} + K_{Hz} + K_{Ez})\,,$$

$$K_{\theta x} = 2[K_{D\theta x} + K_{H\theta x} + K_{E\theta x}\cos\theta + K_{E\theta y}\sin\theta + \frac{x_3^2}{4}(K_{Hz} + K_{Dz})]\,,$$

$$K_{\theta y} = 2[K_{D\theta y} + K_{H\theta y} + K_{E\theta x}\sin\theta + K_{E\theta y}\cos\theta + \frac{(x_1+x_2)^2}{16}K_{Hz} +$$

$$+ \frac{(x_5+x_6)^2}{16}K_{Dz} + \frac{(x_6+x_2)^2}{16}K_{Ez}]\,,$$

$$K_{\theta z} = 2[K_{D\theta z} + K_{H\theta z} + \frac{(x_1+x_2)^2}{16}K_{Hy} + \frac{(x_5+x_6)^2}{16}K_{Dy} +$$

$$+ K_{E\theta z} + \frac{(x_6+x_2)^2}{16}(K_{Ex}\sin\theta + K_{Ey}\cos\theta) + \frac{x_3^2}{4}(K_{Hx} + K_{Dx})]\,. \tag{5}$$

For rectangular slideway joint shown in Fig. 3, the equivalent spring stiffness at point G can be derived as follows:

$$K_x = 2(K_{Dx} + K_{Hx} + K_{Ey} + K_{Ty}), \quad K_y = 2(K_{Dy} + K_{Hy} + K_{Ex} + K_{Tx}\,,$$

$$K_z = 2(K_{Dz} + K_{Hz} + K_{Ez} + K_{Tz})\,,$$

$$K_{\theta x} = 2[K_{D\theta x} + K_{H\theta x} + K_{E\theta y} + K_{T\theta y} + \frac{x_3^2}{4}(K_{Hz} + K_{Dz})]\,,$$

$$K_{\theta y} = 2[K_{D\theta y} + K_{H\theta y} + K_{E\theta x} + K_{T\theta x} + \frac{(x_1+x_5)^2}{16}K_{Hz} +$$

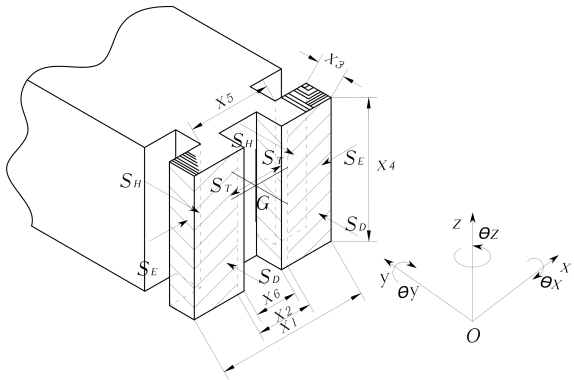

Fig. 3. Rectangular slideway joint

$$+\frac{(x_1+x_2)^2}{16}K_{Dz}+\frac{x_6^2}{4}K_{Tz}+\frac{x_1^2}{4}K_{Ez}],$$

$$K_{\theta z}=2[K_{D\theta z}+K_{H\theta z}+K_{E\theta z}+K_{T\theta z}+\frac{(x_1+x_5)^2}{16}K_{Hy}+\frac{(x_1+x_2)^2}{16}K_{Dy}+$$

$$+\frac{x_3^2}{4}(K_{Hx}+K_{Dx})+\frac{x_1^2}{4}K_{Ex}+\frac{x_6^2}{4}K_{Tx}]. \tag{6}$$

Similarly, the equations for calculating the equivalent damping coefficients are derived. In the first subscripts D, H, E, T correspond to the joint surface S_D, S_H, S_E and S_T, while the second subscripts $x\,, y\,, z\,, \theta_x\,, \theta_y\,, \theta_z$ correspond to the directions of six coordinates respectively.

By applying the above equations, the equivalent spring stiffness coefficients in the model are calculated, and the results for equivalent spring stiffness of joints are displayed in Table 1.

3. Dynamic characteristics analysis and computation

After the motion equation of the structural system is obtained, the characteristic equation can be written as follows:

$$\boldsymbol{K}\boldsymbol{\phi}_i=\omega_i^2\boldsymbol{M}\boldsymbol{\phi}_i \tag{7}$$

where $\boldsymbol{\phi}_i$ is the r-order eigenvector. The natural frequencies ω_{n1}, ω_{n2}, $\cdots$, ω_{n19} and vibration vectors $\boldsymbol{A}^1$, $\boldsymbol{A}^2$, $\cdots$, $\boldsymbol{A}^{19}$ of the structural system can be obtained, respectively, by solving the above equations.

For vertical milling, the direction of the main cutting force in the $x-y$ plane is simplified along the x-axis direction. The actual cutting conditions are simulated approximately by the relative exciting shown in Fig. 4, between cutter and workpiece, a pair of equal and opposite forces $-F_{\mathrm{e}}\mathrm{e}^{\mathrm{i}\omega t}$ at point O_5 of the vertical cutter arbor and $F_{\mathrm{e}}\mathrm{e}^{\mathrm{i}\omega t}$ at point O_6 of the horizontal table are applied along horizontal direction.

Thus, the exciting force column matrix can be expressed as

Table 1. The values of equivalent stiffness of each joint

Joint	Stiffness (N/m, N m/rad)	
Bed and horizontal spindle body	$K_x^{①}$	7.642×10^8
	$K_{\theta x}^{①}$	3.629×10^7
	$K_{\theta z}^{①}$	5.473×10^7
Bed and compound slide	$K_x^{⑧}$	3.829×10^8
Vertical milling head and vertical milling head support	$K_{\theta x}^{③}$	7.142×10^6
Vertical milling head and vertical cutter arbor	$K_x^{④}$	2.741×10^7
Horizontal table and vertical table	$K_x^{⑥}$	2.512×10^9
	$K_z^{⑥}$	2.512×10^9
Vertical table and compound slide	$K_x^{⑦}$	7.218×10^5
	$K_{\theta x}^{⑦}$	4.538×10^7
	$K_{\theta z}^{⑦}$	4.341×10^7

Note: In the table the unit of line stiffness is N/m, while the unit of angular stiffness is N m/rad.

$$\boldsymbol{F}(t)_{19\times 1} = (000000000,\ -F_{e10}\mathrm{e}^{\mathrm{i}\omega t},\ 000,\ F_{e14}\mathrm{e}^{\mathrm{i}\omega t},\ 00000)^{\mathrm{T}} = \boldsymbol{F}\mathrm{e}^{\mathrm{i}\omega t}. \tag{8}$$

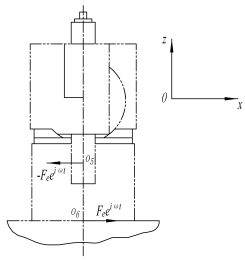

Fig. 4. Diagram of exciting force

In accordance with theory of modal analysis, the cutter-workpiece relative displacement in the normal direction of machined surface under relative of exciting can be derived as

$$X_{\mathrm{c}} = \sum_{r=1}^{19} \frac{\left(A_{14}^r - A_{10}^r\right)^2 F_{\mathrm{e}}}{K_r \left[1 - \left(\frac{\omega}{\omega_{nr}}\right)^2 + \mathrm{i}\cdot 2\xi_r \left(\frac{\omega}{\omega_{nr}}\right)\right]} \tag{9}$$

where, A_{14}^r and A_{10}^r are the r-order modal vectors corresponding to the generalized

coordinates q_{14} and q_{10}, K_r is the r-order modal stiffness, ξ_r denotes the r-order modal damping ratio and ω, ω_{nr} are exciting frequency and the r-order natural frequency, respectively. Thus, the compliance of cutter-work at cutting point can be written as

$$W_{\mathrm{c}} = \frac{X_{\mathrm{c}}}{F_{\mathrm{e}}} = \sum_{r=1}^{19} \frac{\left(A_{14}^r - A_{10}^r\right)^2}{K_r \left[1 - \left(\frac{\omega}{\omega_{nr}}\right)^2 + \mathrm{i}\, 2\xi_r \left(\frac{\omega}{\omega_{nr}}\right)\right]} . \tag{10}$$

If $\omega = 0$, the relative static compliance $(f_{\mathrm{ce}})_{\mathrm{s}}$ and modal flexibility $(f_{\mathrm{ce}})_r$ of machine tool structure in cutting force direction (e) and in normal direction (c) of machined surface at cutting point are found to be

$$(f_{\mathrm{ce}})_{\mathrm{s}} = \left(\frac{X_{\mathrm{c}}}{F_{\mathrm{e}}}\right)_{\omega=0} = \sum_{r=1}^{19} \frac{\left(A_{14}^r - A_{10}^r\right)^2}{K_r} = \sum_{r=1}^{19} (f_{\mathrm{ce}})_r \ , \tag{11}$$

where

$$\sum_{r=1}^{19} \frac{(f_{\mathrm{ce}})_r}{(f_{\mathrm{ce}})_{\mathrm{s}}} = \frac{(f_{\mathrm{ce}})_1}{(f_{\mathrm{ce}})_{\mathrm{s}}} + \frac{(f_{\mathrm{ce}})_2}{(f_{\mathrm{ce}})_{\mathrm{s}}} + \cdots + \frac{(f_{\mathrm{ce}})_{19}}{(f_{\mathrm{ce}})_{\mathrm{s}}} = 1.0 \, . \tag{12}$$

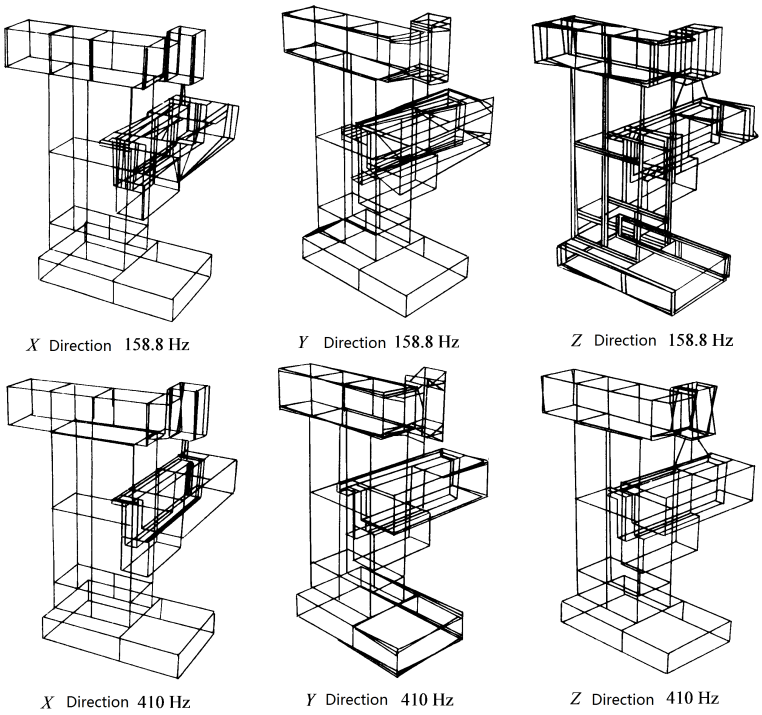

Fig. 5. Vibration modal shape of machine tool

The modal damping ratio ξ_r used in the calculations is obtained by analyzing

the machine tool relative pseudo-random exciting test data processing by analyzer 7T17S. Fig. 5 shows the vibration modal shape of the main modes of 158.8 Hz and 410 Hz. Fig. 6 compares the computed frequency response at cutting point with that of exciting test. The dotted lines indicate the computed results, while the solid line is the relative harmonic exciting results. Table 2 compares the modal frequencies in relative pseudo-random exciting with computed natural frequencies. The correspondence between the calculated results and the measured results indicates that the dynamic analytic model established is in line with the experimental situation, and the model can simulate the dynamic characteristics of the actual structure well.

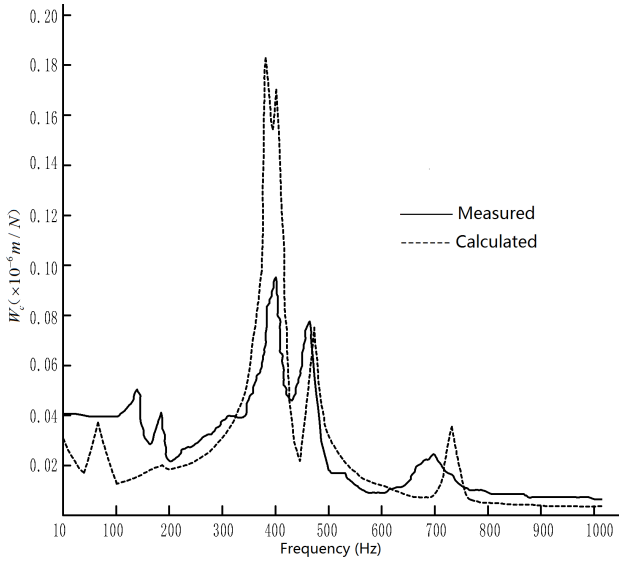

Fig. 6. Computed and measured results of the relative compliance

Table 2. Comparison between natural frequencies and modal frequencies

Modal order	Computed results	Experimental value		Modal order	Computed results	Experimental value	
	Natural frequency (Hz)	Modal frequency (Hz)	Modal damping ratio		Natural frequency (Hz)	Modal frequency (Hz)	Modal damping ratio
1	17.741	——	——	8	390.744	——	——
2	39.342	——	——	9	403.966	410.069	0.0183
3	65.275	——	——	10	472.266	468.000	——
4	162.248	158.794	0.0236	11	534.494	545.092	0.0183
5	195.181	197.642	0.0379	12	585.166	596.314	0.0147
6	273.391	——	——	13	645.908	625.045	0.0120
7	319.625	315.159	0.0317	14	735.153	738.802	0.0118

4. Conclusion

1. The method to build the dynamic model of machine tool structure considering joint dynamic characteristics is feasible and applicable to engineering.

2. The dynamic analytic model established simulates the dynamic characteristics of the actual structure well, the computed results agree with that of exciting test.

3. Lagrange equations based on principle of energy are used to establish the equation of motion of machine tool structure, so it can be easily calculated energy distribution of each component in the system, and the energy ratio of a part in the system can be computed consequently. Based on this, dynamic optimum design and structural improvement could be carried out, which will be discussed in another paper.

References

[1] M. Yoshimura, T. Hosh: *Computer approach to dynamically optimum design of machine tool structures.* Proceedings of the Twelfth International Machine Tool Design and Research Conference, London: Macmillan Publishers Limited (1972), 439–446.

[2] T. Hosh, M. Yoshimura: *Initial applications of dynamic structural analysis to computer-aided design of machine tools.* Proceedings of the Fourteenth International Machine Tool Design and Research Conference, London: Macmillan Publishers Limited (1974), 559–566.

[3] M. Yoshimura: *Study on optimum design of machine structures with respect to dynamic characteristics: Approach to optimum design of machine tool structures with respect to regenerative chatter.* Bulletin of JSME *20* (1977), No. 145, 811–818.

[4] R. P. H. Faassen, N. van de Wouw, J. A. J. Oosterling, H. Nijmeijer: *Prediction of regenerative chatter by modelling and analysis of high-speed milling.* International Journal of Machine Tools and Manufacture *43* (2003), No. 14, 1437–1446.

[5] Z. Q. Cui, R. F. Yang: *Parametric modeling and modal analysis for the complex mechanical structure.* Journal of Mechanical Engineering *44* (2008), No. 2, 234–237.

[6] S. Vafaei, H. Rahnejat, R. Aini: *Vibration monitoring of high speed spindles using spectral analysis techniques.* International Journal of Machine Tools and Manufacture *42* (2002), No. 11, 1223–1234.

[7] W. J. Wu, Q. Liu: *Extended transfer matrix method for dynamic modeling of machine tools.* Journal of Mechanical Engineering *46* (2010), No. 21, 69–75.

[8] M. Yoshimura: *Computer aided design of machine structures with respect to static and dynamic characteristics by synthesis of dynamic rigidity program system: Study for analysis of structural dynamics of machine tools.* Journal of the Japan Society of Precision Engineering *41* (1975), No. 490, 1060–1065.

[9] C. Y. Liu, F. Tan, L. P. Wang, Z. Y. Cai: *Research on optimization of column structure design for dynamic performance of machine tool.* Journal of Mechanical Engineering *52* (2016), No. 3, 161–168.

[10] L. Li, A. J. Cai, L. G. Cai, T. Guo, X. Ruan: *Identification method for dynamic properties of bolted joints.* Journal of Mechanical Engineering *49* (2013), No. 7, 168–175.

[11] M. Yoshimura: *Computed-aided design improvement of machine tool structure incorporating joint dynamics data.* Annals of the CIRP *28* (1979), No. 1, 241–246.

Received May 5, 2018

Acta Technica *63* No. 3/2018, 433–446

Monitoring thermal state of induction motors through the winding direct temperature control during the start

Oleksandr G. Sereda[1], Victoriia Lytvynenko[2], Iryna Varshamova[3]

Abstract. The necessity of the direct winding thermal control of induction motors is proved. The thermal mode control of motors operating with the intermittent duty is done by analyzing extreme values of instantaneous power consumed by an electric motor at the initial moment after its start. Theoretical justification of the possibility to obtain information on parameters of an electric loop in the transient condition of current disturbance changing, especially, when reading induction motor temperature through controlling their winding active resistance change. An algorithm of micro-processing device functioning is developed. The device is to protect induction motors that operate in the intermittent duty mode against winding overheating.

Key words. Induction motor, protective micro-processing device.

1. Introduction

Electric supply systems of subsurface mining machines are built according to the principle of transferring the electric power through cables from explosion proof switch gears of a central subsurface power station to mini-substations that convert the voltage of 6 (10) kV into 380, 660/1140 V with further its distribution through controlling/protecting devices to electric motors of mining machines. In this case it is allowed to connect no more than three technologically linked portable substations/transformers of the same capacity to one switch-gear provided that high sensibility of the current protection devices is arranged. It significantly complicates the electric supply mine subsurface system [1]. One of the ways to enhance explosion proof mini-substations is increasing their functionality of protection at the low voltage side. It requires to engineer the structures that contain a protective device

[1]NTU "KhPI"; 2, Kyrpychova str., Educational and Research Institute of Power Engineering, Electronics and Electromechanics, Department of Electrical Apparatus, 61002, Kharkiv, Ukraine
[2]E-mail addresse: : {o.g.sereda, vikalitv21082, varshamova.i.s}@gmail.com

of supply connections/controlling the motors of mine machines [2].

In the changeable and continuous operation mode some actuators and mechanisms create loads that vary within a wide range, for instance, crushing machines. Periodic overloading of a motor is accompanied by either underloading or idling [3]. Some short time current increasing doesn't lead to dangerous temperature growing. However, if over-currents repeat, the heightened temperature influence on motor insulation accumulates quickly. The process of heating up a motor in the mode of varying loading is different from the process of heating it up with the constant/slightly varying loading [4, 5]. If loads vary, a motor is constantly in a transient process. Flowing of the transient thermal processes with changeable loads is a very difficult phenomenon and barely computable. Therefore, it is not possible to measure motor winding temperature by a current flowing in it. Due to the fact that separate parts of a motor heat up differently, parts exchange the heat between themselves inside the motor. Once the motor is switched off, stator winding temperature can grow due to the heat transferred from the rotor [6–8]. Therefore, an electric current value does not reflect the degree of insulation heating up. It should be noted that in some modes the rotor will heat up quicker, whereas it will cool down slower than the stator. The difficulty of heat exchange processes complicates the control of motor heating. The intermittent mode is the most disadvantageous in the sense of protection. Periodic switching on/off creates short time overloading of the motor. In this case an overloading value should be limited by a set value of winding heating up. The protection device, which monitors winding temperature, should receive a corresponding signal. Since in transient modes the current and temperature can be mismatching each other, the protection, whose action is based on current measurement, cannot function properly.

Periodic overheating of the winding shortens the insulation operation life. The operation life of motor and insulation depends on the over-temperature value. Overheating by each 8–10 °C above the allowed limit shortens the insulation operation life twice as much (the eight-degree rule of Montziger) [9–11]. According to the last researches a long period of motor operation with 5 % over-current shortens its service life 10 times as much [12–14]. Therefore, the winding temperature control is the important means to provide a long service life of motors.

2. Analysis of researches and related papers

Known methods of induction motor protection against over-currents, whose protective time-current I_{L} response is formed through using so called "integral" set point Q_{L} [15]:

$$Q_{\mathrm{L}} = I_{\mathrm{ph}}^2 t_{\mathrm{L}} \,, \tag{1}$$

where I_{ph} is the rms value (active) of phase current and t_{L} denotes the time of protection tripping in over-current conditions.

In over-current conditions, the integral set point provides inverse dependence $t_{\mathrm{L}} = f\left(I_{\mathrm{ph}}^2\right)$ of time t_{L} on a phased current squared value I_{ph}^2. If thermal loading on a protected motor exceeds a given value Q_{L} and its protection trips, an operation

algorithm of the protection device stipulates a time delay for repetitive switching on. This value t_r should be adopted, if a motor cools down to a set [16] temperature. It allows to have a non-direct control of the motor temperature mode, which justifies using the integral protection response with the set point Q_L. In the same time, the indicated features of the protection response influence negatively on the operation efficiency of the equipment operating with intermittent duty. The motor integral set point, which is used in the equipment, facilitates operation of the equipment, but decreases its efficiency. Therefore, leading electric companies exclude the integral set point from the over-current protection devices of motors designed to operate in the intermittent mode and substitute them with time set points. A time set point decreases the overload time and allows to switch on the motor quicker.

TeSys LR97D and LT47 relays of "Schneider electric" Company [17] are examples of motor protective devices against over-currents. These relays were designed to protect motors that operated in intermittent-short time mode with increased load torque, when the rotor was blocked, phase missed, rotor was blocked by growing brake torque, mechanism switched on/off often with high inertia and probability to jam in the constant mode: conveyors, crushers, mixers, driers, presses, elevators, fans, pumps, compressors, and lathes. Quick detection of overload in comparison with heat protection devices based on the integral set point is one of advantageous protection functions of LR97D and LT47 relays.

Some deficiencies should also be noted in spite of advantages of the motor protection method through using inertial integral set point. The thermal load level control is the main deficiency. Motors without thermistor protection are often exposed to such loading. In case of an aggressive mode (often occurring starts) without decreasing the process equipment loading, motor winding heating up can exceed an allowed limit. Let's remember that in the intermittent and short time mode the most overheated part is not the entire motor, but only its winding and its insulation, in particular.

There are some technical solutions of indirect control over motor winding temperature.

E16DU-E1250DU electronic relays of "ABB" Company [18] can model thermal response of motor behavior. In case of often switching on/off the most important is not nominal current, but higher start current of a motor, and its start frequency (number of switching on and off). Significant heating of a motor occurs at each start. In this case temperature can exceed an allowed limit. In order to avoid motor breakage, it should be stopped. Overload relay tripping occurs, if temperature exceeds a maximally allowed limit. The relay tripping algorithm defines allowed duration of motor starting, if due to long starting/frequent starting a current average effective value reaches its nominal level. Thermistor relays of CM-MSE, CM-MSS, CM-MSN types of "ABB" Company control a temperature mode of motors equipped with a temperature sensor with a positive resistance coefficient (thermistor). Thermistors inbuilt in the motor windings measure a degree of motor heating; it allows to control various operation conditions: overheating due to insufficient cooling, heavy start, often switching on/off, operation with one phase, braking, phase asymmetry. If only one thermistor is heated above a set limit, an output relay switches off a motor from

mains.

Moeller ZEV [19] system and Siemens Sirius 3RB20/21 overloading electronic relays [20] fit for the heaviest conditions of motor starting. The triggering threshold is settable and allows to reliably protect a motor with acceleration time of up to 40 sec. The current increase is monitored by an inbuilt current transformer and processed by an electric unit, which generates an impulse for auxiliary switches. Ground short-circuit is detected by an external current transformer. The possibility of combining thermistor sensors into one system allows to provide the motor complete protection. Moeller EMT6 and Siemens Sirius 3RB22/23 protection thermistor relays possess necessary features to interact with thermistors during long starting or stopping of a motor.

Usage limitation of calculated technical solutions of motor thermal protection is the common disadvantage. Overload relays with thermistor temperature control can be used only for protection of motors, whose windings contain thermistors. More versatile is the direct control over motor winding temperature increase in case of overloading. The direct control measures a degree of active resistance R_{m} of a motor winding itself instead of current measurement [21, 22] of thermistors that should be inbuilt in a winding. Therefore, a motor winding is used as a temperature sensor.

According to the technical solution [23], resistance R_{m} is measured to find motor winding temperature by a special device, which should be connected to the winding before it is powered. In order to switch on/off the measurement unit Rm before the motor is started, an intermediate relay is used. Its contacts connect the unit to the motor supply circuit. Such method of resistance measurement Rm, requiring usage of auxiliary equipment with the intermediate relay, increases overall dimensions and cost of the protection devices, and decreases the reliability of its operation. Besides, when applying the described measurement method Rm to protect motors, operating in the intermittent and short time mode, the process equipment operation responsiveness worsens. Before the next starting of a motor, it is necessary to carry out all the described above connection operations, measurement and connection of the measurement unit Rm.

Taking into account the said above, it is reasonable to develop such temperature control technical solution Rm, which measures temperature without additional units and only through analyzing active and reactive powers that are consumed by a motor during the start. The motor winding temperature control through analyzing extreme values of instantaneous power allows to simplify the functional set of the protection devices and in so doing to decrease financial expenses for its manufacturing, because there will be no need for additional measuring/controlling units, and to provide operation responsiveness of motors/process equipment that operate in intermittent-and-short time mode, because measuring the motor winding temperature will be done quickly in 10 msec.

3. Goal formulation

The theoretical justification, development and implementation of a micro-processing unit function algorithm to protect motors against over-currents with the direct tem-

perature control in winding during the start; finding its active resistance value and calculation of winding temperature at each start.

4. Research materials

The control of a motor winding temperature mode should be done in the transient mode of electric loop disturbance with obtaining discrete values of phase currents i_{ja}, i_{jb}, i_{jc} ($i_{\mathrm{j(a,b,c)}}$) and voltages u_{ja}, u_{jb}, u_{jc} ($u_{\mathrm{j(a,b,c)}}$). The possibility of such control is based on the analysis of the quasi-instantaneous value alterations of total active $p_{\Sigma}(t)$ and reactive $q_{\Sigma}(t)$ powers of the three-phase circuit during the first period of disturbance, namely on the extreme value ratio of $p_{\max}p_{\Sigma}(t)$ and $q_{\max}q_{\Sigma}(t)$ in the transient mode of start current changing. The dependency of the phase current discrete $i_{\mathrm{j(a,b,c)}}$ value product sum on the phase voltage discrete $u_{\mathrm{j(a,b,c)}}$ values can be analyzed.

The behavior during quasi-instantaneous values p_{ja}, p_{jb}, p_{jc} ($p_{\mathrm{j(a,b,c)}}$) of active and q_{ja}, q_{jb}, q_{jc} ($q_{\mathrm{j(a,b,c)}}$) reactive powers in the motor start transient mode and at different values of the electromagnetic time constant τ of an electric loop was examined. The time dependencies of quasi-instantaneous active $p_{\Sigma}(t)$ and reactive $q_{\Sigma}(t)$ powers of all three phases were obtained through mathematical modeling of the motor start process:

$$p_{\Sigma}(t) = p_{\mathrm{a}}(t) + p_{\mathrm{b}}(t) + p_{\mathrm{c}}(t) \,, \tag{2}$$

$$q_{\Sigma}(t) = q_{\mathrm{a}}(t) + q_{\mathrm{b}}(t) + q_{\mathrm{c}}(t) \,, \tag{3}$$

where $p_{\mathrm{a}}(t) = i_{\mathrm{a}}(t)u_{\mathrm{a}}(t)$, $p_{\mathrm{b}}(t) = i_{\mathrm{b}}(t)u_{\mathrm{b}}(t)$, $p_{\mathrm{c}}(t) = i_{\mathrm{c}}(t)u_{\mathrm{c}}(t)$ are the quasi-instantaneous values of the active powers consumed in a motor, in phases a, b, c, respectively; $q_{\mathrm{a}}(t) = i_{\mathrm{a}}(t)u_{\mathrm{a}}(t-T/4)$, $q_{\mathrm{b}}(t) = i_{\mathrm{b}}(t)u_{\mathrm{b}}(t-T/4)$, $q_{\mathrm{c}}(t) = i_{\mathrm{c}}(t)u_{\mathrm{c}}(t-T/4)$ are the quasi-instantaneous values of reactive powers consumed in a motor in phases a, b, c, respectively and T is the period of mains voltage changing.

The well-known analytic expressions of current behavior in time of a symmetrical three phase system in the transient mode are

$$i_{\mathrm{a}}(t) = \sqrt{2}I_{\mathrm{ph}}\left[\sin(\omega t + \psi - \varphi + 2\pi/3) - \sin(\psi - \varphi + 2\pi/3)\cdot \mathrm{e}^{-t/\tau}\right] , \tag{4}$$

$$i_{\mathrm{b}}(t) = \sqrt{2}I_{\mathrm{ph}}\left[\sin(\omega t + \psi - \varphi) - \sin(\psi - \varphi)\cdot \mathrm{e}^{-t/\tau}\right] , \tag{5}$$

$$i_{\mathrm{c}}(t) = \sqrt{2}I_{\mathrm{ph}}\left[\sin(\omega t + \psi - \varphi - 2\pi/3) - \sin(\psi - \varphi - 2\pi/3)\cdot \mathrm{e}^{-t/\tau}\right] , \tag{6}$$

where I_{ph} is the rms (active) value of the phase current periodic component, $\varphi = arctg(\omega L/R)$ denotes the displacement angle at which the phase current periodic component lags behind the phase EMF, L and R are induction and active resistance of the phase, $\tau = L/R = \sin\varphi/(\omega\cos\varphi)$ stands for the time constant of the electric

loop, $\omega = 2\pi f$ is the mains angular frequency, f represents the mains operation frequency, and ψ is the moment of current disturbance.

Equations of phase EMF behavior in time read

$$u_{\mathrm{a}}(t) = \sqrt{2}U_{\mathrm{ph}} \sin\left(\omega t + \psi + 2\pi/3\right) , \tag{7}$$

$$u_{\mathrm{b}}(t) = \sqrt{2}U_{\mathrm{ph}} \sin\left(\omega t + \psi\right) , \tag{8}$$

$$u_{\mathrm{c}}(t) = \sqrt{2}U_{\mathrm{ph}} \sin\left(\omega t + \psi - 2\pi/3\right) , \tag{9}$$

where U_{ph} is rms (active) value of phase EMF and ψ represents the EMF initial angle of phase b (disturbance beginning moment).

As it can be seen from equations (7)–(9), phase voltages (unlike currents) do not have any aperiodic component.

The temporal dependencies of total quasi-instantaneous power of the three phase circuit consumed by the electric motor during its start were analyzed using mathematical modeling. We substitute equations (4)–(6) for phase currents and (7)–(9) for phase voltages in formula (2) and obtain the expression

$$\begin{aligned} p_{\Sigma}(t) &= 2I_{\mathrm{ph}}U_{\mathrm{ph}} \times \\ &\times \Big\{ \Big[\sin\left(\omega t + \psi - \varphi + \tfrac{2\pi}{3}\right) - \sin\left(\psi - \varphi + \tfrac{2\pi}{3}\right) \cdot e^{-\frac{t}{\tau}}\Big] \times \sin\left(\omega t + \psi + \tfrac{2}{3}\pi\right) + \\ &+ \Big[\sin\left(\omega t + \psi - \varphi\right) - \sin\left(\psi - \varphi\right) \cdot e^{-\frac{t}{\tau}}\Big] \times \sin\left(\omega t + \psi\right) + \\ &+ \Big[\sin\left(\omega t + \psi - \varphi - \tfrac{2\pi}{3}\right) - \sin\left(\psi - \varphi - \tfrac{2\pi}{3}\right) \cdot e^{-\frac{t}{\tau}}\Big] \times \sin\left(\omega t + \psi - \tfrac{2}{3}\pi\right) \Big\} , \end{aligned} \tag{10}$$

which, after some calculation gives

$$p_{\Sigma}(t) = 3I_{\mathrm{ph}}U_{\mathrm{ph}} \left[\cos\varphi - \cos(\omega t + \varphi) \cdot \mathrm{e}^{-\frac{t}{\tau}}\right] . \tag{11}$$

The values of $p_{\mathrm{a}}(t)$, $p_{\mathrm{b}}(t)$ and $p_{\mathrm{c}}(t)$ in the steady mode change in time by the sinusoidal law, so the character of variation in time of the phase power $p_{\mathrm{ph}}(t)$ in the transient mode of the electric drive start, namely, the extreme values are determined by the moment of occurrence of inrush current I_{st} and the value of the electromagnetic time constant of the circuit τ $(\cos\varphi)$. Moment ψ of the occurrence of the current I_{st} is a random value, so by the nature of the change of the dependence $p_{\mathrm{ph}}(t)$ it is impossible to extract reliable information about the value of τ. As the results of mathematical modeling shown, accurate information on the value of τ can be extracted from the analysis of the time dependence (11) of power p_{Σ} (see Fig. 1).

The temporal behavior of quasi-instantaneous values q_{ja}, q_{jb}, q_{jc} $(q_{\mathrm{j(a,b,c)}})$ of powers in the transient mode of the electric motor start at different values of the electromagnetic time constant τ of the electric circuit was investigated. The tempo-

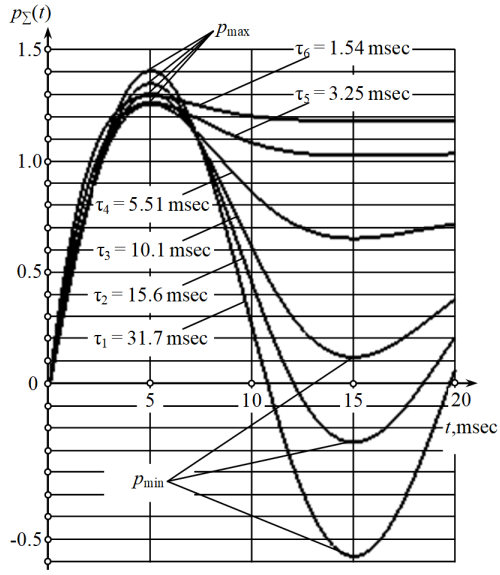

Fig. 1. Time change of quasi-instantaneous active power consumed by an electric motor in the start transient mode

ral dependence of total quasi-instantaneous power $q_\Sigma(t)$ for the three phase circuit consumed by the electric motor in the start mode was obtained using mathematical modeling of the motor start process.

We substitute equations (4)–(6) for phase currents and (7)–(9) for phase voltages in formula (3) and obtain the expression

$$q_\Sigma(t) = -2I_{\text{ph}}U_{\text{ph}}\times$$

$$\times\left\{\left[\sin\left(\omega t+\psi-\varphi+\tfrac{2\pi}{3}\right)-\sin\left(\psi-\varphi+\tfrac{2\pi}{3}\right)\cdot e^{-\frac{t}{\tau}}\right]\times\cos\left(\omega t+\psi+\tfrac{2}{3}\pi\right)+\right.$$

$$+\left[\sin\left(\omega t+\psi-\varphi\right)-\sin\left(\psi-\varphi\right)\cdot e^{-\frac{t}{\tau}}\right]\times\cos\left(\omega t+\psi\right)+$$

$$\left.+\left[\sin\left(\omega t+\psi-\varphi-\tfrac{2\pi}{3}\right)-\sin\left(\psi-\varphi-\tfrac{2\pi}{3}\right)\cdot e^{-\frac{t}{\tau}}\right]\times\cos\left(\omega t+\psi-\tfrac{2}{3}\pi\right)\right\}. \tag{12}$$

After some calculations we get

$$q_\Sigma(t) = -3I_{\text{ph}}U_{\text{ph}}\left[\sin\varphi-\sin(\omega t+\varphi)\cdot\mathrm{e}^{-\frac{t}{\tau}}\right] \tag{13}$$

The analysis of expression (13) shows that the temporal behavior character of variation of the dependence $q_\Sigma(t)$ in the transient mode of the current change as well temporal behavior character of variation of the dependence $p_\Sigma(t)$ (11) does not depend on the moment ψ of the disturbance current occurrence. It means that the

character of functions $p_\Sigma(t)$ and $q_\Sigma(t)$, in particular their extreme values $p_{\max}$ and $q_{\max}$ only depend on the time constant of the electric circuit τ.

Figure 2 shows dependencies $q_\Sigma(t)$ for different cases of the time constant τ (and, respectively, $\cos\varphi$) built under condition that active values of currents and voltages at determining quasi-instantaneous values q_j and, respectively, at calculation of values q_Σ, are assumed to be equal to 1.

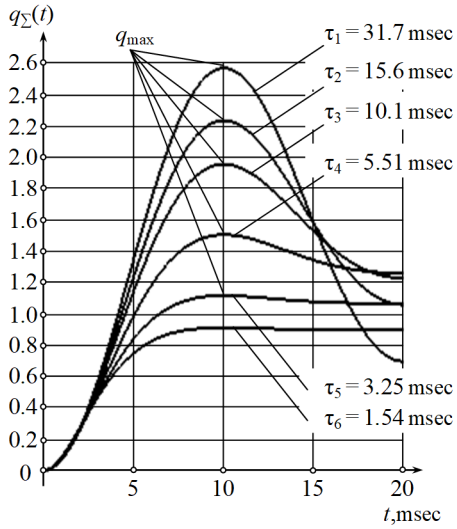

Fig. 2. Time change of quasi-instantaneous reactive power consumed by an electric motor in the start transient mode

The dependencies in Figs. 1, 2 illustrate the necessary features of functions $p_\Sigma(t)$ and $q_\Sigma(t)$ in the transient mode. It is obvious, that values $p_{\max}$ and $q_{\max}$ the more differ from each other, the less is time constant τ. Therefore, by the relationship of $p_{\max}$ and $q_{\max}$ in first 10 msec upon the motor start it is possible to find the value of τ, resistance R_m and motor winding temperature.

The analysis of time changing of values p_Σ and q_Σ is valid only for the first period $T_1 = 20$ msec of start current. Such a small time interval is necessary for excluding the influence of motor rotation beginning on the time constant τ of its winding. It is known, that values of power factor $\cos\varphi$ of the motor winding vary from 0.2–0.3 at the starting moment to 0.9 upon reaching the idling mode state. The faster is motor rotation, the more is a value of the time constant. Therefore, in order to exclude the influence on τ of motor winding heating, it is necessary to find the value of τ as soon as possible and prior to the moment, when motor starts to rotate.

Using the difference $q_j - p_j$ of reactive and active powers, especially for $q_{\max} - p_{\max}$, a criterion of finding a change of τ of the motor wining during its heating up in a general case, when values of current and voltage do not equal 1, is not possible. The difference $q_{\max} - p_{\max}$ will depend on the value of motor starting current. In order to make the τ change criterion as not depending on current and voltage, it should be expressed in relative units.

Let us find an operation range of the value τ, when the winding resistance heats up. Let us assume that $\cos\varphi = 0.2$, when the motor is started at ambient temperature. Such $\cos\varphi$ corresponds to time constant of $\tau_{25} = 15.6$ msec ($f = 50$ Hz). The temperature of $T_{\mathrm{B}} = 155\,^{\circ}\mathrm{C}$ [5] is an allowed temperature of V-class insulation winding. It maintains the standard operation life of the insulation. Copper wire resistance, if heated by $\Delta T = 130\,^{\circ}\mathrm{C}$, will grow 1.55 times as much. Therefore, time constant τ of the winding heated up to $T_{\mathrm{B}} = 155\,^{\circ}\mathrm{C}$ will decrease down to $\tau_{155} = 0.645\tau_{25} = 10.06$ msec. Thus, the range of $\tau = (10 - 16)$ msec is operational. Either the relationship $K = p_{\max}/q_{\max}$ or $K = q_{\max}/p_{\max}$ is not convenient to use due to low sensitivity of their behavior $\tau = f(K)$ in the operational range of the change of τ.

The more significant coefficient of an irregularity degree of extreme values $p_{\max}$ and $q_{\max}$, if τ varies, is the relationship of active W_{P} and reactive W_{Q} powers:

$$K_{\mathrm{W}} = \frac{W_{\mathrm{Q}} - W_{\mathrm{P}}}{W_{\mathrm{P}}}\,, \tag{14}$$

where

$$W_{\mathrm{P}} = \sum_{0}^{t=T_1/2} p_{\Sigma \mathrm{j}} \Delta t = \sum_{0}^{t=T_1/2} \left(u_{\mathrm{ja}} i_{\mathrm{ja}} + u_{\mathrm{jb}} i_{\mathrm{jb}} + u_{\mathrm{jc}} i_{\mathrm{jc}}\right) \Delta t\,. \tag{15}$$

$$W_{\mathrm{Q}} = \sum_{0}^{t=T_1/2} q_{\Sigma \mathrm{j}} \Delta t = \sum_{0}^{t=T_1/2} \left(u_{\mathrm{ja}-T/4} i_{\mathrm{ja}} + u_{\mathrm{jb}-T/4} i_{\mathrm{jb}} + u_{\mathrm{jc}-T/4} i_{\mathrm{jc}}\right) \Delta t\,. \tag{16}$$

Here, Δt is the discretization interval of dependencies $p_{\Sigma}(t)$ and $q_{\Sigma}(t)$, while $\mathrm{j} - T/4$ denotes the number of a discrete value of the voltage shifted by a quarter-period in relation to a current discrete value.

Figure 3 shows the dependence of the coefficient K_{W} on time constant τ.

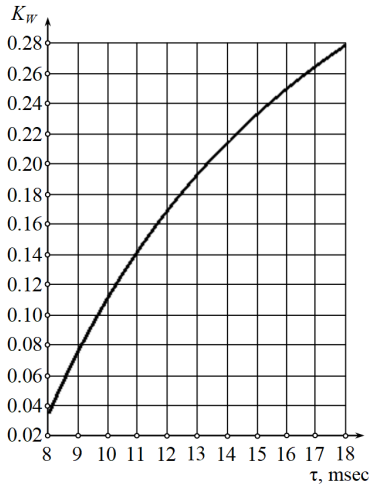

Fig. 3. Dependence of coefficient K_{W} on time constant τ

As can be seen from thisn dependency, if τ varies from 10.06 msec ($\cos\varphi = 0.3$) to 15.6 msec ($\cos\varphi = 0.2$), i.e. 1.54 times as much, the values of K_{W} vary from 0.13 to 0.243, i.e. 2.16 times as much. Therefore, K_{W} is a significant parameter to find a time constant change of the motor winding when it is heated up, as well as to find motor winding temperature.

Therefore, controlling the increase of heated winding resistance and motor temperature prior to each start is possible based on the analysis of the dependency $\tau = f(K_{\mathrm{W}})$ of τ time constant on K_{W} of active and reactive power ratio without using additional units of measuring winding resistance and control devices. Thus, the protection device structure is simplified and financial expenditures for its manufacturing are decreased. Moreover, due to the fact that the analysis of relationship of K_{W} is being done quickly, i.e. in 10 msec, responsiveness of motors themselves and process equipment operated in the intermittent and short time mode being provided.

The algorithm of creating the motor protection against over-currents with winding temperature control through analyzing active W_{P} and reactive W_{Q} powers during first 10 msec of a current change is as follows: at each motor start, coefficient K_{W} is determined. Once the K_{W} value is determined, the electric loop electromagnetic time constant τ_{Θ} (corresponding to winding heating up to temperature T_{Θ} at the next start moment), should be found. Values of τ and K_{W} are related by the dependence in Fig. 3. Comparing τ_{Θ} corresponding to the motor winding heated state with a set (known) $\tau_{T_{\mathrm{kn}}}$ at the set temperature T_{kn} and determining the heated winding time constant decrease the coefficient

$$K_{\tau} = \frac{\tau_{T_{\mathrm{kn}}} - \tau_{\Theta}}{\tau_{\Theta}} \tag{17}$$

allow to easily find the corresponding increase of heated winding active resistance and winding T_{Θ} temperature at the next start moment:

$$T_{\Theta} = \frac{K_{\tau}}{\alpha_{\mathrm{cu}}} + T_{\mathrm{kn}}\,, \tag{18}$$

where α_{cu} is the copper resistance temperature coefficient.

Figure 4 shows a diagram, which illustrates operation of a micro-processing device, when implementing the proposed method of protecting a motor against overloading currents.

Separate calculation and logical operations produced by the microprocessor are pictured as modules. The indicated modules do not exist physically, however their representation is necessary to easily understand the micro-processing device functioning, when implementing the proposed method of protection.

The micro-processing device functions as follows:

In each phase a, b, c, by means of motor winding continuous measurement of phase currents, their analogue-digital conversion into discrete values $i_{\mathrm{j(a,b,c)}}$ through the method of square integration of the obtained discrete values i^2_{ja}, i^2_{jb}, i^2_{jc}, active values of phase currents I_{a}, I_{b} and I_{c} are determined. If values I_{a}, I_{b} or I_{c} are more than an overloading current set point I_{L}, a controlling signal is generated to trigger

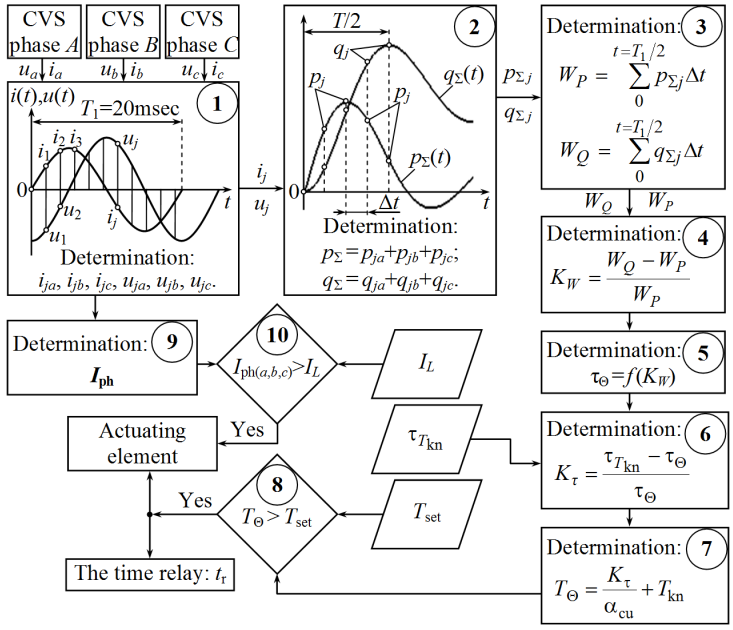

Fig. 4. Algorithmic diagram of micro-processing device operation to protect induction motors against winding overheating

protection with time delay t_{L}. Moreover, at each repetitive start of the motor the measurement of either line voltages u_{jab}, u_{jbc}, u_{jac} is done by 2 watt-meters, or phase voltages $u_{\mathrm{j(a,b,c)}}$ are measured by one watt-meter with an artificial neutral point. Through multiplying discrete values of current $i_{\mathrm{j(a,b,c)}}$ by corresponding discrete values of voltage, the dependencies on time t of instantaneous powers $p_\Sigma(t)$ and $q_\Sigma(t)$ consumed by the motor at its start are determined. Values of active W_{P} and reactive W_{Q} energies are determined in the time period, which equals to the period half T_1 of the start current change. Through the ratio of active W_{P} and reactive W_{Q} energies the temperature T_Θ of the motor heated winding is found.

1. In module 1 (Fig. 4) analogue signals from SCV sensors of currents/voltages of phases a, b, c are converted into discrete values $i_{\mathrm{j(a,b,c)}}$ and $u_{\mathrm{j(a,b,c)}}$.

2. In module 2 dependencies of time function of quasi-instantaneous power values $p_\Sigma(t)$ of equation (2) and $q_\Sigma(t)$ of equation (3) are found. The powers are consumed at the motor start.

3. In module 3 values of active energy W_{P} according to formula (11) and reactive energy W_{Q} according to formula (13) are determined. The electric energies are consumed at the motor start.

4. In module 4, coefficient K_{W} of equation (14) is found.

5. In module 5, at the motor start moment, the time constant τ_Θ of the heated winding is found from the dependency $\tau = f(K_{\mathrm{W}})$.

6. In module 6, according to equation (17), the coefficient K_τ is found. It features a decrease of time constant τ_Θ of the heated winding $\tau_{T_{\mathrm{kn}}}$ in comparison with the

winding temperature, at which standard operation life of the insulation is provided.

7. In module 7, the temperature T_Θ of the heated motor winding is determined according to equation (18).

8. In module 8, the value of T_Θ is found and compared with the temperature T_{set}, and if $T_\Theta \geq T_{\text{set}}$, control signals trigger the protection and form the time delay for the next switching time t_{r} are generated.

9. In module 9, active values of phase currents I_{a}, I_{b}, I_{c} are found.

10. In module 10 the values of I_{a}, I_{b}, I_{c} are compared with the maximal current set point I_{L}. If a current value in any of phases is higher than I_{L}, "Yes" control signal to a protection element (an independent breaker of a circuit breaker) is sent.

The micro-processing device, when operating according to the indicated algorithm, forms new, enhanced (compared with conventional ones) behavior protecting against overload currents of motors that operate in the intermittent and short time mode. In this case the stipulated control over motor winding temperature modes is not equipped with thermistors. Compared with similar protection solutions it has no additional units of measuring resistance to control temperature of the motor heated winding.

5. Conclusion

The method of finding electric loop parameters through analyzing irregularities of extreme values of instantaneous power consumed in the transient mode of current disturbance is developed.

The discovered method of thermal protection of electric motors that operate in the intermittent and short time mode against winding overheating at overload currents uses the direct temperature control of the stator winding through calculation of its active resistance increase.

The quick, real time calculation of hot state stator winding active resistance during first 10 msec upon the start current occurrence and the resistance comparison with one of the cold state without additional devices of resistance measurement/ control allow to significantly enhance features of electric motor protection equipment, significantly simplify their structure and decrease financial expenditures for their manufacturing.

References

[1] N. M. Basov: *A new direction in the development of mine explosion-proof transformer substations for low voltage up to 3300 V - Novoe napravlenie v sozdanii rudnichnych vzryvozashchischennych transformatornych podstancij na nizshee naprjazhenije do 3300 V.* Explosion-proof electrical devices, proceedings of scientific works, Doneck: OOO "AIR" (2010), 61–71. In Russian.

[2] I. Ya. Chernov: *Analysis of technical and operational indicators of modern foreign explosion-proof transformer substations - Analiz techniko-expluatacionnych pokazatelej sovremennych zarubezhnych vzryvozashchischennych transformatornych podstancij.* Explosion-proof electrical devices, proceedings of scientific works, Doneck: OOO "AIR" (2010), 74–89. In Russian.

[3] M. A. Valenzuela, P. Reyes: *Simple and reliable model for the thermal protection of variable-speed self-ventilated induction motor drives.* IEEE Transactions on Industry Applications *46* (2010), No. 2, 770–778.

[4] P. Zhang, B. Lu, T. G. Habetler: *A remote and sensorless stator winding resistance estimation method for thermal protection of soft-starter-connected induction machines.* IEEE Transactions on Industrial Electronics *55* (2008), No. 10, 3611–3618.

[5] P. Zhang, Y. Du, B. Lu, T. G. Habetler: *A DC signal injection-based thermal protection scheme for soft-starter-connected induction motors.* IEEE Transactions on Industry Applications *45* (2009), No. 4, 1351–1358.

[6] P. Zhang, Y. Du, T. G. Habetler, B. Lu: *Improving thermal recovery time for soft-starter-connected AC motors with intermittent periodic duty cycles.* Proc. IEEE International Symposium on Diagnostics for Electric Machines, Power Electronics and Drives, 31 Aug.–3 Sept. 2009, Cargese, France (2009).

[7] Z. Gao, T. G. Habetler, R. G. Harley, R. S. Colby: *A sensorless adaptive stator winding temperature estimator for mains-fed induction machines with continuous-operation periodic duty cycles.* IEEE Transactions on Industry Applications *44* (2008), No. 5, 1533–1542.

[8] Z. Gao, T. G. Habetler, R. G. Harley: *A complex space vector approach to rotor temperature estimation for line-connected induction machines with impaired cooling.* IEEE Transactions on Industrial Electronics *56* (2009), No. 1, 239–247.

[9] A. N. Zakladnoy: *Methods for estimating the lifetime of induction motors - Metody ocenki sroka sluzhby asinchronnych elektrodvigatelej.* Energetika ta elektrifikacija (2010) No. 4, 63–67. In Ukrainian.

[10] P. Zhang, Y. Du, J. Dai, T. G. Habetler, B. Lu: *Impaired cooling condition detection using dc signal injection for soft-starter-connected induction motors.* IEEE Transactions on Industrial Electronics *56* (2009), No. 11, 4642–4650.

[11] P. N. Shah, S. N. Patel, J. A. Patel, U. S. Vani: *Novel setting and design of relay for protection of 3-phase induction motor using PSCAD.* International Journal of Research in Engineering and Technology *4* (2015), No. 2, 554–561.

[12] L. A. Daniloy: *General electrical engineering with basic electronics - Obshchaja elektrotechnika s osnovami elektroniki.* Vyshshaja shkola (2005).

[13] P. Zhang, B. Lu, T. G. Habetler: *An active stator temperature estimation technique for thermal protection of inverter-fed induction motors with considerations of impaired cooling detection.* IEEE Transactions on Industry Applications *46* (2010), No. 5, 1873–1881.

[14] S. Cheng, Y. Du, J. A. Restrepo, P. Zhang, T. G. Habetler: *A nonintrusive thermal monitoring method for induction motors fed by closed-loop inverter drives.* IEEE Transactions on Power Electronics *27* (2012), No. 9, 4122–4161.

[15] P. Zhang, Y. Du, T. G. Habetler: *A transfer-function-based thermal model reduction study for induction machine thermal overload protective relays.* IEEE Transactions on Industry Applications *46* (2010), No. 5, 1919–1926.

[16] *IEC 60085:2007 «Electrical insulation – Thermal evaluation and designation* (2007).

[17] *TeSys control gear.* Catalog Schneider Electric (2007).

[18] *Low-voltage equipment.* Contactors, control relays, electric motor protection devices: Technical catalog ABB (2010).

[19] *Starting and protection of electric motors.* Moeller product catalog (2009).

[20] *Low-voltage control and distribution devices Siemens.* Catalog LV1 Siemens (2007).

[21] V. F. Sivokobylenko: *Ways of implementing the thermal protection of induction motors based on measurement of the input resistances - Sposoby realizacii teplovoj zashchity asinchronnych elektrodvigatelej osnovannye na izmerenii vchodnych soprotivlenij.* Proc. Scientific works of Doneck National Technical University, series Electrical engineering and power engineering, Doneck (2008), *140*, No. 8, 13–18. In Ukrainian.

[22] V. F. Sivokobylenko: *Thermal protection of the induction motor with cage rotor with unbalanced voltage - Teplovaja zashchita asinchronnogo dvigatelja s korotkozamknutym rotorom pri nesimmetrii pitajushchego naprjazhenija.* Vesnik KDPU imeni Michaila Ostrogradskogo, Kremenchuk (2009) *56*, No. 3, Part 2, 74–78. In Ukrainian.

[23] G. A. Bugaev, E. Ju. Erochin, A. N. Leont'jev, M. A. Shamis: Patent No. 2227354 of the Russian Federation IPC H02H5/04, H02H7/06 *The thermal protection method of the induction motor and the device for its implementation* (2004).

Received October 25, 2017

Acta Technica *63* No. 3/2018, 447–458

Intelligent cyber-physical computer system and database for microclimate monitoring based on nanostructured sensors[1]

Halyna Klym[2,3], Oleksandr Berezko[2], Ivanna Vasylchyshyn[2], Yuriy Kostiv[2]

Abstract. Intelligent computer system for monitoring and control of microclimate parameters (temperature and/or relative humidity) using novel technologically modified nanostructured sensors were realized on specialized system on a chip. The local database with regular recording of information in memory was developed. Obtained data can be analyzed by two-processor sub-systems. Portable system for monitoring and control of microclimate parameters such as temperature and humidity were also realized on Arduino Uno for Android OS.

Key words. Intelligent system, database, microclimate monitoring, control.

1. Introduction

In the modern development of information technology the cyber-physical systems (CFS, i.e. complex platform related components for integration processes of physical and cyber worlds) are popular [1–4]. These CFSs are widely used in industrial control systems and management [5], for control and communication of components in network systems [6] wireless devices [7], security systems, navigation, intelligent buildings, power management, etc. [2–4]. Regardless of the architectural features of CFS, one of the components is intelligent sensor information and measuring components [8]. Sphere of their applications is constantly expanded. Sensors of temperature, pressure, humidity, ionizing radiation, gas pollution of the atmosphere

[1]This work was supported by Ministry of Education and Science of Ukraine under Project for young researchers No. 0116U004411 State Fund for Fundamental Research of Ukraine under Grant of President of Ukraine.

[2]Lviv Polytechnic National University, 12 Bandera st., Lviv, 79013, Ukrain; klymha@yahoo.com, halyna.i.klym@lpnu.ua,berezko@gmail.com,inadych@i.ua,yura.kostiv@gmail.com

[3]Corresponding author

- it is an incomplete list of sensors for their basic functionality. A special place in this list belongs temperature and humidity sensors (electronic devices to quantify the temperature and absolute/relative humidity), as monitoring and control of these parameters of the environment is an important task within using of CFS, relevance successful solution of which overemphasized.

Recent advances in related fields of science and technology have stimulated increased interest in the study of sensor elements. However, effective work of CFS is possible only if the provision of high-quality primary information. This requires a fundamentally new sensors based on modern functional nanomaterials with new physical effects [9–14], the use of sensors arrays highly sensitive, accurate and stable measurement channels [15, 16].

Significant work towards the creation of such sensor systems to control temperature, humidity, gases, pressure, light, were made known global manufacturers, including E + E Electronic, Honeywell, Sensorsoft, etc. This work is dedicated to the development of intelligent computer system (or CFS) using previously obtained technologically modified temperature, humidity and integrated temperature/humidity sensors based on functional ceramic nanomaterials [17–19] and database for microclimate monitoring and control.

2. Intelligent computer system

Hardware of computer system for monitoring and control of microclimate parameters was implemented on modern element base with modular organization working in the real time and can be used to complementation of database on environmental conditions. The microcontroller CY8C29466-24PVXI (programmed system on a chip, PSoC) contains all necessary modules and manages the work of all components. This system can be installed both indoors and outside, it provides measurement data processing and the relative humidity and temperature [20–22]. The basic requirements applying to the system: modularity of structure to connect new sensors, functionality in automatic mode, obtaining and initial processing of measured data, transmitting of measured data to a personal computer (PC) at its request in the automatic mode, acceptance and performance of PC commands (time synchronization, power on/off system calibration sensors, etc.), creation and support of local database for a long time with automatic accumulation of new data, open architecture hardware and software to build devices and embedding of new algorithms for environmental control [20].

Designed intelligent microprocessor system for microclimate monitoring and control contains level of sensors (humidity, temperature sensors and integrated temperature-humidity sensors, see Fig. 1). Signals from sensors transform into an electrical signal and fed to the input of analog-to-digital converter (ADC). The including scheme provides harmonization of output signals from sensors in the region of ADC. In addition to ADC the read-only memory (ROM), random access memory (RAM), processor and indicator (to application in domestic purposes) are connected to the system bus. These devices are typical microprocessor system in which the work program is stored in ROM, their implementation is in the processor and the data are stored in RAM.

The additional corrective scheme for including of active sensor elements are used to more accurate and linear accordance impressions and provide of nominal parameters (voltage/current) temperature and relative humidity sensors.

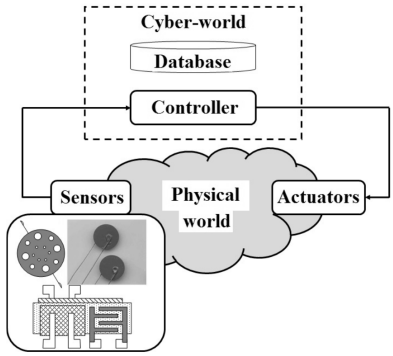

Fig. 1. Prototype of CFS for microclimate control using nanostructured sensors

Electrical principal circuit of system for monitoring and control of temperature and humidity is shown in Fig. 2. The CY8C29466-24PVXI microcontroller is used to measurement, calculation, processing and transmission of information via COM port using a level converter MAX-232. The 2×16 LCD display is applied to output of the measured values. Obtaining data from sensors is carried out with P0 [3] and P0 [5] ports and digitized by built ADC. There are micro-keys to change parameters and output of information in display.

To management of proposed system the software for microcontroller CY8C29466-24PVXI is developed using specialized PSoC Designer 5.4 program and C programming language. As was shown early in [20–22], proposed CFS can be placed indoors or outside. However, such system can be modified by adjusting their functionality by implementing a dual-system device (system or sub-system). The first sub-system can be placed inside to measure of temperature and relative humidity or integrated temperature-humidity of environment simultaneously.

This sub-system is determined to save data via RX+TX433: wireless module to another module that will be placed indoors. The second sub-system will be contained nonvolatile memory for data record from the first system and displayed on the LCD. If information output from the first system, information from the second system is recorded in nonvolatile memory and conversely. Data are presented as parameters with time codes and number of systems from which these data were received. The working algorithm of system is shown in Fig. 3.

Structural diagram of systems with two sub-systems realized on PSoC is presented in Fig. 4. It also contains an interactive menu for display data from both sub-systems (placed outside and indoors).

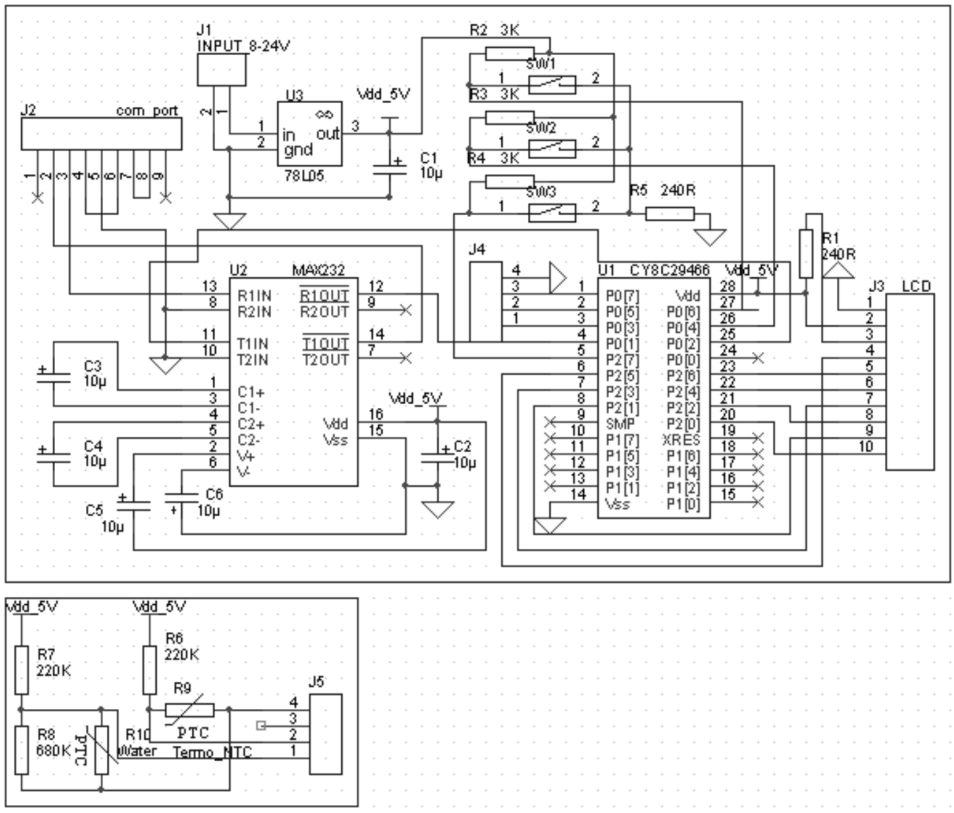

Fig. 2. Electrical principal circuit of system for monitoring and control of temperature and humidity based on PSoC

3. Database designing for registration and control of microclimate parameters

Software for system was created based on object-oriented language (java). Such choice will provide the necessity of work of the program on any calculable machines as well as simplification of programing process, time of implementation and increase of reliability. The system consists of hierarchy of objects. The "EnvironmentalMonitoring" class is based [20].

All other classes are succeed from it that provides connection of the program with vehicles facilities for the control environments and its subsequent implementation. The main window of the program allows to begin a new session, i.e., creation of new database with fixing of time and date of its creation or connecting fact to the existent base. Each 5 minutes the program polls port and fixes the information obtained from RS-232 in database, simultaneously executing data analysis. If amount of the measured indexes exceeds the level of the set values, the system executes the intermediate interrupt and warns a user about exceeding of possible information.

The system also provides fixing of exceeding information in a base. It works in a few modes: registration and control of temperature, relative humidity, as well as simultaneous registration and control of temperature and relative humidity.

In the case using of intelligent systems with sensors located in different places (complex control), the measuring modules will be able independently automatically to accumulate, partly to work over and memorize the previous information obtained from sensor. The system provides exchange of information with the central terminal intended for the centralized working and accumulation of information from all complexes. One operator can serve central terminal as well as system.

System software is proposed for interactive work regime with an operator. It will allow distantly to set all parameters for measurements, change intervals between measurements as well as to get information about work of each of sensors in an user-friendly form. In the ordinary mode each complexes will be able a few times per days to give the query. Obtained information will act on a central terminal without operator. In this case, complex must compare information from sensors with thresholds and give the report on a central terminal. The basic program window allows to begin a new session and to create a new database. Information obtained from RS-232 updates up 5 min. Structural scheme of connection of transmitter and receiver with program is shown in Fig. 5.

To visualization of program Visual.NET. library written in Visual Studio was used. This program consists of two windows: (1) program load window (Fig. 6) with name of the program, number of free sensors, and information whether we have access to our device, (2) the main window that displays information about connection of device to the computer, graphical dependences, etc. [20].

4. Portable system for registration of microclimate parameters for Android (based on Arduino)

In addition, the home-based web server's settings for displaying indoor and outdoor air temperature data and humidity levels are provided. The approach used in this case is based on using the Ethernet expansion card to communicate with the server over the network and other easily accessible peripheral devices (including sensors).

It should be noted that at changing settings on home router, the access to the data from a web server from a remote PC can be obtained. For this configure the mechanism for changing the network address in the IP datagram headings (NAT) and configure the DNS is needed so that when the provider returns IP address, Arduino has access to the network. The program for Android devices has been developed using Internet resource. The simple custom design for displaying the data was compiled was created using blocks presented in Fig. 7.

In general, proposed system consists of two main boards (Arduino Uno, Ethernet Shield) and temperature and humidity sensors. The nanostructured sensors based on ceramics in bulk [12, 23] and thick-film performance [19, 24] were used. Since the Ethernet completely covers the useful area of the Arduino and have same ports for connecting the periphery, all sensors are connected directly to it. Special wires were

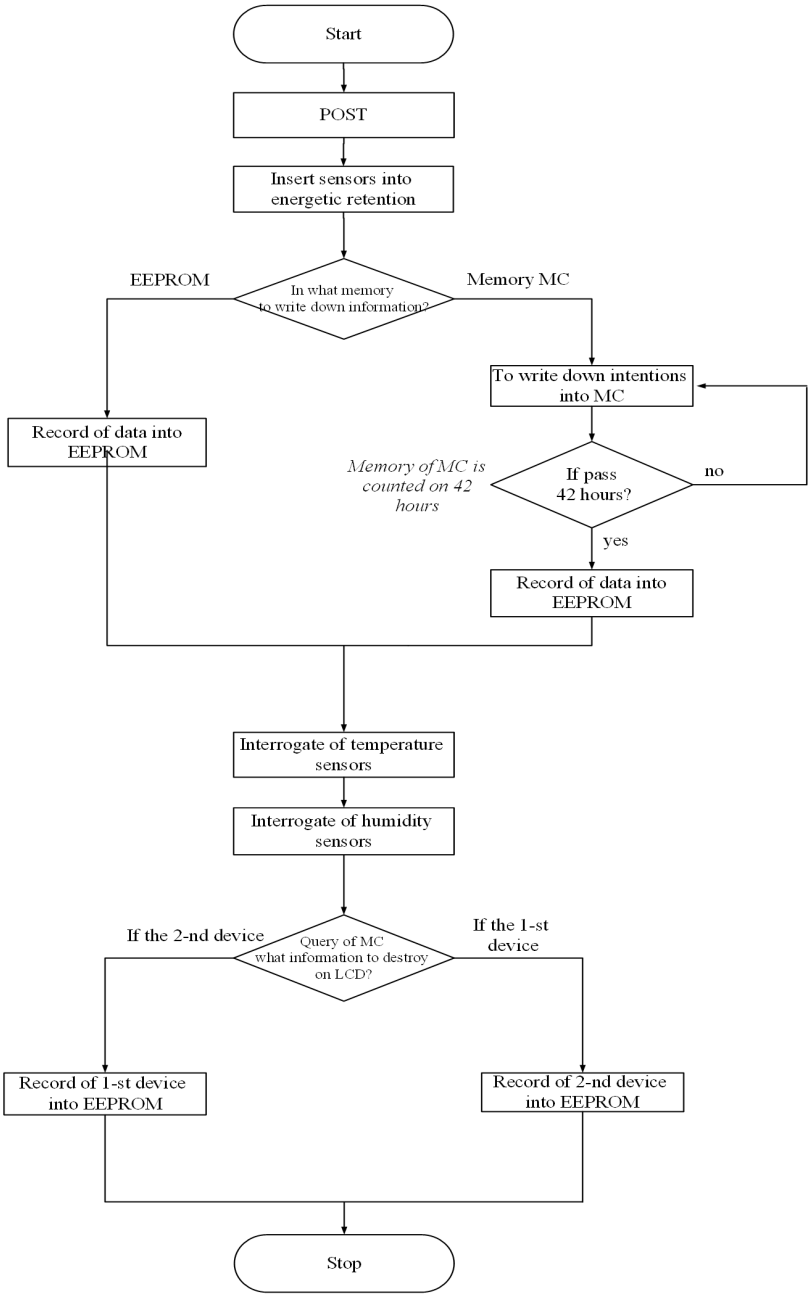

Fig. 3. Algorithm of information data treatment for computer-aided information systems

used to connect.

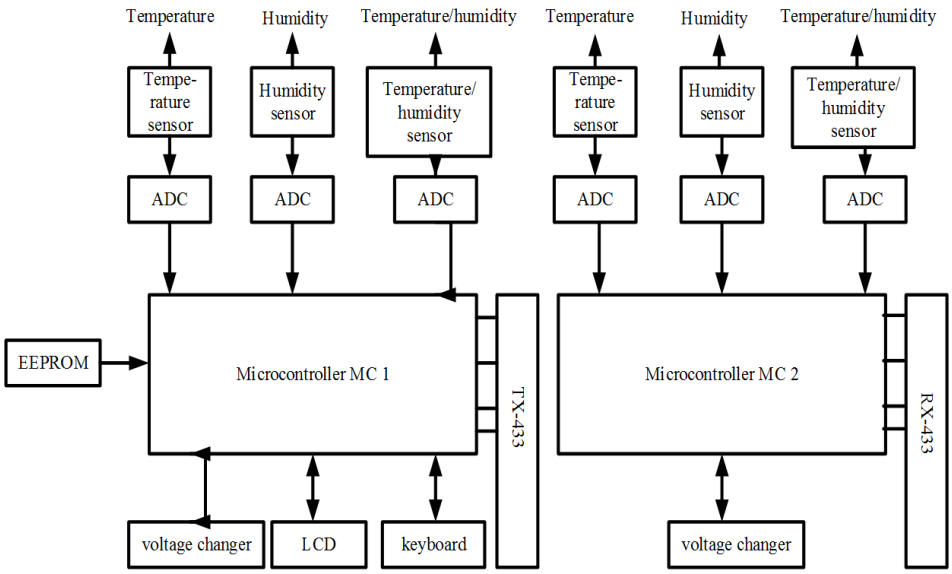

Fig. 4. Functional scheme of microprocessor information measuring system

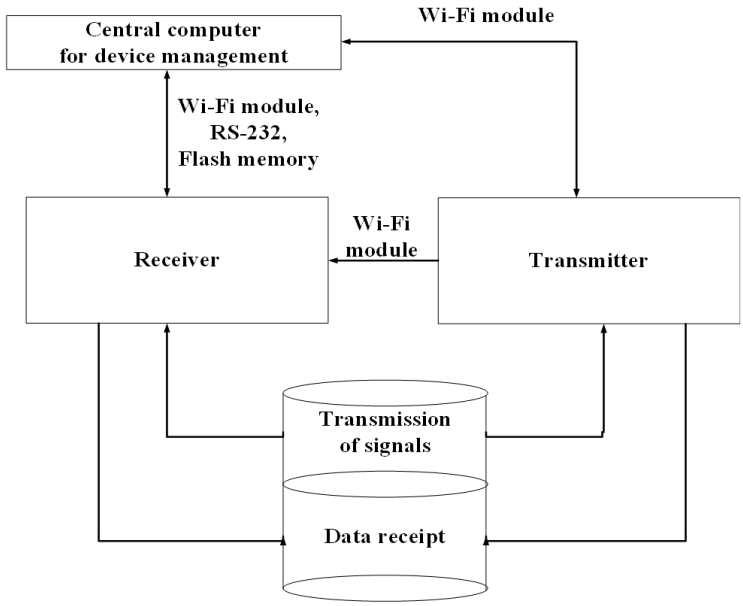

Fig. 5. Structural scheme of connection of transmitter and receiver with program

In proposed configuration of device, only one resistor (10 kΩ) was used, since most of the resistors, capacitors on the inductors coils are already inside the desired periphery or on Arduino. The correctness of the device was tested through the embedded development environment of the Serial Monitor tool (Fig. 8). After

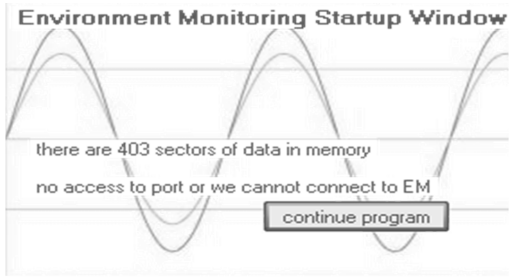

Fig. 6. Start program load window

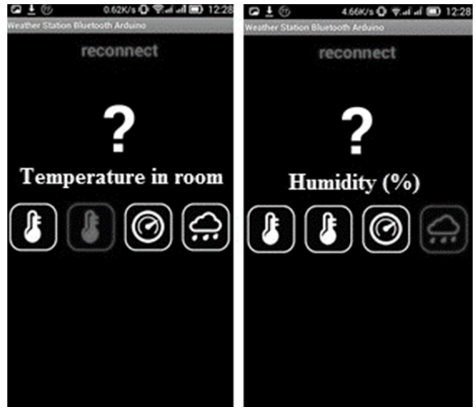

Fig. 7. Appearance of the application (without connecting to the main device)

connecting the device to PC (server) and performing a general setting, their work can be checked by navigating to the desired IP address in Internet browser (Fig. 9).

After connecting the mobile device to the designed system, the correctness of its operation can be checked (Fig. 10).

5. Conclusion

Intelligent CFS for microclimate control and monitoring using novel technologically modified nanostructured humidity- and temperature sensors was designed to monitor, collect, process, transmit, store and analyze of information on the state of the environment, forecasting their changes and development of recommendations for making decisions on the prevention of negative changes state of the environment.

Portable system for monitoring and control of microclimate parameters such as temperature and humidity were also realized on Arduino Uno. The nanostructured sensors based on ceramics in bulk and thick-film performance were used. The software for Android were developed. Low range of working voltage and opportunity of sensor operation in the energy severing mode reduce intensity, electric field stress and enhanced use of equipment. Lower dimensions and easy to implement make this device portable. Obtaining device can be integrated into smart house.

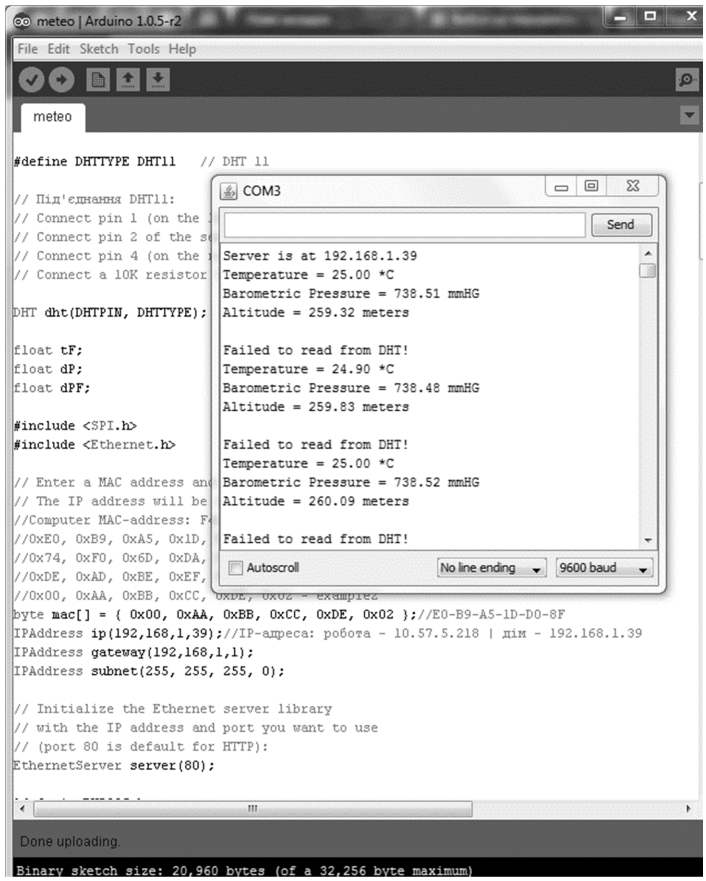

Fig. 8. Test mode of the device (displayed on the Serial Monitor)

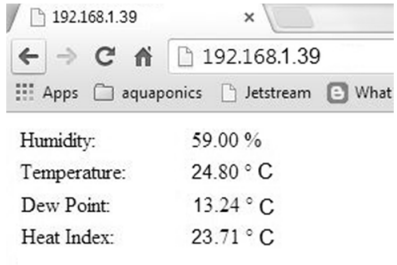

Fig. 9. Displaying data on a server

References

[1] W. Wolf: *Cyber-physical systems.* Journal Computer *42* (2009), No. 3, 88–89.

[2] L. Sha, S. Gopalakrishnan, X. Liu, Q. Wang: *Cyber-physical systems: A new frontier.* Machine Learning in Cyber Trust (2009), No. 2, 3–13.

[3] R. Baheti, H. Gill: *Cyber-physical systems.* The Impact of Control Technology *12*

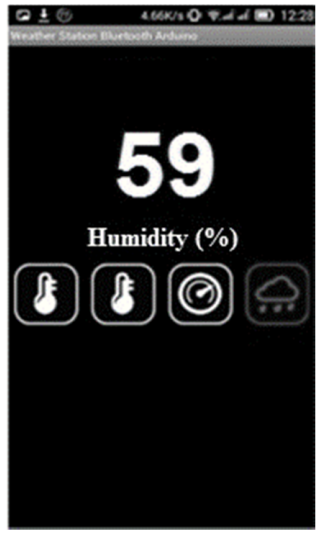

Fig. 10. Mobile device screen on Android OS

(2011), 161–166.

[4] L. Monostori: *Cyber-physical production systems: Roots, expectations and R&D challenges.* Procedia CIRP *17* (2014), 9–13.

[5] T. Schoeler: *The sepia cyber-physical production control system.* Electrotechnic and Computer Systems *13* (2014), No. 89, 197–202.

[6] X. Cao, P. Cheng, J. Chen, Y. Sun: *An online optimization approach for control and communication codesign in networked cyber-physical systems.* IEEE Transactions on Industrial Informatics *9* (2013), No. 1, 439–450.

[7] D. D. Hoang, H. Y. Paik, C. K. Kim: *Service-oriented middleware architectures for cyber-physical systems.* International Journal Computer Science and Network Security *12* (2012), No. 1, 79–87.

[8] X. Kong: *Analysis of sensor data in cyber-physical system.* Masters Thesis, University of Massachusetts Amherst (2013).

[9] H. Klym, A. Ingram, O. Shpotyuk, J. Filipecki, I. Hadzaman: *Extended positron-trapping defects in insulating $MgAl_2O_4$ spinel-type ceramics.* Physica Status Solidi(c) *4* (2007), No. 3, 715-718.

[10] H. Klym, I. Hadzaman, O. Shpotyuk: *Influence of sintering temperature on pore structure and electrical properties of technologically modified MgO-Al_2O_3 ceramics.* Materials Science *21* (2015), No. 1, 92–95.

[11] H. Klym, A. Ingram: *Unified model of multichannel positron annihilation in nanoporous magnesium aluminate ceramics.* Journal of Physics: Conference Series *79* (2007), No. 1, p. 012014.

[12] J. Filipecki, A. Ingram, H. Klym, O. Shpotyuk, M. Vakiv: *Water-sensitive positron trapping modes in nanoporous magnesium aluminate ceramics.* Journal of Physics: Conference Series *79* (2007), No. 1, p. 012015.

[13] H. Klym, A. Ingram, O. Shpotyuk, L. Calvez, E. Petracovschi, B. Kulyk, R. Szatanik: *'Cold' crystallization in nanostructurized $80GeSe_2$-$20Ga_2Se_3$ glass.* Nanoscale Research Letters *10* (2015), No. 1, p. 49.

[14] H. Klym, A. Ingram, O. Shpotyuk, J. Filipecki: *PALS as characterization tool in application to humidity-sensitive electroceramics.* International Conference on Microelectronics Proceedings (MIEL), 16–19 May 2010, Nis, Serbia, IEEE Conferences 239–242.

[15] H. Klym, V. Balitska, O. Shpotyuk, I. Hadzaman: *Degradation transformation in spinel-type functional thick-film ceramic materials*. Microelectronics Reliability *54* (2014), No. 12, 2843–2848.

[16] H. Klym, I. Kateryнchuk: *High-reliable temperature systems for sensor electronics*. International Conference on Modern Problem of Radio Engineering, Telecommunications and Computer Science, 21–24 February 2012, Lviv-Slavske, Ukraine, IEEE Conferences 490–490.

[17] H. Klym, I. Hadzaman, A. Ingram, O. Shpotyuk: *Multilayer thick-film structures based on spinel ceramics*. Canadian Journal of Physics *92* (2014), Nos. 7–8, 822–826.

[18] H. Klym, I. Hadzaman, O. Shpotyuk, M. Brunner: *Integrated thick-film nanostructures based on spinel ceramics*. Nanoscale Research Letters *9* (2014), No. 1, p. 149.

[19] M. Vakiv, I. Hadzaman, H. Klym, O. Shpotyuk, M. Brunner: *Multifunctional thick-film structures based on spinel ceramics for environment sensors*. Journal of Physics: Conference Series *289* (2011), No. 1, p. 012011.

[20] H. Klym, R. Kochan, I. Karbovnyk: *Nanostructured sensors in application to computer-based systems and electronics*. International Conference on Electronics and Nanotechnology (ELNANO), 21–24 April 2015, Kiev, Ukraine, IEEE Conferences 214–217.

[21] R. Dunets, H. Klym, R. Kochan: *Multi-functional nanostructured sensors and their adaptation into cyber-physical systems*. International Scientific and Technical Conference "Computer Sciences and Information Technologies" (CSIT), 14–17 September 2015, Lviv, Ukraine, IEEE Conferences 154–157.

[22] H. Klym, I. Hadzaman, I. Yurchak: *Design and properties of nanostructured thick-film structures for sensor microelectronics*. International Conference Mixed Design of Integrated Circuits and Systems (MIXDES), 19–21 June 2014, Lublin, Poland, IEEE Conferences 363–366.

[23] O. Shpotyuk, V. Balitska, M. Brunner, I. Hadzaman, H. Klym: *Thermally-induced electronic relaxation in structurally-modified* $Cu_{0.1}Ni_{0.8}Co_{0.2}Mn_{1.9}O_4$ *spinel ceramics*. Physica B *459* (2015), 116–121.

[24] I. Hadzaman, H. Klym, O. Shpotyuk: *Nanostructured oxyspinel multilayers for novel high-efficient conversion and control*. International Journal of Nanotechnology *11* (2014), Nos. 9–11, 843–853.

Received November 8, 2017

Acta Technica *63* No. 3/2018, 459–466

Development and research of characteristics of linear inductors for heating of steel ferromagnetic plates and tubes

A. B. Kuvaldin[1], M. A. Fedin[1],
M. L. Strupinskiy[2], N. N. Khrenkov[2]

Abstract. The research of electric and energetic characteristics of different versions of linear inductors for heating of steel ferromagnetic plates and tubes with the use of both industrial and elevated frequencies have been performed. The obtained results can be used in the development of pipeline and tank heating systems.

Key words. Linear inductors, induction-resistive heating, steel ferromagnetic plates and tubes.

1. Introduction

Induction and induction-resistive heating units of different types made in the form of linear inductors are used in petrochemical production for pipeline and tank heating. This type of heaters is outstanding due to its simple design and operating convenience, but still founds a limited application by virtue of insufficient engineering development of their design methods. The linear output level of these heaters normally ranges from 15 to 60 W/m and hardly reaches 100 W/m, when the current of industrial or elevated frequency is used.

Some application examples of the linear inductors, in particular for pipeline heating, are described in [1, 2] (see Figs. 1 and 2).

The applications analyzed in the paper are: heating of cylindrical surface of large size tanks that with a reasonable degree of accuracy can be replaced for the calculation by a flat plate, and also heating of pipelines where their cylindrical shape is taken into account. A study of energetic characteristics of heating system

[1]National Research University "Moscow Power Engineering Institute", Russia, Moscow
[2]Special Systems and Technologies, LLC, Russia, Mytischi, Moscow Region

Fig. 1. Pipeline of diameter $d = 400$ mm and length $l = 40$ m heated by two linear inductors laid along the pipe

for plates and pipes with the use of linear inductors depending in the heater's design option, inductor's current, supply voltage frequency and presence of ferromagnetic or electromagnetic shield have been performed.

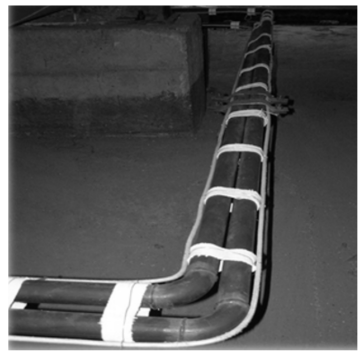

Fig. 2. Two parallel oil lines 150 m long, the maintained temperature being 90 °C

The linear (also known as rod type) inductor of round or rectangular cross-section, electrically insulated, is placed on the surface of steel ferromagnetic plate or pipe. The linear inductor may be equipped with magnetic conductor purposed to improve the energetic characteristics (Fig. 3).

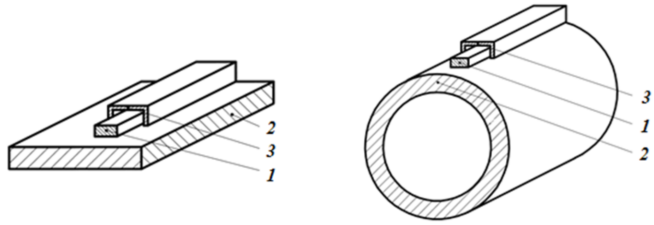

Fig. 3. Linear inductor for heating of steel ferromagnetic plate (left) and pipe (right): 1–linear inductor, 2–steel plate or pipe, 3–magnetic shield

When current flows through the inductor, electromagnetic field is created, due to which the plate or pipe is heated. The inductor itself is also heated and can serve as an additional source of heat, which means that a combined induction-resistive heating is realized. Using of a magnetic shield or electromagnetic screen enables to concentrate the magnetic field, whose energy is also converted to heat and should be taken into account in calculations.

2. Research and calculation methods

The following known methods can be used for the calculation of the electric and energetic characteristics of heating systems with linear inductors:

1. An analytical method developed by prof. G. I. Babat [3] for calculation of the parameters of linear inductor of round or rectangular cross-section without magnetic shield. The inductor–load system consists of the tape (inductor) located in parallel to indefinite metal plate. As a result of the research, a family of curves has been received showing distribution of the linear current density in the plate depending on the distance between the inductor and the plate.

2. An analytical method proposed by the assistant professor of the National Research University "Moscow Power Engineering Institute" A. M. Weinberg [4], based on calculation of the electromagnetic field energy by regions of the inductor–ferromagnetic load system (inductor, air gap between the inductor and the load, area outside the inductor).

3. An experimental-computational research method of N. I. Bortnichuk [5], in which the data of an experimental research of energy loss in steel sheets located near a current lead in form of a copper water-cooled conductor are used.

4. Numerical methods with the use of application software packages (ELCUT, FEMM, ANSYS/MAXWELL and others).

   In this paper, the software package ELCUT (QuickField), version 6.0 has been used.

3. The statement of the problem

The modern computer-based simulation methods enable to calculate the characteristics of the linear inductors taking into account the real object size and, most significantly, taking into account non-linear dependence of the magnetic permeability of steel on the magnetic field strength.

The calculations solve the alternating-current magnetic field plane problem. The magnetic fields produced by currents varies sinusoidally with time. At the same time, the currents induced in the load and in the magnetic conductor as well as heat power outputted in all elements of the electromagnetic system are calculated.

An example of the computational region used at simulation of a single inductor is shown in Fig. 4. The simulation is made with the following input data: the cores of the inductors are made of copper with conductance of 5.7×10^7 S/m. The electric insulation of the inductors is 2–3 mm thick with heat thermal resistivity of up to 250 °C. The electric conductance of steel is accepted to be equal to 5.5×10^6 S/m.

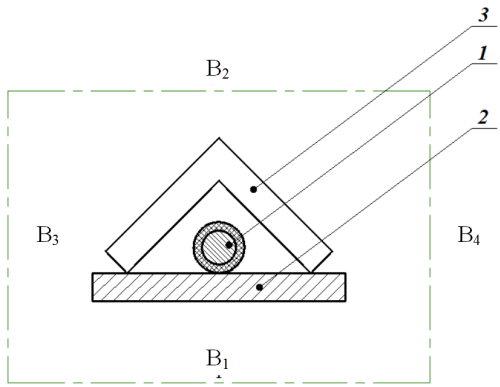

Fig. 4. Computational region with boundaries: 1–inductor with electrical insulation, 2–steel plate, 3–magnetic shield, B_1–B_4— boundaries of the computational region

The following assumptions were made in the calculation:

- the problem to be solved is flat,
- there are no end surfaces,
- the temperature dependencies of the cable electrical resistance and relative magnetic permeability of the steel plate are neglected,
- the magnetic induction B and the magnetic field strength H are sinusoidally varying with time. The boundary conditions on all boundaries of the computational region have been defined as $A = 0$ (Dirichlet condition),
- the magnetic permeability of the steel plates, pipes and magnetic shields are linearly dependent on the magnetic field strength.

The design options of the linear inductor are shown in Fig. 5: the unscreened inductor (a) and the inductor with ferromagnetic (b) and electromagnetic (c) shields. An alternating current flowing through the inductor produces an alternating electromagnetic field that results in heating of all elements of the electromagnetic system.

As an example, Table 1 shows the results of the calculation of the electric and energetic characteristics of the heating system of a ferromagnetic steel plate with copper inductor of a round cross section area of 8 mm^2 with current 100 A current of frequency 50 Hz. The shields are 4 mm thick; the relative magnetic permeability of the magnetic shield $\mu = 500$ (losses in the magnetic conductor are neglected).

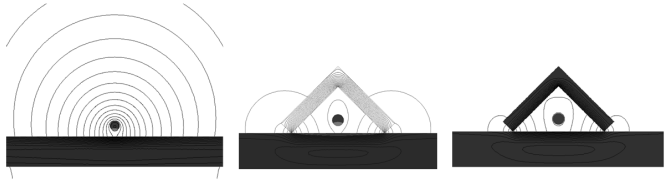

Fig. 5. Design versions of the linear inductor and magnetic field pattern: unshielded (left), with an ideal magnetic conductor (middle), with a steel angle (right)

In case of the electromagnetic shield (the steel angle, right option (in Fig. 5, approximately 3 W/m output is produced also in this angle.

From the data of Table 1, it follows that the part of the total power transferred to the steel plate due to the induction heating is small. In view of the above, a research of the heating at elevated frequencies was performed.

Table 1. Calculated electric and energetic characteristics of the system (Fig. 5)

Design option of the linear inductor	Total power output per 1 m of length (W/m)	Power factor	Supply voltage per 1 m of length (W/m)	Active power in the plate (W/m)
Unshielded option (left)	22.1	0.98	0.319	0.4 (1.7 %)
With magnetic shield (middle)	26.4	0.84	0.445	4.7 (17.8 %)
With electromagnetic shield (right)	27.1	0.92	0.416	2.3 (8.3 %)

Variants of a steel pipe heating by one and two unshielded linear inductors were considered. The location of the linear inductors and the pattern of the magnetic fields produced by the current of these inductors installed on the pipe are shown in Fig. 6.

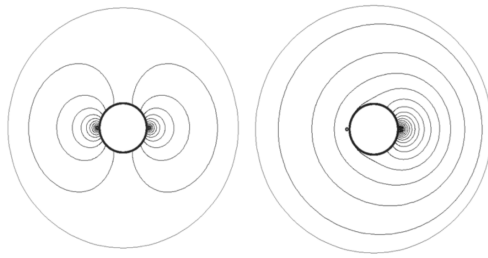

Fig. 6. Magnetic fields pattern near the pipeline heated by linear inductors: left–two symmetrically located inductors, right–single inductor

4. The results of the inductors' parameters calculation at various current frequencies

The calculations have been performed for the inductors of a round cross section area of 8 mm^2 and the heated pipe is 100 mm in diameter and 4 mm wall thickness. The results of the calculation of the total power output and of the output in the pipe caused by the induced current for the induction heating system with a single and double inductor are shown in Tables 2 and 3. The calculations are made for several inductor current and frequency values taking into account non-linear dependence of the magnetic permeability of steel on the magnetic field strength. The first value in the table cell is the total power output and the second one is the output induced in the pipe.

Table 2. Characteristics of the heating system with a single inductor

Inductor current (A)	Total power output and the output induced in the pipe (W/m) at a current frequency (Hz)			
	400	1000	2400	8000
50	5.85 / 0.49	6.8 / 1.4	9.56 / 3.96	25.8 / 18.5
100	23.3 / 1.62	27.0 / 5.13	38.9 / 16.1	110.6 / 81.0

Table 3. Characteristics of the heating system with a double inductor

Inductor current (A)	Total power output and the output induced in the pipe (W/m) at a current frequency (Hz)			
	400	1000	2400	8000
50	12.2 / 1.4	14.2 / 3.4	22.2 / 11.0	66.3 / 51.7
100	48.0 / 4.5	58.2 / 14.4	92.8 / 47.2	289 / 230

The data from the Tables 2 and 3 demonstrate that with the increase of the frequency and inductor current, the power output in the system and in the pipe can be achieved that enables to solve many problems of liquids transportation by pipelines.

The voltage drop values per unit length of the linear inductor were also calculated. Taking into account the limitations of the maximum allowable voltage on the linear inductor, it became possible to determine the maximum length of the heated pipe segment that is important for the systems design. For the inductor current and frequency values shown in the Tables 2 and 3, the possible heated pipe length, at 800 V supply voltage, is 1400–700 m at 400 Hz and 100–50 m at 8000 Hz.

The influence of the magnetic shield on the characteristics of the induction systems with linear inductors has been also investigated for the case when the elevated frequencies are used. It has been found that the total power of the system with the inductor shielded by the magnetic shield significantly increases with frequency but

at that the length of the heated pipe segment becomes by 40–50 % lower at the same supply voltage.

5. Conclusion

The linear inductors with the use of the elevated power frequencies can be successfully used for heating of relatively short pipeline segments (up to 1000 m) that is determined by limitations of the maximum allowable voltage. At the same time, the use of these inductors enables to obtain sufficiently great linear output values (of up to 300–400 W/m but on the length of not more than 100 m) that makes it possible to heat up the transported products in a pipeline.

The results obtained can serve as the basis for the development of design and construction methods for heating systems using the linear inductors.

References

[1] A. B. Kuvaldin: *Induction heating of ferromagnetic steel - Indukcionnyj nagrev ferromagnitnoj stali*. Energoatomizdat, Moscow (1988). In Russian.

[2] I. A. Makulov, Yu. A. Nikitin: *Equipment and application features of induction heating in oil-and-gas industry - Oborudovanije i osobennosti primenenija indukcionnogo nagreva v njeftjegazovoj promyshlennosti*. Industrial Electric Heating (2014), No. 3, 50–53. In Russian.

[3] G. I. Babat: *Induction heating of metal and its industrial application - Indukcionnyj nagrev metalla i ego promyshlennoe primenenije*. Energy, Moscow (1965), 94–95. In Russian.

[4] A. M. Weinberg: *Induction melting furnaces - Indukcionnye plavil'nye pechi*. Energy, Moscow (1967). In Russian.

[5] N. I. Bortnichuk: *Determination of losses in steel sheets/Research in the field of the industrial electric heating - Opredelenie potjer' v stal'nych listach/Issledovanija v oblasti promyshlennogo elektronagreva*. Publishing House VNIIEM, (1965). In Russian.

Received December 12, 2017

Acta Technica *63* No. 3/2018, 467–474

Enhancing optimal performance of the platinum concentrates by reduction sulfuric acid

M. S. Melnichuk[1], G. V. Petrov[1], S. B. Fokina[1], I. E. Zotova[1]

Abstract. Extension and restructuring of raw recourses of the platinum group metals by low-sulfide ores processing makes an important direction for development of the mining and metallurgical industry of the Russian Federation. The platinum group metals (PGM) concentrates, recovered during low-sulfide ores processing, have too high iron content and do not meet the requirements of the refineries. Objective: create a comprehensive technology for processing of ferrous platinum-bearing products of low-sulfide ores in order to recover PGM-rich concentrates. Methods used: we carried out electrochemical studies of the magnetite cathodic reduction in the sulfuric acid applying the IPC-Pro potentiostat and an electrochemical cell. Experimental studies of the sulfuric acid leaching patterns employed a model magnetite concentrate; and included a study of the influence of technological process variables: consumption of iron powder, duration of the process, concentration of sulfuric acid and temperature. Novelty: the primary novelty of this work is identification of basic kinetic patterns of magnetite sulfuric acid leaching. Results: we calculated the apparent activation energy of the process, which proves that constraining factors of the electrochemical process are mostly kinetic in nature. We also defined optimal variables of the sulfuric acid leaching with a reducing agent, which ensure practically complete leaching of iron from magnetite concentrates. Practical relevance: we proposed a technology of hydrometallurgical refining of the platinum concentrates from iron.

Key words. Low-sulfide ores, PGM concentrates, magnetite, sulfuric acid leaching, refining.

1. Introduction

Various compositions of ores and applied processing technologies greatly affect the content of platinum group metals (PGM), non-ferrous metals, iron and silicates in platinum-bearing products, which dictates principles for their further processing [1, 2].

[1]Saint-Petersburg Mining University, Saint Petersburg, Russian Federation 199106, Saint-Petersburg, Vasilievsky Island, 21st Line, 2

The PGM concentrates, recovered during processing of copper and nickel electrorefining anode slime, meet the requirements of the refineries, and their processing does not cause difficulties in general [3–5].

Chemical and phase composition classification of platinum-bearing products of beneficiation of various raw materials allows us to distinguish the following types: rich gravity concentrates, recovered during beneficiation of magnetite tailings of sulfide Cu-Ni ore processing (up to 5 kg/t of PGM) [6]; flotation concentrates from beneficiation of low sulfide ores, containing up to 1 kg/t of PGM [7]; magnetite concentrates, recovered during beneficiation of the Nizhny Tagil alluvial ores (up to 1050 g/t of PGM) and poor dunite raw materials (up to 50 g/t of PGM) [8]; gravity platinum concentrates, recovered during beneficiation of the Aldan chromites (20–300 g/t of PGM).

In low-sulfide concentrates, a highly-dispersed nature of the PGM minerals, which are mostly complex chalcogenides and sulfoarsenides, requires chemical-metallurgical methods of liberation that convert the PGM into a solution, followed by recovery through well-known methods [7]. To process iron-bearing low-sulfide concentrates, it is worthwhile to use hydrometallurgical processes focused on selective dissolution of iron, with precious metals concentrated in a compact insoluble leaching residue. This policy is most often used in technological solutions for the titanium metallurgy, where raw materials are concentrates bearing minerals with high content of iron (ilmenite, titanomagnetite) and silica.

A promising method for purifying a platinum-bearing concentrate from iron is its leaching in a sulfuric acid with a reducing agent. An obvious advantage of the reduction sulphate leaching is that the platinum group metals virtually do not pass into solution.

2. Research methods

Study of the influence of magnetite cathodic reduction on its dissolution rate makes it possible to reveal the nature of the rate-limiting stage and the mechanism of oxide dissolution. We carried out electrochemical studies of the magnetite cathodic reduction in the sulfuric acid applying the IPC-Pro potentiostat and an electrochemical cell consisting of a working magnetite electrode (Fe_3O_4), a chlorine-silver reference electrode, and an auxiliary platinum electrode. The magnetite cathodic polarization was made in the potentio-dynamic mode with a sweep rate of 5 mV/s.

Experiments to study the patterns of reductive sulfuric acid leaching employed a model magnetite concentrate containing (%): 52.1 Fe_2O_3; 1.2 MgO; 15.1 SiO_2; 24.9 Al_2O_3. We studied the influence of the main leach technological variables on the behavior of iron: consumption of iron powder (up to triple theoretical value), duration 0.5–1.5 hours, sulfuric acid concentration 50–250 g/l, temperature 323–343 K. Molar ratios Fepowder/Feconcentrate and the excess of the reducing reagent was calculated using the reaction:

$$Fe_3O_4 + Fe + 4H_2SO_4 = 4FeSO_4 + 4H_2O.$$

Iron recovered into the solution was determined as the ratio of the iron passed into the sulfate solution and the sum of iron in the concentrate and iron powder. The

experiments were carried out in a glass jar with mechanical stirring. The agitator rotation speed amounted to 400 rpm. To maintain the temperature, we used the ultra-thermostat UTU-2, with accuracy of ±0.2 1°.

3. Research results

Having analyzed the cathodic polarization curves, we came to a conclusion that the dissolution rate increases when the potential shifts to the cathodic zone with the growing solution acidity (50–200 g/l H_2SO_4) and the temperature rise (25–80 °C). The increasing rate of magnetite dissolution during cathodic polarization confirms that the kinetics of the electrochemical process is constrained by transition of protons from the solution to the oxide surface (Figs. 1, 2).

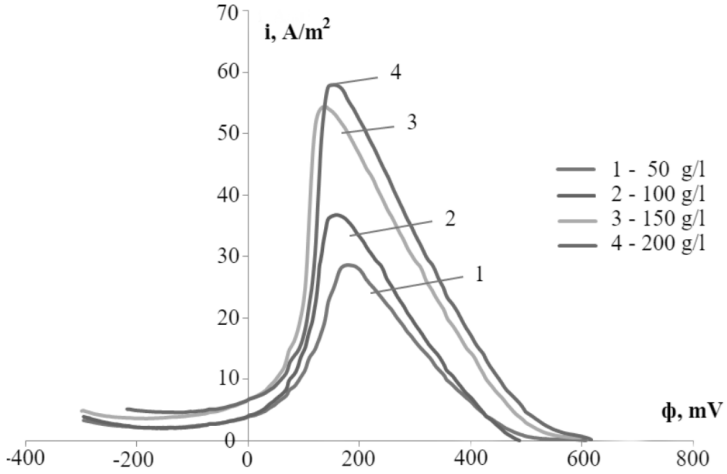

Fig. 1. Influence of acidity on magnetite cathodic polarization

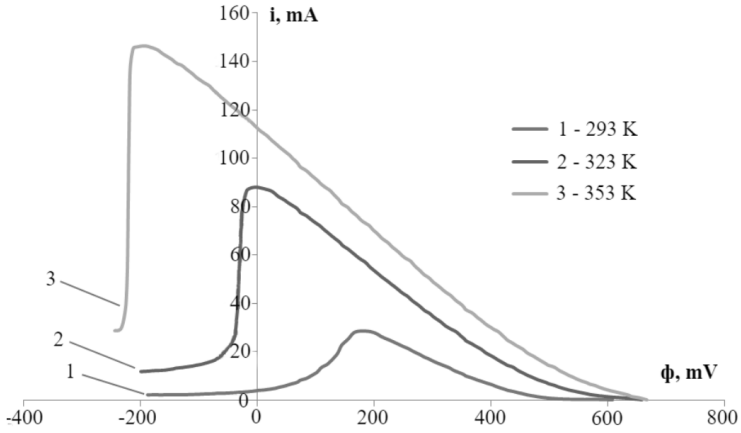

Fig. 2. Influence of the temperature on the magnetite cathodic polarization

The divalent iron ions in the solution minimize the induction period in the low over-voltages zone, thus making the process autocatalytic, and facilitate the accelerated dissolution of magnetite by time (Fig. 3). The calculated apparent activation energy of magnetite electrochemical reduction in the acid amounts to 46±3 kJ/mol, which indicates that the constrains are predominantly kinetic in nature.

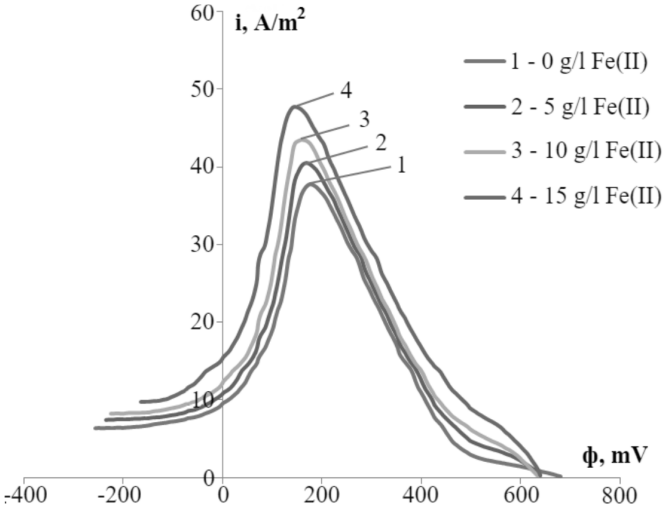

Fig. 3. Influence of the Fe (II) cations on the magnetite cathodic polarization

The experimental results of reductive sulfuric acid leaching are presented as dependency graphs of the iron recovery into the solution (α) and H_2SO_4 concentration on the process duration. The graphs indicate that an increase in the temperature from 323 to 343 K contributes to an increase in the iron leaching by 21 % (from 68 % to 89 %). The boat-shaped kinetic curves, flowing from "parabolic" to linear, indicate a monotonic decay of the process speed after 1 hour of leaching, which is also confirmed by derivation of the experimental dependence of the iron content in the solid phase (1-α) on time (Figs. 4, 5).

The general equation of the Fe_3O_4 dissolution rate can be described as follows: (at T = const:

$$\frac{\mathrm{d}(1-\alpha)}{\mathrm{d}\tau} = -kS[\mathrm{H_2SO_4^n} \cdot [\mathrm{Fe}]^m\,, \tag{1}$$

where α and 1 - α, respectively, are the amount of iron (III), which passed into solution and remained in the solid phase, S denotes the surface of magnetite, varying in time (dm^2/g), [H_2SO_4] stands for the initial concentration of the sulfuric acid (mol/dm^3), n is the reaction order by acid concentration, [Fe] denotes the indicator accounting for the consumption of iron for recovery, (stoichiometry ratio), m is the reaction order by reductive agent, and k represents the reaction rate constant, (g·dm)/(mol·min).

To account for the change in the surface over time, we assumed that in the leaching process the surface varies proportionally to the amount of iron (III) in the

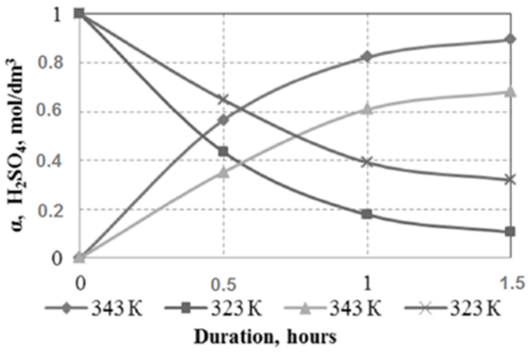

Fig. 4. Influence of the temperature on the liberation rate of the model magnetite concentrate molar ratio $\mathrm{Fe_{powder}/Fe_{concentrate}} = 4.14$, $L/S = 10:1$

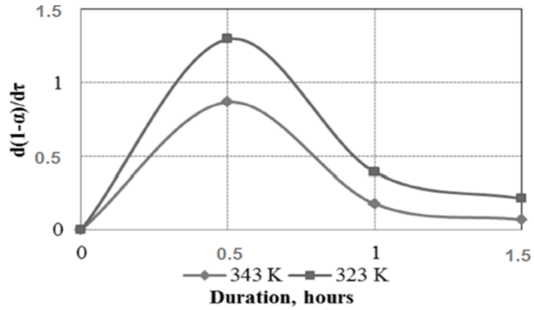

Fig. 5. Dependence of the iron leaching rate on temperature (initial concentration of the sulfuric acid in the solution 1.0 mol/dm^3, molar ratio $\mathrm{Fe_{powder}/Fe_{concentrate}} = 4.14$, $L/S = 10:1$

concentrate to β power:

$$S = S_0(1-\alpha)^{\beta}\,. \tag{2}$$

Then the rate equation looks as

$$\frac{\mathrm{d}(1-\alpha)}{\mathrm{d}\tau} = -kS_0(1-\alpha)^{\beta}[\mathrm{H_2SO_4}]^n \cdot [\mathrm{Fe}]^m\,, \tag{3}$$

where $\mathrm{S_0}$ is the initial specific surface area of the concentrate sample.

We assume that at different temperatures and concentration of $\mathrm{H_2SO_4}$ are constant during the experiment, Fe content in the concentrate decreases exponentially over time:

$$(1-\alpha) = \mathrm{e}^{CT} \tag{4}$$

where C is a coefficient, depending on the variables of sulfuric acid liberation (temperature, acid concentration and specific surface area of magnetite).

After logarithm and differentiation transformations of the equation (4), we get

$$\frac{\mathrm{d}(1-\alpha)}{\mathrm{d}\tau} = -C(1-\alpha)\,. \tag{5}$$

Comparing equations (3) and (5) we get $\beta = 1$, $C = kS_0[H_2SO_4]^n \cdot [Fe]^m$ and

$$\frac{d(1-\alpha)}{d\tau} = -kS_0(1-\alpha)[H_2SO_4]^n \cdot [Fe]^m . \tag{6}$$

The calculated process rate constants for temperatures 323 and 343 K amount to 4.21703 and 6.65326, respectively (see Fig. 6).

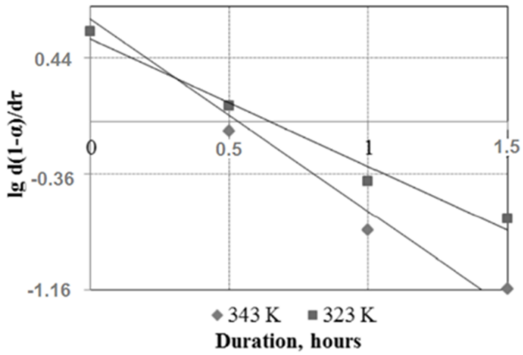

Fig. 6. Temperature-kinetic dependence of the leaching rate of the model concentrate

The dependence of the rate constant on the temperature can be recorded as follows:

$$k = (1.05 \pm 0.02) \cdot 10^4 \exp\left(-\frac{2525}{T}\right) . \tag{7}$$

The calculated value of the apparent activation energy of the magnetite concentrate reduction by iron powder (21.1 kJ/mol) is typical for processes occurring in the diffusion zone.

Experimental results indicate that an increase in the reducing agent consumption ($Fe_{powder}/Fe_{concentrate} = 1.4/4.2$) has a positive effect on the sulfuric acid dissolution of magnetite (see Fig. 7).

The data obtained show that the optimal process variables (sulfuric acid concentration–200 g/l, metallic iron excess - double theoretical value, temperature 70 °C, duration 1.5 hours, $L/S = 10 : 1$) ensure almost complete iron leaching from magnetite concentrates.

4. Conclusion

Application of this process to a platinum-rich concentrate, recovered during beneficiation of the Middle Urals alluvial ore (5.8 Cr %, 54.6 % Fe, 3.32 % MgO, 2.6 % SiO_2, 2.7 %Al_2O_3, 1050.0 g/t Pt), allows to achieve complete purification from iron and a significant reduction in the product (by 5–6 times). Refined platinum-rich concentrate (up to 0.59 % of platinum) can be directly delivered to the refinery facility. In case a poorer product is obtained (100–150 g/t), recovered from dunite raw

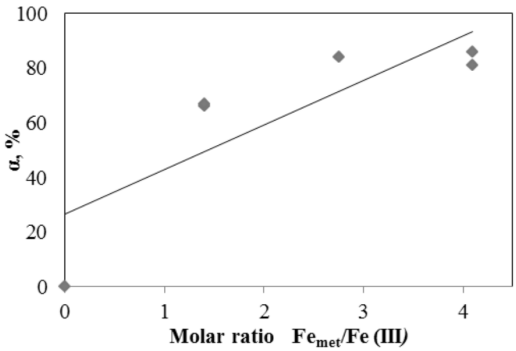

Fig. 7. Influence of the reducing agent consumption on the liberation of magnetite (1.5 hours at the temperature of 70 °C and excess of the solvent)

materials, for example, it can be processed together with platinum-bearing copper-nickel slimes. Summing up, we should note that sulfuric acid reduction leaching is an effective method for refining various types of ferrous concentrates beneficiated with precious metals.

References

[1] S. Cole, C. J. Ferron: *A review of the beneficiation and extractive metallurgy of the platinum-group elements, highlighting recent process innovations.* SGS Minerals Services, Technical Bulletin *54* (2002), No. 3, 811–818.

[2] N. A. Kolpakova, Y. A. Oskina, E. N. Dyachenko, A. Ya. Pshenichkin: *Determination of platinum metals in carbonaceous mineral raw materials by stripping voltammetry.* Procedia Chemistry *15* (2015), 335–341.

[3] S. A. Mastyugin, A. A. Korolev, V. G. Lobanov: *Development of hydrometallurgical scheme of processing of slimes of electrolytic copper with the release of refined metals and other types of finished products.* International Scientific-Practical Conference (2013), 124–125.

[4] D. Li, X. Guo, Z. Xu, Q. Tian, Q. Feng: *Leaching behavior of metals from copper anode slime using an alkali fusion-leaching process.* Hydrometallurgy *157* (2015), 9–12.

[5] A. Y. Bonusn: *Effect of roasting and leaching on the change in the phase composition of the main components electrolytic copper sludge.* Journal of Mining Institute *152* (2002), 194–196.

[6] M. A. Pashkevich, T. A. Petrova: *Technogenic impact of sulphide-containing wastes produced by ore mining and processing at the ozernoe deposit: Investigation and forecast.* Journal of Ecological Engineering *18* (2017), No. 6, 127–133.

[7] L. C. Seitz, T. J. P. Hersbach, D. Nordlund, T. F. Jaramillo: *Enhancement effect of noble metals on manganese oxide for the oxygen evolution reaction.* Physical Chemistry Letters *6* (2015), No. 20, 4178–4183.

[8] V. A. Chanturia, T. N. Matveeva, T. A. Ivanova, V. V. Getman: *Mechanism of interaction of cloud point polymers with platinum and gold in flotation of finely disseminated precious metal ores.* Mineral Processing and Extractive Metallurgy Review *37* (2016), No. 3, 187–195.

Received November 8, 2017

Acta Technica *63* No. 3/2018, 475–480

Development of water-shutoff composition on the basis of carboxymethyl cellulose for fractured and fractured-porous oil and gas reservoirs

A. Shagiakhmetov[1], D. Tananykhin[1], A. Terleev[1]

Abstract. The article is devoted to solving one of the most important problem of the oil industry – the high level of water cut. Different kinds of water shutoff agents were studied in the work and its advantages and disadvantages were claimed. The authors proved an actuality of the water inflow limitation problem in fractured and fractured-porous reservoirs. The laboratory research has established the dependency of the gelling kinetic and strength characteristic of the shutoff composition on reagent concentration by which optimum reagent concentration can be prompt determined for specific geological conditions. In addition, the gelling induction period was measured at shear rate that modelled a movement of the composition in fractured-porous reservoir for different spacing gaps between two resistors plates of the Rheotest unit. The determination of residual resistance in the sample of the rock with an artificially created crack was carried out by the filtration experiment.

Key words. Reservoirs, water-shutoff, gelation time, copper sulfate, fractured-porous.

1. Introduction

Modern period of oil production is characterized by deterioration in structure of reserves of oil fields, involvement in the development of heterogeneous reservoirs and fast transfer of the main operational objects to a final stage of the development accompanied with the significant level of water cut and low rate of wells oil discharge [1]. Currently, an accent of oil and gas fields development is moving to fractured reservoirs, because of it contains approximately 60 % of world's hydrocarbons reserves [2]. The prominent feature of fractured reservoirs is a vast influence

[1]Saint-Petersburg Mining University

of discrete systems on fluid flow in a formation, such as: cracks systems, system of open channels inside cracks systems and cavities [3]. Fractured reservoirs are, basically, represented by rock blocks which separated by cracks systems. Depending on filtration and capacitor properties of a matrix (skeleton) of a rock two main types of fractured reservoirs can be determined [4]:

1. Fractured without porosity. These reservoirs are compiled by impenetrable blocks which do not contain hydrocarbons inside. In these reservoirs oil locates in a system of associated cavity where the filtration happens. The volume of the cracks system usually varies from a few thousandths to one hundredth share of the volume of the rock (according to the data of complex rock samples field researches).

2. Fractures with porosity. Unlike previous one the major oil locates inside blocks of the porous environment where the cracks have a function of associated channels in which the filtration happens. The secondary porosity normally takes no more than 1 % of the whole rock volume.

In [5] stated that to restrain the too-fast rising of water cut in oil wells in Ordovician fracture-cavity carbonate reservoirs in Tahe Oilfield, two effective water shutoff agents (modified tannin gel water shutoff agent and flexible water shutoff agent) couls be used. The laboratory study of fracture-cavity carbonate cores plugged with the two agents shows that the increase of the agent injection leads to an increase of depth of plugging section and higher breakthrough pressure gradient in the initial stage; the accumulation of the shutoff agent makes the flow path narrower when a certain depth of plugging section is reached, raising the residual resistant factor. According to [6] the crosslinker/polymer ratio had more effects on the gelation time than did the polymer concentration and their interaction. A response surface method provides an optimum gel formulation. Core flooding experiments reveal that a significant permeability reduction on the sand pack cores can be achieved at reservoir conditions, when it is treated with an optimum gel formulation. Hence, this gel system may be suitable in the water shutoff job required for enhanced oil recovery from the oil fields.

The object of the study is oil-saturated layers with commercial oil content timed to Upper Devonian and relates to carbonate basins that contain about 95 % of the whole amount of oil reserves. Reservoir formations are formed by brown organogenic-detrital porous micro-cracked oil saturated limestones. These layers are described by a high stratification factor (>3). Reservoir water has a high mineralization (>100 g/l). Carboxylmethyl cellulose, organic salt of chromium (as a crosslinker) and aqueous solution of copper sulfate (as a catalyst) were used as a raw material for the gelling composition preparation. These reagents are non-toxic, widespread and cheap. Experimental of determination of physic-chemical, rheological and filtration properties of the gelling composition were carried out on a modern equipment in a laboratory of Production Stimulation Engineering in Saint-Petersburg Mining University. In the research the following parameters were determined: gelation time, plastic strength, induction period of gelation and residuary resistance coefficient. Researches of strength and gelation time dependence on carboxymethyl cellulose concentration, crosslinker and catalyst were held for determination of the optimum concentration of the developed water-shutoff composition. The gelation period was

measured in according to following principle: the compound was transfused to a transparent glass right after the mixing and covered by a piece of foil. Then, the glass was being tilted to an angle of 450 every 15 minutes. The compound could be considered gelled in case of the angle of the meniscus remained unchanged. Gelling composition is acceptable for production in case gelation time is between 2 and 24 hours [6].

The plastic strength was measured on a cone-and-plate rheometer (Rebinder machine) as follows: the cone of the known weight was fallen into the gelling composition and kept on there for 15 minutes. In the result, cones penetration depth into the gel was measured and the endpoint of the plastic strength was calculated. The compound is acceptable in case of the plastic strength is 3000 Pa [3].

Figure 1 shows dependence graphs of the gelation time and plastic strength vs the concentration of copper sulfate.

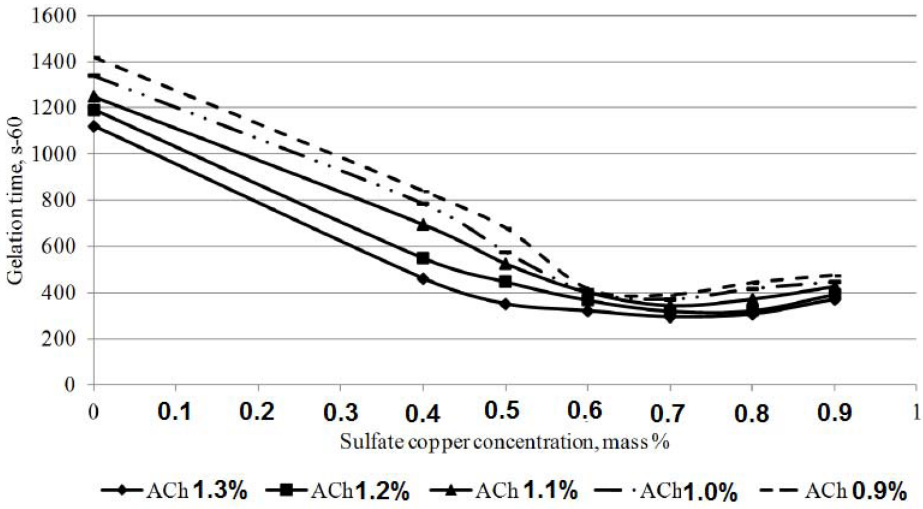

Fig. 1. The dependence of the gelation time vs the copper sulfate concentration

As can be seen from Fig. 1, all measured concentrations of copper sulfate and chrome acetate (III) are placed within the valid time of gelation. Furthermore, it should be taken into account, that the gelation time changes insignificantly when the concentration of the copper sulphate is higher than 0.6 %.

For induction period of gelation metering a rheometer Anton Paar MCR 102 which has a high measurement accuracy of different liquids was used. On the facility, the gap between the two plates can be changed in order to study the dependence of the induction gelation period vs the gap size. The method of the induction period determination is described further. The sample of the gelling compound is poured on the plate by a dosimeter; a certain gap, a temperature of 25 °C and a constant shearing rate of $5\,s^{-1}$ are established [7]. The experiment used to be stopped with the growth of the effective viscosity. The induction period of gelation was defined as time at which the effective viscosity remained unchanged with respect to the initial one.

Figure 2 shows the dependence of the effective viscosity of the gelling compound vs the time and the gap width ($\gamma = 5c - 1$).

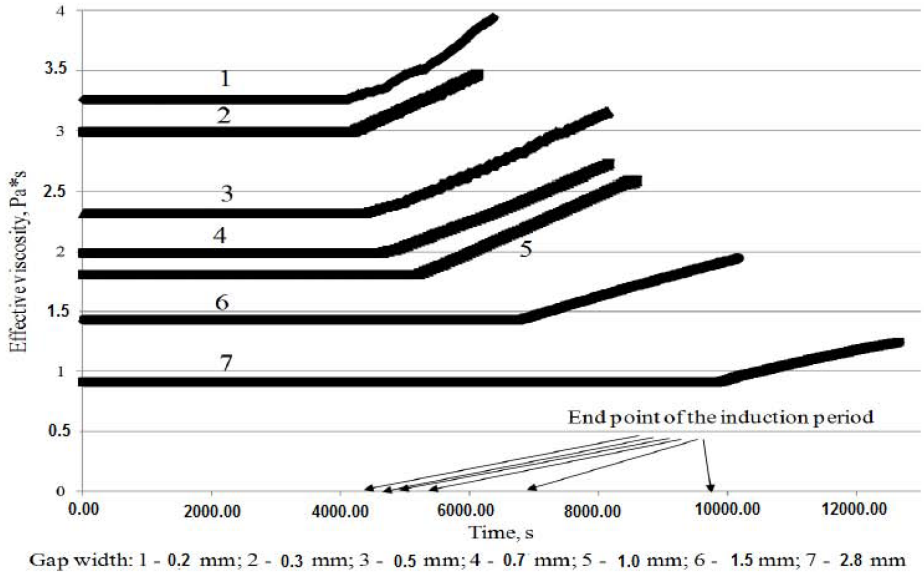

Fig. 2. Dependence of the effective viscosity of the gelling compound vs the time and the gap width ($\gamma = 5c - 1$)

The induction period of gelation is higher than 1 hour with different gaps. It is enough for pumping it into a fracture system.

To evaluate the effect of the gelling compound on the indicators of a fractured-porous reservoir development the filtration experiment of the residual resistance factor determination was conducted. The research was carried out on a filtration unit FDES-645 (Corotest Systems Corporation, USA). The rock sample from Mezelinskoe oil field with a pre-generated fracture was placed in a core holder [7]. The sample was saturated with a formation water with mineralization of 180 g/l in advance. At the first stage the formation water with a continuous flow of 0.5 ml/min was pumped up until pressure level-off. After that the gelling composition in a volume of the porous space was pumped. After the operations, the unit was stopped for 24 hours in order of the gelation. The operation of the water pumping was repeated then. Finally, the residuary resistance coefficient of the fractured rock sample which shows the permeability reduction of the sample after the treatment was calculated as

$$R_{>\mathrm{AB1}} = \frac{\operatorname{grad} P_2}{\operatorname{grad} P_1},$$

where $R_{>\mathrm{AB1}}$ is the residuary resistance coefficient after the treatment, $\operatorname{grad} P_1$ is the pressure gradient before the insulation process (Pa/m) and $\operatorname{grad} P_2$ is the pressure gradient after the insulation process (Pa/m).

Figure 3 and Table 1 represent the results of the filtration experiment.

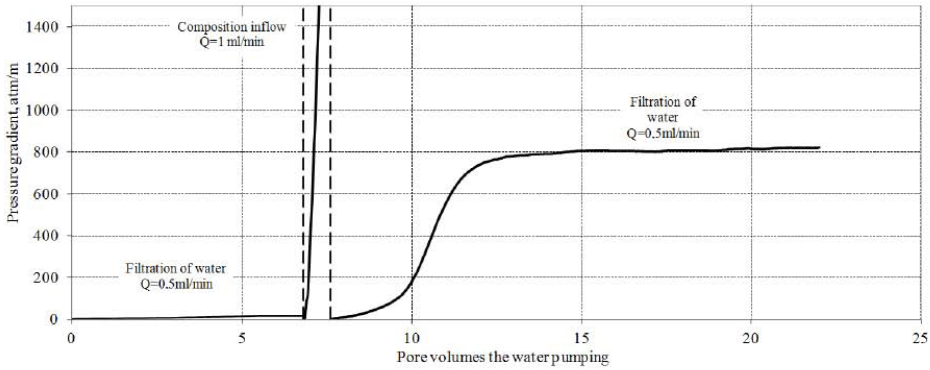

Fig. 3. Dependence of the pressure gradient on the pore volumes, the water being pumped on the saturated fractured-porous rock sample

Table 1. Experimental results

Parameter	Measure	Before the treatment	After the treatment
Pressure gradient for water	MPa/m	1.80	82.17
Core permeability	$\times 10^{-3}$ mkm^2	8.25	0.18
Permeability reduce factor	%	-	–97.8
Residuary resistance coefficient	u	-	45.7
Maximum pressure gradient for the composition	MPa/m	325.59	

As can be seen from Figure 3 and Table 1, the water permeability in the core sample with an artificially created fracture decreased 46 times. The maximum pressure gradient for the composition is 325.6 MPa/m. It can be concluded that proposed compound insulates cracks effectively thus allowing to displace an oil from low-permeability channels.

2. Conclusion

The gelling organic shutoff composition was developed for water inflow limitation in fractured-porous rocks. The main component of the compound is carboxymethyl cellulose (the mass fraction is 5.5 %), chrome acetate (III) (mass fraction is 1–1.1 %) used as a crosslinker, copper sulfate used for increase of the plastic strength of the composition is recommended as a densifier.

It is found that the ratio of the concentrations of chromium acetate and copper

sulfate allows adjusting the gelling time and strength properties of the composition. The relationship between the induction period of gelation period at shear rate in fractured-porous reservoir and the gap width obeys an exponential function. Its value is sufficient to inject the composition to a depth necessary for stability of the gelling compound to water breakthrough and blocking the formation of the treated interval.

The filtration experiment proved that the proposed composition can effectively insulate the fractured reservoir intervals; water permeability is reduced 46 times after the injection of the compound.

References

[1] O. Muraza, A. Galadima: *Aquathermolysis of heavy oil: A review and perspective on catalyst development.* Fuel *157* (2015), 219–231.

[2] I. Fofana, A. Bouaïcha, M. Farzaneh: *Characterization of aging transformer oil–pressboard insulation using some modern diagnostic techniques.* European Transactions on Electrical Power *21* (2010), 1110–1127.

[3] J. B. Curtis: *Fractured shale-gas systems.* AAPG Bulletin *86* (2002), 1921-1938.

[4] Y. He, L. Yang: *Testing study on variational characteristics of rockmass permeability under loading-unloading of confining pressure.* Chinese Journal of Rock Mechanics and Engineering (2004), No. 3.

[5] M. S. Al-Anazi, S. H. Al-Mutairi, M. Alkhaldi, M. N. Gurmen: *Laboratory evaluation of organic water shut-off gelling system for carbonate formations.* SPE European Formation Damage Conference, 7–10 June 2011, Noordwijk, The Netherlands, Paper SPE 144082-MS.

[6] C. Solans, P. Izquierdo, J. Nolla, N. Azemar, M. J. Garcia-Celma: *Nano-emulsions.* Current Opinion in Colloid & Interface Science *10* (2005), 102–110.

[7] Sh. Ikeda, K. Nishinari: *"Weak gel"-type rheological properties of aqueous dispersions of nonaggregated κ-Carrageenan helices.* Journal of Agriculture and Food Chemistry *49* (2001), 4436–4441.

Received October 12, 2017

Acta Technica *63* No. 3/2018, 481–492

Depth computation for the onset of organic sedimentation formation in the oil producing well as exemplified by the Sibirskoye oil field

G. Korobov[1,2], D. Podoprigora[1]

Abstract. The article deals with the issues of determining fluid temperature in the flowing wells complicated by the formation of asphaltene-resin-paraffin deposits. For production conditions of the Sibirskoye Oil Field, values of heat transfer coefficient in the heat equation have been estimated by analyzing the actual temperature logs of the well. It is shown that the calculated temperature logs constructed using these values of the heat transfer coefficient are practically identical to the actual ones. The authors determined the influence of asphaltene and resin content on wax appearance temperature in the well and on the deposit formation intensity. The article demonstrates nomograms enabling to evaluate wax appearance temperature in the well based on the values of asphaltenes and resin content in oil. Impact of water cut on the deposit formation intensity in the well has been shown. Using the obtained dependencies a mathematical model was created to evaluate the depth of the onset of asphaltene-resin-paraffin deposit formation in the well with practical accuracy.

Key words. Organic deposits, asphaltenes, resins, paraffins, wax appearance temperature.

1. Introduction

The current state of development in oil fields is related to their transition to the final stage of development which is accompanied by an increase in water cut, reservoir and bottom hole pressure drop, and increase in the content of high molecular weight components in crude oil. These factors increase the risk of complications in the operation of oil producing wells due to the formation of asphaltene-resin-paraffin deposits (ARPD) on the walls of the wells and washed equipment [1]. ARPD is intensively formed when fluid temperature is lower that the wax appearance temperature

[1]Department of Development and Operation of Oil and Gas Fields, "Saint-Petersburg Mining University", Saint-Petersburg, the Russian Federation
[2]Corresponding author

(paraffin crystallization point) [2]. Therefore it is necessary to determine the distribution of fluid temperature and wax appearance temperature in production wells with sufficiently practical accuracy. Currently the research of temperature distribution along the hoist resulted in a significant number of solutions to heat equation describing the temperature processes occurring during the movement of products along the production wellbore. Mishchenko [3] calculate the temperature distribution along the borehole as follows:

$$\frac{t}{t_{\mathrm{bh}}} = 1 - \frac{\mathrm{wh}}{t_{\mathrm{bh}}} \cdot \frac{h}{D} \cdot \frac{K\pi D^2}{4q\rho c}\,, \tag{1}$$

where t is the fluid temperature in wellbore cross-section at a distance h from the bottomhole (°C), t_{bh} is the bottomhole temperature (°C), w denotes the geothermal coefficient of rocks surrounding the borehole (°C/m), D stands for the borehole diameter (m), q is the volume flow rate for fluids (m^3/s), ρ denotes the fluid density ($\mathrm{kg/m}^3$), c stands for the fluid heat capacity (J/K), and K denotes the heat transfer coefficient ($\mathrm{W/(m^2\,°C)}$. The heat transfer coefficient K remains unknown in equation (1). This coefficient depends on numerous factors which in practice cannot always be known. Despite the large number of analytical studies, field engineers do not have simple and sufficiently precise recommendations for its determination. The value of temperature is now of undoubted practical interest not only at any point in the well, but even at the wellhead with the known bottomhole temperature. In [4, 5] it is proposed to calculate flow temperature at any tubing string cross-section by the equation

$$\begin{gathered} t\,(H) = t_{\mathrm{ft}} - (L_{\mathrm{ft}} - L_{\mathrm{fn}})\,\frac{0.0034 + 0.79G\cos\theta}{10^a} - \\ - (L_{\mathrm{fn}} - L)\frac{0.0034 + 0.79G\cos\theta}{10^a}\,, \\ a = \frac{Q_{\mathrm{fl}}}{20d_{\mathrm{ps}}^{2.67}}\,. \end{gathered} \tag{2}$$

Here, L_{ft}, L_{fn} and L denote the distances from the well head to the formation top, pump fishneck and the considered cross-section in the wellbore or in the tubing string, respectively (m), G is the mean geothermal coefficient (°C/m), t_{ft} stands for the temperature of rocks at the formation top elevation (°C), d_{ps} and d_{ts} represent the inside diameter of production and diameter of the tubing strings, respectively m, θ is the average hole angle (°), Q_{fl} stands for the well fluid rate (m^3/s). The construction of downhole temperature logs in the specific conditions of various development targets with the help of the above empirical equations which are given in a number of educational and reference books may lead to results that differ materially from the actual one. Figure 1 shows the calculated temperature logs obtained by the specified dependencies (9)–(11) for producing well No. 341 of the Sibirskoye Oil Field (Perm Region). The apparent discrepancy between the calculated temperature logs and the actual one indicates that the use of known empirical equations in the conditions of Sibirskoye Oil Field leads to considerable error when calculating

temperature distribution in wells.

2. Methodology

2.1. Changing wax appearance temperature

To verify the influence of asphaltene content of oil on the wax appearance temperature at the laboratory of the Department of "Development and Operation of Oil and Gas Fields", Saint-Petersburg Mining Universityan experiment is carried out to determine wax appearance temperature using the FLASS analyzer (Vinci Technologies) intended to study solids onset processes in the reservoir fluid. The plant flow sheet is shown in Fig. 1. This allows for qualitative and quantitative analysis with a full description of the asphaltene and paraffin precipitation conditions (pressure, temperature, morphology, visualization, change of structure, etc.).

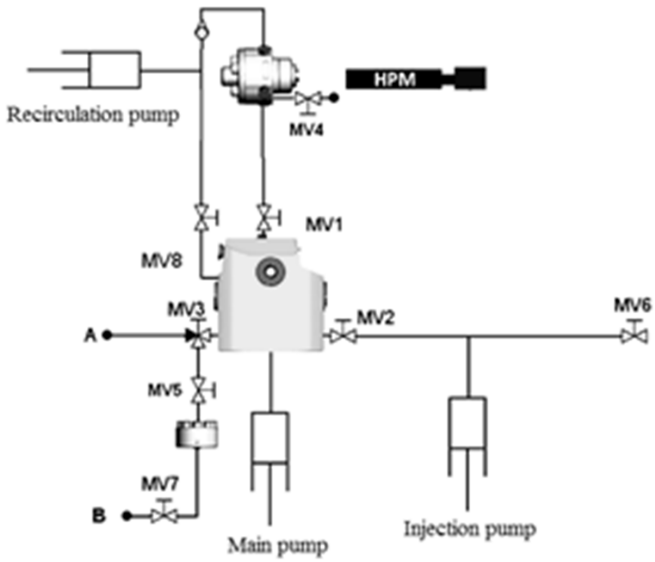

Fig. 1. FLASS system flow sheet

The measuring system includes 3 types of equipment to study solid deposition in the reservoir fluid sample:

1) High Pressure Microscope (HPM) is designed to accurately visualize paraffin and asphaltene precipitation at pressure up to 103 MPa and temperature sup to 170 °C. It enables to detect solid particles and monitor physical and morphological variations of the formed asphaltene-resin-paraffin particles with changing temperature, pressure, time and the impact of various chemical agents (CO_2, ARPD inhibitors, surfactants, solvents, etc.).

2) Solid Detection System with a laser source (SDS) is used to determine the

conditions of asphaltenes and paraffins precipitation in the reservoir fluid.

3) HPHT Organic Solid Filter is intended to determine the amount of solids formed in the fluid sample under altering PVT conditions.

Oil samples are prepared in accordance with the instructions and recommendations of Vinci Technologies Company. Sample preparation consists of heating oil samples to 90 °C in a special charging device, by means of which of oil is supplied in the PVT cell for further studies. Oil heating completely dissolve paraffins, asphaltenes and resins. After charging the PVT cell is isolated by a special high-pressure valve. Oil sample is thermostated for 24 hours in the PVT-cell. To study the paraffins and asphaltenes deposition process, SDS and HPM systems are typically used.

The general procedure for the experiments included the following:

1. To set permanent pressure in the PVT cell (an isobaric process). At the same time in case of any changes in system the pressure will be the same owing to the pump operation.

2. To reduce temperature gradually by cooling PVT cell using a temperature control system. In order to simulate the flow of oil in the well a system is included to perform continuous stirring at a certain speed. Data are recorded on the hard disk.

3. To analyze the information received for studying the conditions of asphaltene-resin-paraffin precipitation.

To determine the conditions of paraffins and asphaltenes precipitation, the isobaric method was chosen during which the system pressure is kept constant, and the temperature varies in a predetermined range. The system Pressure is selected on the basis of production data as equal to 24 MPa.

2.2. Studying intensity of asphaltene-resin-paraffin deposits formation by 'cold finger' test

To evaluate the impact of total content of asphaltenous-resinous substances (ARS) on the intensity of ARPD formation a cold finger test was conducted.

3. Results

3.1. Temperature distribution along the wellbore

While rising in the production or tubing string, fluid carries off the heat externally via the pipe wall in the elementary section of the pipe dh with lateral surface πDdh and the amount of this heat is equal to $K\left[t_{\text{fl}} - t_{\text{amb}}\right]\pi Ddh$. The fluid temperature decreases in this case by $c_{\text{fl}}\rho_{\text{fl}}vF_{\text{TR}}\,\mathrm{d}t_{\text{fl}}$. It is obvious that

$$K\left[t_{\text{lq}} - (t_{\text{pl}} - wh)\right]\pi Ddh = c_{\text{fl}}\rho_{\text{fl}}vF_{\text{fl}}\mathrm{t}_{\text{fl}}\,. \tag{3}$$

Here, K is the coefficient of heat transfer from fluid to the environment, t_{fl} denotes the fluid temperature in the elementary section, D stands for the inside diameter of

the pipe, c_{fl} is the fluid specific heat, ρ_{fl} represents the fluid density, v is the average speed of fluid flow, F_{p} denotes the pipe internal area, w is the geothermal gradient, t_{bh} represents the fluid bottomhole temperature, h is the (vertical) distance from the bottom hole to the elementary section of the pipe under consideration, t_{amb} denotes the ambient temperature (temperature of rocks at the depth $H_w - h$, H_{w} representing the well depth).

Taking into account that $vF_{\mathrm{p}} = q$ (volumetric fluid flow rate), solution of the equation (3) has the following form:

$$t_{\mathrm{fl}} = t_{\mathrm{bh}} - wh + \frac{c_{\mathrm{fl}} w \rho_{\mathrm{fl}} q}{K\pi D} - C_1 \mathrm{e}^{\frac{K\pi D h}{c_{\mathrm{fl}} \rho_{\mathrm{fl}} q}}\,, \tag{4}$$

or

$$t_{\mathrm{fl}} = t_{\mathrm{bh}} - wh + \frac{c_{\mathrm{fl}} w \rho_{\mathrm{fl}} q}{K\pi D}(1 - \mathrm{e}^{\frac{K\pi D h}{c_{\mathrm{fl}} \rho_{\mathrm{fl}} q}})\,. \tag{5}$$

Here, C_1 is an integration constant that is determined from the initial conditions at $h = 0$, where $t_{\mathrm{fl}} = t_{\mathrm{bh}}$, therefore

$$C_1 = \frac{c_{\mathrm{fl}} w \rho_{\mathrm{fl}} q}{K\pi D}\,.$$

The heat transfer coefficient in equations (3–5) can be presented in the form of

$$K = \frac{1}{\frac{1}{\alpha} + R}\,, \tag{6}$$

where α is the coefficient of heat transfer from fluid to the internal wall of the pipe, R denotes the thermal resistance of pipe walls, annular space and borehole environment (see Fig. 2).

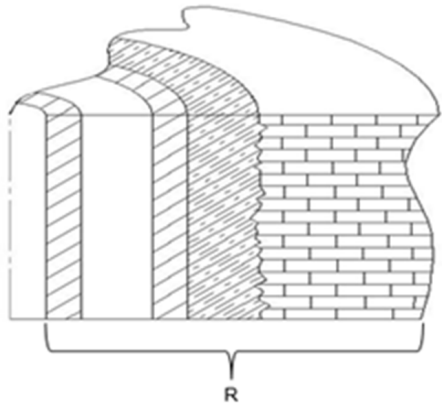

Fig. 2. Well heat transfer scheme

The coefficient α can be determined by criteria equations [6]: for a laminar flow there holds

$$\alpha = 0.021\,\mathrm{Re}^{0.8}\mathrm{Pr}^{0.43}\,\frac{\lambda_{\mathrm{f}}}{D} \tag{7}$$

and for a turbulent flow

$$\alpha = 4\frac{\lambda_{\mathrm{f}}}{D}\,. \tag{8}$$

Here, Re is the Reynolds number (similarity criterion) λ_{f} is the thermal conductivity of the pipe material and Pr is the Prandtl number (similarity criterion).

The thermal resistance R consists of resistances of tubing body, medium filling the annular space, the pipe body of the production string, cement stone and rocks surrounding the well (Fig. 2). Analytical determination of R is complicated (for the lack of information about the thermal properties of rocks surrounding the borehole, cement stone thickness is not constant; the tubing is not strictly centered in the production string, etc.).

Available actual temperature logs are used to evaluate the thermal resistance R. When solving the reverse problem using formulas (3), (4) and actual temperature log thermal, resistance R is determined.

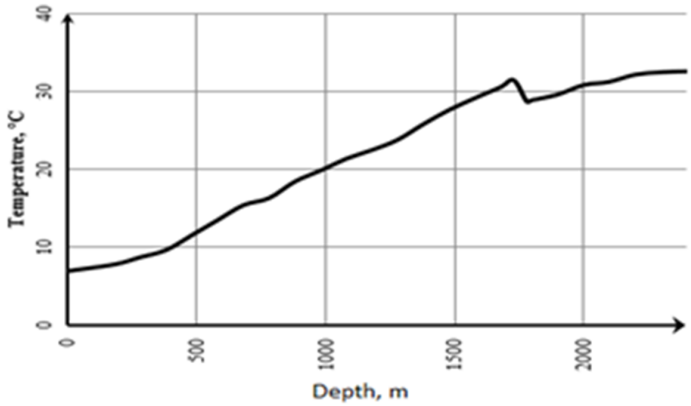

Fig. 3. An example of a downhole temperature log

The thermal resistance has no constant value along the well depth, since in different intervals it is composed of different constituents. Therefore, when determining thermal resistance, separate intervals (sections) should be singled out in the well [7]:

1 – from the bottomhole to the pump (tubing string shoe),

2 – from the pump to the dynamic head,

3 – from the dynamic head to the wellhead (see Fig. 4).

The thermal resistances of separate intervals for the studied 10 wells at Sibirskoye Oil Field are determined based on actual temperature logs by data averaging (see Fig. 4). The following values of R were obtained for the intervals [7]:

With regard to the determined thermal resistance calculation of temperature distribution is shown as exemplified by well No. 341 of the Sibirskoye Oil Field (Fig. 5). The figure shows the actual temperature log and calculated temperature logs built according to the technique proposed by Mishchenko [68] and Lyapkov for comparison [4].

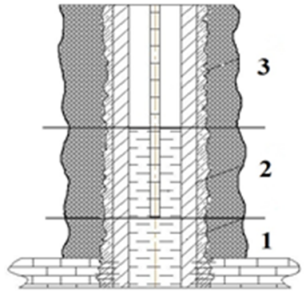

Fig. 4. Singling out well intervals during determination of resistance R: $R_1 = 0.0763\,\mathrm{m}^2\,^\circ\mathrm{C})/\mathrm{W}$, $R_2 = 0.0774\,\mathrm{m}^2\,^\circ\mathrm{C})/\mathrm{W}$, $R_3 = 0.0763\,\mathrm{m}^2\,^\circ\mathrm{C})/\mathrm{W}$

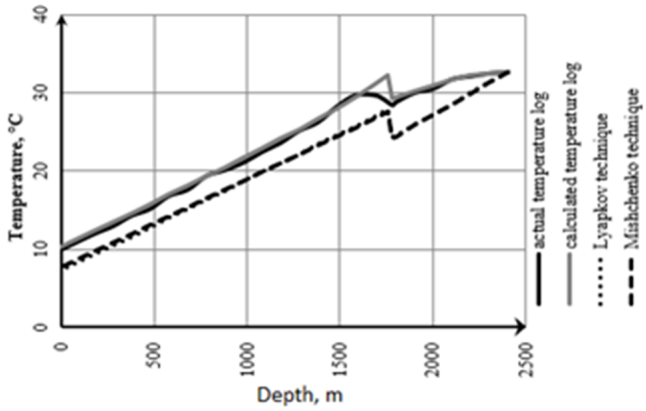

Fig. 5. Temperature logs of well No. 341, Sibirskoye Oil Field

3.2. Calculating wax appearance temperature distribution along the producing wellbore

To study the impact of asphaltenous-resinous components in oil on the process of asphalt, resin, and paraffin deposits formation, 5 more oil samples are taken. Oil samples were taken at one of the oil fields complicated with ARPD precipitation. Some data on the properties of these oil samples are given in Table 1.

Table 1. Properties and composition of oil samples

Sample number	1	2	3	4	5
Density (g/cm^3)	0.826	0.894	0.815	0.829	0.846
Dynamic viscosity (mPa s)	7.57	42.68	5.25	13.1	7.27
Contents					
paraffins (% wt)	5.9	5.6	8.1	7.8	4.5
asphaltenes (% wt)	1.6	3.6	0.6	1.8	3.3
resins (% wt)	2.8	9.5	2.5	3.5	4.5

By mixing samples specified in Table 1, two oil models were obtained (model A and model B), differing from each other in the content of asphaltenes (with similar content of resins and paraffins). Mixing samples No. 1, No. 2, and No. 3 in the proportions of 0.75, 0.18, 0.07, respectively, enabled to obtain oil model A. Mixing samples No. 1, No. 4, No. 5 in the proportions of 0.04, 0.44 and 0.52, respectively, enabled to obtain oil model B. The proportions are selected such that the resulting oil models A and B have the same content of paraffins and resins with different content of asphaltenes. The data about the content of high molecular weight components in the oil models (A, B) are given in Table 2.

Table 2. Content of high molecular weight components in the oil models (A, B)

Oil model	A	B
Proportions	1:2:3=0.75:0.18:0.07	1:4:5=0.04:0.44:0.52
Contents		
paraffins (% wt)	6	6
asphaltenes (% wt)	1.9	2.6
resins (% wt)	4	4

In further studies similar content of paraffins and resins with different content of asphaltenes in the oil model allows obtaining the dependence of any indicator on the content of asphaltenes in oil and eliminate the impact of paraffin and resin content in oil on this property. Prepared oil models (A, B) were used to assess the impact of asphaltene content on the ARPD formation process. Field data analysis shows that intensive ARPD formation occurs at fluid temperature below the wax appearance temperature [9]. To study the impact of resins content in oil on its paraffin saturation point two models are obtained. The proportions were selected so that the resulting oil models C and D have the same content of paraffins and asphaltenes with different content of resins. Data about the content of high molecular weight components in the oil models (C, D) are given in Table 3.

Table 3. Content of high molecular weight components in the oil models (C, D)

Oil model	C	D
Proportions	1:2:3=0.38:0.51:0.11	1:4:5=0.11:0.41:0.48
Contents		
paraffins (% wt)	6	6
asphaltenes (% wt)	2.5	2.5
resins (% wt)	3.5	6.2

In further studies similar content of paraffins and asphaltenes with different content of resins in the oil model allows obtaining the dependence of any indicator on the content of resins in oil and eliminate the impact of paraffins and asphaltenes in oil on this property. As a result of the experiment, the plot of paraffin wax appearance temperature versus the content of asphaltenes was built (see Fig. 6).

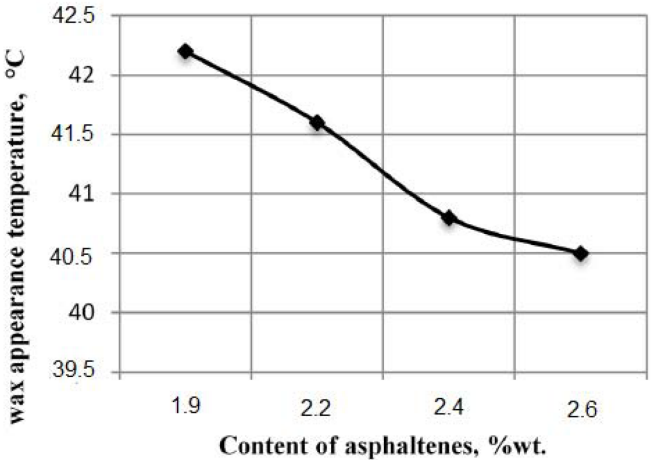

Fig. 6. Wax appearance temperature vs asphaltene content in oil

Experimental results relating to the evaluation of resin content impact on the wax appearance temperature, with isobaric decrease in temperature and at pressure of 24 MPa are shown in Fig. 7.

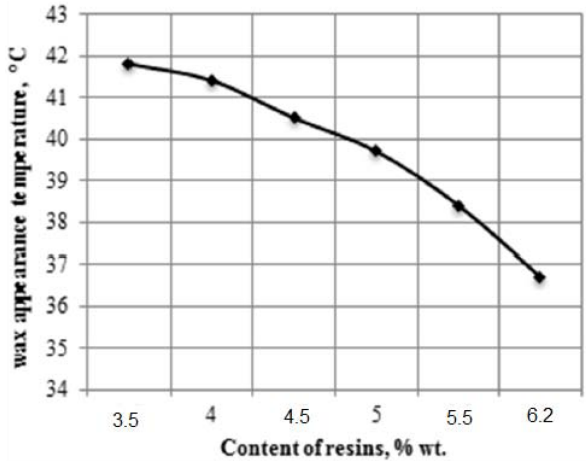

Fig. 7. Wax appearance temperature vs. resins content in oil

Most mathematical models used to determine the wax appearance temperature either do not take into account the content of asphaltenes and resins for the calculation, or relationship between the wax appearance temperature of oil and ARS content in it contradicts to the results obtained in this work. To determine wax appearance temperature with regard to the obtained relationships, a nomogram was built (see Fig. 8) that allows determining wax appearance temperature with practical accuracy. This relationship is valid for calculation of wax appearance temperature for oil with paraffin content ranging from 4.5 to 7.5 % wt and asphaltenous-resinous substances ranging from 4.5 to 13 % wt.

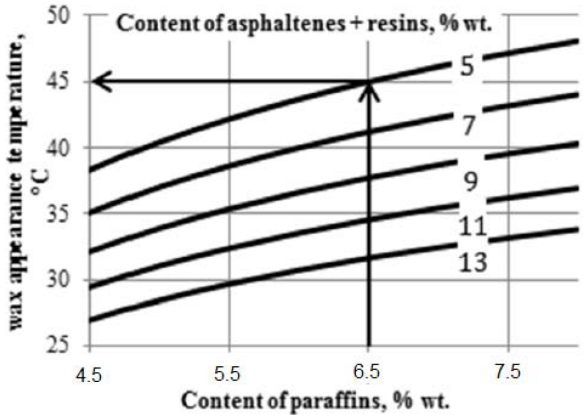

Fig. 8. Nomogram to determine wax appearance temperature

The above nomogram allows determining the wax appearance temperature in the well as a function of the content of paraffins, asphaltenes, and resins. Depth of ARPD formation is determined graphically intersection of the well temperature distribution curve and wax appearance temperature distribution curve. This method enables to consider a large amount of data while determining the ARPD formation depth:

$$H_{\mathrm{ARPD}} = f(P_i, T_i, \Gamma_i, \Delta T_{\mathrm{escp}}, Q_{\mathrm{fl}}, \beta_{\mathrm{fl}}, \eta_{\mathrm{p}}, D_{\mathrm{ts}})\,, \tag{9}$$

where P_i is the fluid flow pressure in the well, T_i denotes the fluid flow temperature, G_i represents the gas content in fluid flow, ΔT_{escp} stands for the thermal heating of electrical submersible centrifugal pump, Q_{fl} is the fluid rate, β_{fl} denotes the fluid water cut, η_{p} represents the pump efficiency, and D_{ts} stands for the tubing diameter.

The depth of ARPD formation on set was determined by means of model (5) for the Shershnevskoye Oil Field for 38 wells (Fig. 8). Depths of ARPD precipitation on set are plotted versus well flow rates (Fig. 9) and versus altering temperature of fluid passing through electrical centrifugal pump; it is shown that inside tubing diameter has impact on the paraffin precipitation process.

4. Conclusion

In the studied wells of the Shershnevskoye Oil Field depth of ARPD formation on set varied from 500 to 1200 m. Figure 9 shows the trend of ARPD precipitation depth decreasing with the growth of the well flow rate (approximately 8 meters per $1\,\mathrm{m}^3$/day of the flow rate increase).

The described mathematical model allows for predicting the depth of the onset of the formation of ARPD in the well, and reducing the risk of complications associated with the ARPD formation, enabling to select the operating parameters of the downhole equipment in view of the possible complications during the operation of wells.

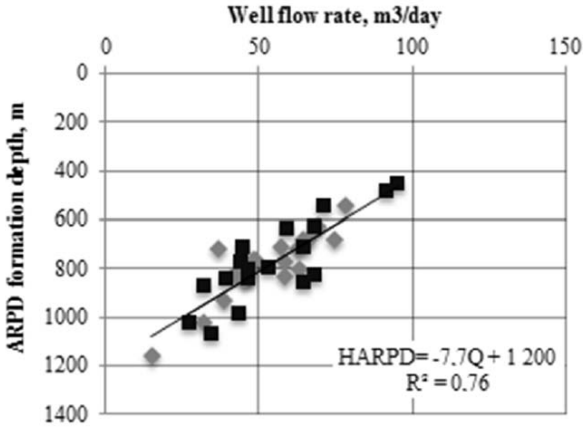

Fig. 9. Relationship between ARPD precipitation depth and well flow rates

References

[1] N. J. Poole, F. Sarvar: *Fundamentals of heat transfer.* Proc. IEE Colloquium on Thermal Design of Electronic Systems, 29–29 March 1989, London, UK (1989).

[2] G. Y. Korobov, I. Raupov: *Study of adsorption and desorption of asphaltene sediments inhibitor in the bottomhole formation zone.* International Journal of Applied Engineering Research *12* (2017), No. 2, 267–272.

[3] R. M. Balabin, R. Z. Syunyaev, Th. Schmid, J. Stadler, E. I. Lomakina, R. Zenobi: *Asphaltene adsorption onto an iron surface: Combined near-infrared (NIR), Raman, and AFM study of the kinetics, thermodynamics, and layer structure.* Energy & Fuels *25* (2011), 189–196.

[4] A. N. Zotov, K. R. Urazakov, E. B. Dumler: *Simulation of operation of pneumatic compensator with quasi-zero stiffness in the electric centrifugal submersible pump unit.* Journal of Mining Institute *229* (2018), 70-76.

[5] H. Ohta, K. Nomura, M. Orita, M. Hirano, K. Ueda, T. Suzuki, Y. Ikuhara, H. Hosono: *Single-crystalline films of the homologous series $InGaO_3(ZnO)_m$ grown by reactive solid-phase epitaxy.* Advanced Functional Materials *13* (2003), 139–144.

[6] J. H. Pacheco-Sanchez, G. A. Mansoori: *In situ remediation of heavy organic deposits using aromatic solvents.* Proc. Latin American and Caribbean Petroleum Engineering Conference, 30 August–3 September 1997, Rio de Janeiro, Brazil (1997).

[7] C. M. Matthews, R. Chachula, B. R. Peachey, S. C. Solanki: *Application of downhole oil/water separation systems in the alliance field.* Proc. SPE Health, Safety and Environment in Oil and Gas Exploration and Production Conference, 9–12 June 1996, New Orleans, Louisiana (1996).

[8] I. A. Struchkov, M. K. Rogachev: *Risk of wax precipitation in oil well.* Natural Resources Research *26* (2017), 67–73.

Received October 12, 2017

Acta Technica *63* No. 3/2018, 493–500

Research of polymer compositions rheological properties for oil production

Inzir Ramilevich Raupov[1], Grigoriy Yurevich Korobov[1]

Abstract. In the present article the results of theoretical and laboratory researches for rheological performances of aqueous polymer solution, represented by hydrolyzed polyacrylonitrile and polymethacrylate ("Geopan" reagent), were considered. It was established that with increase of the polymer content in solution, the yield stress and, consequently, the plastic viscosity logarithmically increase. Repeatability of obtained laboratory data is confirmed by directly proportional dependence of the solution consistency coefficient on the polymer concentration. It was also found that with increase of the polymer content in solution, the flow index decreases according to a power law. With increase of a molecular weight, the polymer solution viscosity increases according to the power law, and the same behavior of curve is also observed for dependence of the molecular weight on the degree of hydrolysis. When the degree of hydrolysis increases, the molecular weight increases according to the power law. The results of the theoretical and laboratory researches shown in the present article may be used in modeling of such oil production processes as a polymer water-flooding and an in-situ water shutoff.

Key words. Hard to recover oil, polymer solution, rheological researches, effective viscosity, shear rate, shear stress.

1. Introduction

It is commonly known that currently a share of hard to recover oil reserves (HRR) in residual reserves grows steadily and it is associated with the active recovery of mobile oil reserves, the oil properties deterioration and the geologic aspects of the productive strata. In the work [1] according to data of oil reserves analysis in the Republic of Tatarstan (RT) and considering the usage of modern methods of oil production notes that the oil HRR account for 7.7 % and the immobile oil reserves account for 61.4 % of geologic reserves of oil. In general, the share of the oil HRR in Russian Federation is 78.7 % as of 01. 01. 2013 [2]. Chemical reagents development for oil production objects, in particularly for the certain geology-physical

[1]Saint-Petersburg Mining University, 2, 22nd line, Saint-Petersburg, 199106, Russian Federation

conditions, is performed by carrying out of complex laboratory researches including the physical-chemical, rheological and filtration researches [3–8]. In this article we will consider the theoretical and practical part of the rheological researches of the polymer solutions and compositions, including those used for polymer water-flooding and in-situ water shutoff [9, 10].

2. Methodology

Determination of the effective viscosity of the polymer solutions was carried out according to [10] using Rheotest RN 4.1 general-purpose rotary viscometer having H2 cylindrical measurement system. Measurement method for the effective viscosity involves plotting of "viscosity curve" in controlled shear rate mode (CR test–Controlled Rate). Principle of the method is based on obtaining the dependence of the effective viscosity (shear stress) on shear rate (rotation frequency) at gradual increase of the last parameter from 0 up to 300 1/s (fluid viscosity curve).

3. Results of theoretical and practical research

As per to the flow and viscosity curves (dependence of the shear stress (Fig. 1, left part) and the effective viscosity (Fig. 1, right part) the polymer solutions relate to pseudoplastic fluids having yield strength according to [8–10]. The hydrolyzed polyacrylonitrile and polymethacrylate (the "Geopan" reagent) widely applicable in oil production was used as a target of research.

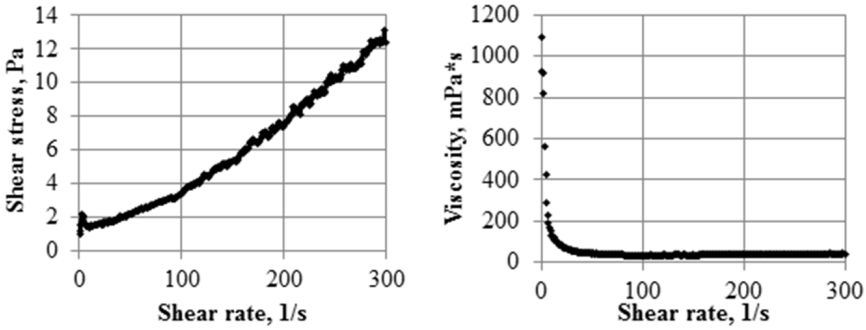

Fig. 1. Flow curve (left) and Viscosity curve (right) of 0.1 % aqueous solution of the hydrolyzed polyacrylonitrile and polymethacrylate

Viscosity parameter (μ) of the polymer solutions can depend on minimum of 6 values, so that it can be represented as a function

$$\mu = f(S, T, P, D, t, EF)\,. \tag{1}$$

According to the research results, the two molecular weights areas divided by

critical value M_c were determined:

$$\mu = a \cdot M^{\alpha} \text{ for } M < M_c,\ \mu = b \cdot M^{\beta} \text{ for } M \geq M_c\,. \tag{2}$$

Here, a and b are the specific constants of polymer-homologous range, α is a value of the order of 1 (typically, more than 1) and β is a value close to 3.4–3.5.

In this work, the characteristic viscosity depends on the molecular weight as per formula [8]

$$M = 2.11 \cdot h^{0.75}\,. \tag{3}$$

where K is a constant, which depends on the nature of solvent, polymer and temperature and a is a constant determined by conformation of a macromolecule in solution (for flexible polymers: $0.5 < a < 0.8$). A viscosity of polyesters melt depends on the degree of polymerization as per the following formula [10]

$$\ln \mu = \frac{A}{R} + \frac{B}{R}\sqrt{n} + \frac{C}{RT}\,, \tag{4}$$

where n denotes the degree of polymerization, T is the absolute temperature, R represents the universal gas constant and A, B, C are constants for the given polymer-homologous range.

Paper [9] provides the results for researches of the effective viscosity of the polymer solutions of different molecular weight and the degree of hydrolysis. On the basis of obtained data the dependences of μ on M (Fig. 2) at different content of polymer in aqueous solution were plotted.

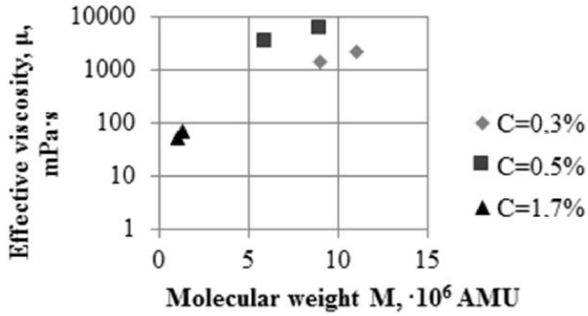

Fig. 2. Dependence of the effective viscosity of aqueous polyacrylamides solutions of different grades on molecular weights of PAA

With increasing the degree of hydrolysis of polyacrylamide the molecular weight increases according to the power law

$$M = 2.11 \cdot h^{0.75}\,. \tag{5}$$

In this case, the coefficient $R^2 = 0.95$.

The increase of molecular weight results in the increase in the effective viscosity. Consequently, with the increasing of value of h, the μ value of PAA solutions increases.

The activation theory is associated with the activation energy E of fluid flow process which is described by the Arrhenius-Frenkel-Eyring (AFE) equation [9]

$$\mu = B \exp\left(\frac{E}{RT}\right) , \tag{6}$$

where E is the activation energy of the flow process and B a constant.

When the value of B, which is weakly dependent on temperature, is specified, equation (6) can be rewritten as follows:

$$\mu = B \cdot T^{\frac{3}{2}} \exp\left(\frac{E}{RT}\right) . \tag{7}$$

As per the free-volume theory, the temperature dependence of the viscosity is associated with a free volume. The Dependence of the free volume v_{f} on temperature can be shown by the M. Williams, R. Landel and J. Ferry formula

$$v_{\mathrm{f}} = v_{\mathrm{f,g}} \left(1 + \alpha_0 (T - T_{\mathrm{g}})\right) , \tag{8}$$

(8) where T_{g} is the glass transition temperature, $v_{\mathrm{f,g}}$ is the value of v_{f} at $T = T_{\mathrm{g}}$ and α_0 is the thermal expansion coefficient of the free volume.

Then the viscosity can be determined according to the researches A. Doolittle and T. Fox by formula

$$\mu = A' \cdot \exp\left(\frac{B_0 v}{v_{\mathrm{f}}}\right) , \tag{9}$$

where A' and B_0 are constants.

G. Falcher and G. Tamman proposed a modification of the free-volume theory using formulas

$$\mu = A \cdot \exp\left(\frac{B}{T - T_0}\right) , \; B = \frac{b_0 v_0}{2.3\alpha_0'} . \tag{10}$$

Summarizing the formulas applied in the activation theory and the free-volume theory, the viscosity can be determined by the following equation

$$\mu = A \cdot \exp\left(\frac{B}{T - T_0} + \frac{E_v^*}{RT}\right) . \tag{11}$$

The empirical coefficients and the determinacy coefficients for the equations of dependence of the effective viscosity on temperature are listed in Table 1.

According to the results of the laboratory researches of the hydrolyzed polyacrylonitrile and polymethacrylate the following dependence of the effective viscosity of the “Geopan” aqueous solutions was established

$$\mu = A \cdot \exp\left(-BT\right) , \tag{12}$$

where A and B are the empirical coefficients.

Table 1. The empirical coefficients and the determinacy coefficients for the equations of dependence of the effective viscosity on temperature

No.	Shear rate	Polymer content in the polymer solution (% wt)								
		0.1			0.5			1		
		A	B	R^2	A	B	R^2	A	B	R^2
1	0.1	1320	0,010	0.86	44713	0.030	0.96	119634	0.025	1
2	1	459	0.010	0.95	5908	0.018	0.96	15465	0.016	1
3	10	160	0.011	0.99	781	0.007	0.94	1999	0.007	0.99
4	50	76	0.011	0.99	240	0.003	0.96	528	0.001	0.92
5	100	41	0.011	0.96	153	0.003	0.98	318	0.002	0.76
6	200	41	0.011	0.96	121	0.008	0.92	228	0.004	0.79
7	300	34	0.011	0.96	121	0.011	0.98	221	0.009	0.99

The influence of pressure on viscosity of polymer systems is poorly studied [9]. In the same work an exponential relationship between initial viscosity and pressure in the low values area is specified

$$\mu_{\mathrm{P}} = \mu_{\mathrm{A}} \exp^{\delta P}, \tag{13}$$

where μ_{P} is the viscosity value at pressure P, μ_{A} denotes the the viscosity at the atmospheric pressure and δ is a constant coefficient (which has a value of the order of several thousands of reciprocal bars).

As previously stated, the dependence of the viscosity on shear rate predetermines the behavior of non-Newtonian fluid. The issue regarding the viscosity changing depending on shear rate (viscosity curve) and on shear stress for the polymer solutions was quite well studied [4, 9] and so on.

For example, in the works of Vinogradov and Malkin the empirical formulas are given which describe the changing of viscosity depending on shear rate and on shear stress.

According to the results of our researches the power-law relations (Fig. 3) between the effective viscosity and the shear rate D

$$\mu = \mu_0 + \frac{a}{D^b}, \tag{14}$$

where a and b are empirical coefficients, μ_0 is the «initial» viscosity, corresponding to the yield strength τ_0.

From the formulas of the dependence of the effective viscosity on the shear rate which are represented in the theoretical part of the article, the Herschel-Bulkley model is one of the most completely models describing the results obtained. The values of the empirical coefficients and the plastic viscosity of 0.1, 0.5 and 1 % aqueous solutions of the hydrolyzed polyacrylonitrile and polymethacrylate are summarized in Table 2.

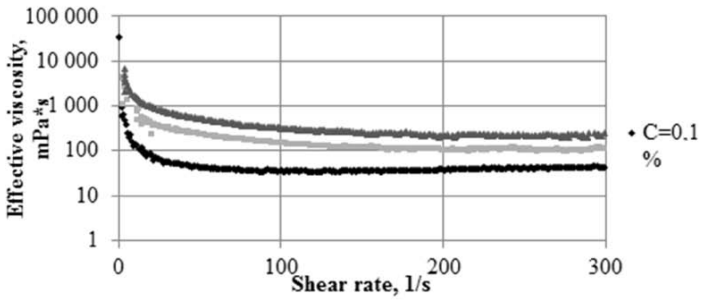

Fig. 3. Dependence of the effective viscosity of the polymer solutions with different concentration on the shear rate

Table 2. The empirical coefficients and the plastic viscosity of 0.1, 0.,5 and 1 % aqueous solutions of the "Geopan" as per the Herschel-Bulkley model

No.	Polymer content C in the polymer solution (% wt)	«Initial» viscosity corresponding to yield strength τ_0 (plastic viscosity) μ_0 (μ_p)	Consistency factor K	Flow index n
1	0.1	892	366	0.551
2	0.5	4339	2806	0.382
3	1	6527	6267	0.374

As a result of the analysis of the rheological performances of the "Geopan" aqueous solution, the following is revealed that:

1) With increase of the polymer content in solution the yield strength increases and, correspondingly, the plastic viscosity increases logarithmically. Moreover, the solution consistency coefficient is directly proportional to the polymer concentration, and it is indicates the repeatability of the obtained laboratory data.

2) With increase of the polymer content in solution the flow index decreases according to the power law.

4. Conclusion

The results of the laboratory and theoretical researches obtained in the present study are important for modeling of such oil production processes as the polymer water-flooding and the in-situ water shutoff. When performing the process activities associated with flooding of the polymer solution into stratum, it is necessary to obtain the reliable values of the viscosity depending on geology-physical conditions of the stratum. In the absence of taking into account of the influence of the physical parameters reviewed above on the viscosity and its incorrect determination it can results in the negative results, for example, the uncontrolled formation of high-conductive crack.

References

[1] J. C. Cano: *Effective energy conservation and management in the building sector: the answer to the energy predicament.* FIU Electronic Theses and Dissertations (1985).

[2] L. K. Altunina, V. A. Pitchers: *Wettability and oil recovery from carbonates: Effects of temperature and potential determining ions.* Colloids and Surfaces A: Physicochemical and Engineering Aspects *279* (2006), 179–187.

[3] A. A. Kartashov, D. G. Lazutin, O. V. Maksimenko, M. Yu. Smirnov: *Dynamic interpretation of archive reflection profiling data: Implications for vendian terrigenous reservoir rocks (case study of upper Chona field).* Seismic Technology *9* (2012), 46–55.

[4] J. Songok, M. Toivakka: *Enhancing capillary-driven flow for paper-based microfluidic channels.* ACS Applied Materials & Interfaces *8* (2016), 30523–30530.

[5] H. H. Vinters, M. Mours: *Rheology of polymers near liquid-solid transitions.* Neutron Spin Echo Spectroscopy Viscoelasticity Rheology, Springer, Chemical Engineering Faculty Publication Series, Vol. 134, 165–234 (1997).

[6] S. O. Ilyin, M. P. Arinina, M. Yu. Polyakova, V. I. Kulichikhin, A. Ya. Malkin: *Rheological comparison of light and heavy crude oils.* Fuel *186* (2016), 157–167.

[7] S. M. Petrov, Ya. I. I. Abdelsalam, A. V. Vakhin, L. R. Baibekova, G. P. Kayukova, E. A. Karalin: *Study of the rheological properties of heat-treatment products of asphaltic oils in the presence of rock-forming minerals.* Chemistry and Technology of Fuels and Oils *51* (2015), No. 1, 133–139.

[8] GOST 25276-82: *Polymers. Method for determination of viscosity by a rotational viscometer at a certain shear rate* (1982).

[9] Ph. Rathsack, M. M. Kroll, M. Otto: *Analysis of high molecular compounds in pyrolysis liquids from a german brown coal by FT-ICR-MS.* Fuel *115* (2014), 461–468.

[10] F. M. Wunner, S. Florczak, P. Mieszczanek, O. Bas, E. M. De Juan Pardo, D. W. Hutmacher: *Electrospinning with polymer melts – state of the art and future perspectives.* Comprehensive Biomaterials II, Elsevier, 217–235 (2017).

Received November 20, 2017